Approaches for improving the combustion, performance, and emissions of marine propulsion engines

エルサイード アブデルミード タウフィーク アブデルミード

Ph.D. Thesis on

Approaches for improving the combustion, performance, and emissions of marine propulsion engines

by

ELSAYED ABDELHAMEED

Supervised by

Assoc. Prof. Hiroshi Tashima

Engine and Combustion Laboratory (ECL)
Department of Energy and Environmental Engineering (EEE)
Interdisciplinary Graduate School of Engineering Sciences (IGSES)
Kyushu University

Japan

September 2023

Abstract

Diesel engines are the most often utilized in the marine sector due to their efficiency, dependability, and fuel flexibility, however pre-chamber gas engines, which have lower emissions and greater fuel economy, are gaining popularity. Larger ships use diesel engines, whereas smaller ships use pre-chamber gas engines or other alternative fuel engines. As the industry attempts to fulfill International Maritime Organization emissions standards, this tendency will likely continue. This thesis investigated diesel spray and methane jet dynamics in engine-like environments experimentally and numerically. We then examined water emulsion, exhaust gas recirculation, methane gas dilution, and methane-hydrogen as a direct-injected fuel to reduce engine greenhouse gas emissions.

The results revealed that the passive entrainment air flux induced by spray motion was much less than the active entrainment along with spray development or droplet dispersion. Using WFE with EGR significantly reduced NO emissions by up to 94% while increasing thermal efficiency by 4%. Also, Gas oil emulsion reduced NOx emissions by 95% and methane-nitrogen mixture reduce NOx emissions to 62% of gas oil fuel emissions. In the case of methane-hydrogen, the penetration length of the methane-hydrogen blend jet was slightly shorter than the methane by 5%. The hydrogen usage increased the in-cylinder pressure and the indicated mean effective pressure by 7.5% and 11%, respectively. Moreover, hydrogen usage decreased CO_2 and hydrocarbon emissions by 23% and 60%.

Acknowledgments

In the name of Allah, the Most Gracious, the Most Merciful. All praise, prostrations, and supplications are due to Allah, who aided me at every step of this project and helped me complete this work. Also, I offer my heartfelt thanks to my parents for giving me the opportunity to pursue my dreams, and for their unwavering belief and support throughout my academic journey.

I am deeply grateful to my supervisor, Assoc. Prof. Hiroshi Tashima, for his exceptional guidance, unwavering support, and constant encouragement throughout my doctoral studies at Kyushu University. His insights, feedback, and expertise have been invaluable to me, and I will always be indebted to him for his mentorship.

I would also like to extend my gratitude to all the members of the Engine and Combustion Laboratory for their invaluable support, insights, and encouragement during my research. Their contributions have been essential to the success of this project, and I am fortunate to have been part of such a collaborative and supportive research community.

Lastly, I would like to acknowledge the Japanese Ministry of Education, Culture, Sports, Science, and Technology (MEXT) for their financial support during my postgraduate studies. Their funding has enabled me to pursue my academic and research goals, and I am grateful for their investment in my future.

Elsayed Abdelhameed

Journal Publications

[1] E. Abdelhameed, H. Tashima, Experimental study on the effects of methane-hydrogen jet as direct injected fuel in marine diesel engine, Energy. 267 (2023) 126569. https://doi.org/10.1016/j.energy.2022.126569.

[2] E. Abdelhameed, H. Tashima, Experimental investigation on methane inert gas dilution effect on marine gas diesel engine performance and emissions, Energy Sources, Part A Recover. Util. Environ. Eff. 44 (2022) 3584–3596. https://doi.org/10.1080/15567036.2022.2067603.

[3] E. Abdelhameed, H. Tashima, EGR and Emulsified Fuel Combination Effects on the Combustion, Performance, and NOx Emissions in Marine Diesel Engines, Energies. 16 (2023). https://doi.org/10.3390/en16010336.

Conference Proceedings

[3] E. Abdelhameed, D. Tsuru, H. Tashima, PIV Measurement of Diffusion Behavior of Intake-Tube-Injected Methane Jet Using High-Pressure Circular Wind Tunnel, 15th Int. Symp. Part. Image Velocim. 1 (2023), San Diego, In-press.

[1] E. Abdelhameed, D. Tsuru, H. Tashima, T. Wakasugi, T. Sako, Consideration of Combustion Improvements of Lean-burn Gas Engine with Pre-combustion Chamber, CIMAC Congr. 2023, Busan, In-press.

[2] E. Abdelhameed, H. Tashima, An investigation on the Behavior of the torch flame in the LBGE combustion process, in: Proc. Int. Exch. Innov. Conf. Eng. Sci., Fukouka, 2022: pp. 207–214. https://doi.org/10.5109/5909093.

[3] E. Abdelhameed, T. Aoyagi, H. Tashima, D. Tsuru, PIV measurements of entrainment process of directly injected media in internal combustion engines, 14th Int. Symp. Part. Image Velocim. 1 (2021), Chicago 1–10. https://doi.org/10.18409/ispiv.v1i1.184.

Table of Contents

List of Figures

List of Tables

Nomenclature

Abbreviations	
ATDC	After Top Dead Center
CAS	Constant Air Suction
COC	Constant Oxygen Charge
CCD	Charge-coupled device
EGR	Exhaust gas recirculation
IMEP	Indicate Mean Effective Pressure
IMO	International Maritime Organization
RCEM	Rapid Compression Expansion Machine
TCM	Two-Color Method
TDC	Top Dead Center
WFE10	Water-in-Fuel Emulsion, 10% water, and 90% fuel, v/v%.
WFE25	Water-in-Fuel Emulsion, 25% water, and 75% fuel, v/v%.
WFE40	Water-in-Fuel Emulsion, 40% water, and 60% fuel, v/v%.
DF	Dual Fuel
EGR	Exhaust gas recirculation
GHG	Greenhouse Gas
GI	Gas Injection
GO	Gas oil
HFO	Heavy Fuel Oil
HRR	Heat Release Rate
ICE	Internal combustion engine
IMO	International Maritime Organization
LNG	Liquefied Natural Gas
MARPOL	The International Convention for the Prevention of Pollution from Ships
NG	Natural Gas
RCEM	Rapid Expansion-Compression Machine
THC	Total hydrocarbon
WEF	Water-Fuel Emulsion
X-DF	Premixed Dual Fuel
M13N	87%Methane and 13% Nitrogen
M17.5N	82.5%Methane and 17.5% Nitrogen
M24N	76%Methane and 24% Nitrogen
M14.4C	85.6%Methane and 14.4% Carbon dioxide
M16C	84%Methane and 16% Carbon dioxide
M 17.5C	82.5%Methane and 17.5% Carbon dioxide
ASOI	After Start Of Injection
ATDC	After Top Dead Center
BSFC	Brake-Specific Fuel Consumption
BTDC	before Top Dead Center
BTE	Brake Thermal Efficiency
CVC	Constant Volume Chamber

DF	Dual Fuel
DTBP	Di-tert buyl peroxide
EFI	Electronically controlled Fuel Injection
HSMS	High-Speed Measurement and System Controller
IMEP	indicated mean effective pressure
ITE	Indicated thermal efficiency
NG	Natural Gas
RCEM	Rapid Expansion-Compression Machine
TEGMME	tri-ethylene glycol mono methyl ether
M20H	80% Methane and 20% Hydrogen
M30H	70% Methane and 30% Hydrogen
M50H	50% Methane and 50% Hydrogen
PIV	Particulate Image Velocimetry

Nomenclature	
$\frac{dQ}{d\theta}$	Heat release rate based on crank angle, J/deg.
$\frac{dP}{d\theta}$	Pressure-change per crank angle, MPa/deg.
$\frac{dV}{d\theta}$	Volume-change rate per crank angle, m^3/deg
P	Instantaneous in-cylinder pressure, MPa
N_o	Monochromatic radiance, W/(m^2·μm)
Pr	Pressure ratio, which is the ratio of the injection pressure to the chamber pressure, [-]
P_i	Injection pressure, [MPa]
P_{ch}	Chamber pressure, [MPa]
CA10	Crank angle at which 10 % of heat is released, [degree]
CA50	Crank angle at which 50 % of heat is released, [degree]
CA90	Crank angle at which 90 % of heat is released, [degree]
Pr	Pressure ratio, which is the ratio of the injection pressure to the chamber pressure, [-]
P_i	Injection pressure, [MPa]
κ	Specific heat ratio
θ	Crank angle, degree
V	Instantaneous in-cylinder volume, m^3
T_b	The black body temperature, K
^{o}CA	Degree of Crank Angle

Chapter 1

Introduction

1.1. Background

The diesel engine has experienced substantial growth and change since its conception in the late nineteenth century. The original concept, developed by German inventor Rudolf Diesel, was based on the notion of using compression heat to ignite fuel rather than a spark plug as in a standard gasoline engine. This enabled more efficient and dependable combustion, and the diesel engine rapidly became popular as a source of power for a wide range of applications. Diesel technology evolved and improved over the twentieth century, and diesel engines got more powerful, efficient, and dependable. Early diesel engines were frequently employed in ships, railroads, and heavy-duty trucks, as well as in power plants to generate electricity. Diesel engines were first used in passenger automobiles in the 1950s, and they soon gained popularity due to their enhanced fuel efficiency and durability. Following this, more advanced diesel technologies like as common rail injection and turbocharging were developed, allowing for even better economy and performance. Diesel engines are now found in a variety of vehicles and equipment, including automobiles, trucks, buses, boats, and industrial and agricultural gear. They are also frequently employed in power generation and continue to be a vital source of energy for a wide range of applications. Despite the fact that the EV shift trend has just emerged in automotive sectors globally, diesel engines continue to be one of the most efficient power sources, particularly in industrial and marine propellant areas. Further improvements should be made to enhance thermal efficiency and the use of GHG-free fuels such as ammonia and H_2. Because the diesel combustion process is thought to reflect mixture formation and distribution in a spray, fuel injection is undoubtedly one of the most important factors influencing the combustion process in diesel engines, and numerous studies on the development process of a diesel spray have been conducted [1].

1.2.Diesel Engine environmental impact and its regulation

In recent years, there has been a greater emphasis on decreasing diesel engine emissions in order to address concerns about air pollution and climate change. Apart from water vapor and carbon dioxide, which are not harmful, the principal components of exhaust gas emissions are nitrogen and nitrogen oxides [2,3]. Aside from those pollutants, the combustion process produces very little quantities of carbon monoxide, particulate matter, and NOx. Nitrogen oxides in the atmosphere include N_2O, NO, NO_2, NO_3, N_2O_4, and N_2O_5 [4]. When addressing nitrogen oxides, the word "NOx" refers to nitrous oxide

(N_2O), nitrogen monoxide (NO), and nitrogen dioxide (NO_2), all of which are regarded "fresh" nitrogen oxides from a photochemical standpoint since they enter the atmosphere in their respective gaseous forms [5]. These gases are produced by combustion processes, which involve the high temperatures necessary to make nitrogen oxides. The majority of NOx released by diesel engines is "Thermal NOx," which is created by direct interactions of nitrogen and oxygen in a high-temperature environment [6]. By 95%, nearly all the NOx generated by combustion processes is NO, with only a minuscule 5% being NO_2 [4]. After being discharged into the environment, NOx can react with organic matter, generating Ozone and causing lung damage and lowering lung function, particularly in youngsters and the elderly [4]. Meanwhile, long-term respiratory exposure to nitrogen oxides may result in asthma [7].

As a result, many regulations have been established to regulate diesel engine emissions. These laws are intended to reduce the amount of emissions that diesel engines emit into the atmosphere, and they often define limitations on the quantities of certain pollutants that diesel engines are permitted to produce. Through the Framework Convention on Climate Change, the United Nations has developed a framework for controlling diesel engine emissions (UNFCCC). This framework, which has been widely appreciated of nations worldwide, provides a global framework for lowering emissions from diesel engines and other sources. In the United States, for example, the Environmental Protection Agency (EPA) has established Clean Air Act emissions regulations for diesel engines. These rules regulate NOx, PM, and other pollution emissions from diesel engines used in on- and off-road vehicles and equipment. Similarly, the European Union created Euro emissions rules, which restrict NOx, PM, and other pollutants emitted by diesel engines used in passenger cars, lorries, and other vehicles. Other nations and regions, such as China and India, have also created their own diesel engine pollution guidelines.

Not only on-road trucks but also on the marine sector, the International Maritime Organization (IMO) is the primary regulatory body for marine sector emissions. IMO has established several different regulations that apply to marine engines, including the International Convention for the Prevention of Pollution from Ships (MARPOL), which sets limits on the levels of various pollutants that marine engines are allowed to emit. IMO strictly regulated the emissions by issuing a series of Tiers starting from Tier I in 2000 to Tier III in 2016 [8]. Those Tiers aimed to gradually decrease the NOx emissions by 80% in Tier III [9].

The marine sector is dealing with 80% of worldwide trade. This large sector produces 2.89% of the Greenhouse gases (GHG) [10]. The marine sector encompasses a wide range of vessels, from small recreational boats to large commercial ships. These boats range in size from small dinghies to large yachts, and they are used for a variety of activities such as fishing, watersports, and cruising. In addition to recreational boats, there are also a significant number of commercial vessels operating in the marine sector (Figure 1.1 1(a)). These vessels include cargo ships, tankers, and container ships, which are used to transport goods and materials around the world. According to industry estimates, there are currently around 50,000 commercial vessels in operation globally. The marine sector is a crucial part of the global economy, and it consists of various types of vessels, including recreational boats, commercial vessels, and passenger ships like cruise ships and ferries. In 2019, around 30 million people went on a cruise, and this number is expected to increase in the coming years. Recreational boats make up the largest percentage of vessels, followed by commercial vessels and passenger ships. The leading companies in the marine sector industry in 2020 were MAN and Wärtsilä, with 38% and 34% of the market share, respectively, as shown in Figure 1.1 (b).

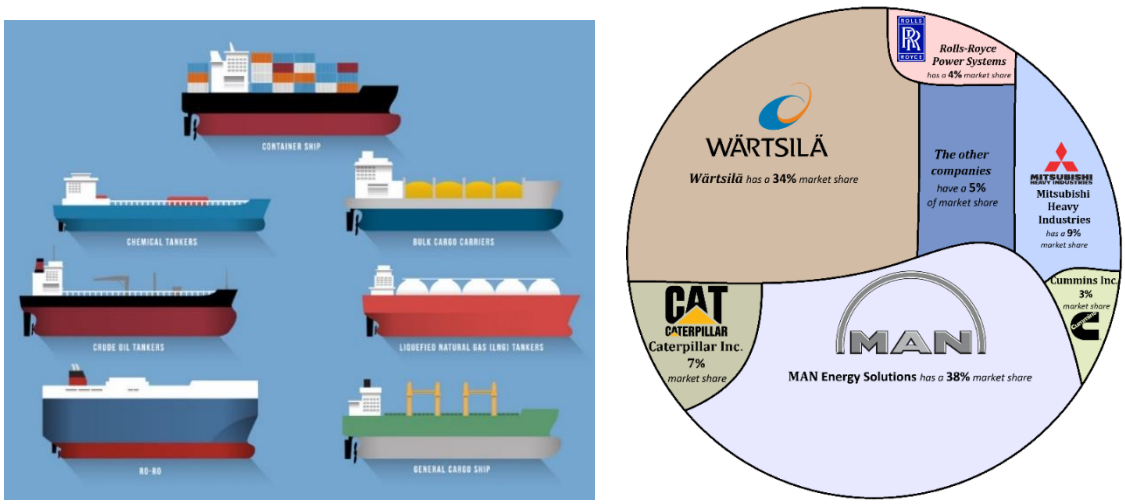

(a) (b)

Figure 1.1 Marine sector a) ship types in marine sector b) market share for each company

1.3.Bibliometric analysis

In the past decades the researchers shed the light on the diesel engine performance, combustion, and its effects on the environment. When researching appropriate study

subjects, bibliometric analysis is an effective tool [11]. Using this method, one might establish connections between many aspects of a specific subject. Bibliographic mapping identifies the most frequently mentioned publications in the literature and establishes links between them. A web search for "Diesel" AND "Engine" in the Web of Science database over the last two decades revealed 10841 papers from 2004 to 2013, 23709 papers from 2014 to until April 2023. The bibliometric analysis in Figure 1.2 shows the dominant approaches in the research field within the last two decades. From 2004 and for a decade, the engine research focused on the biofuels including biodiesel and their blends on the engine performance and emissions and partly the engine combustion. This appears from the red cluster in Figure 1.2(a). This intense biodiesel research direction included some kind of early attention to the nano particles and hydrogen.

Gradually, in the following decade the research in the engine field quantitively doubled. The biodiesel production from different feedstocks was increased and their effects on the engine extended to cover not only the performance but only the In-cylinder combustion. Similarly, the nano addition to the engine fuel including the biodiesel was strengthened to cover their impact on the engine combustion and emissions. Also the particulate matters in the exhaust gases seem to be deeply analyzed as the nano-particles work as catalyzer in the engine combustion, it means it shall exhausted into the emissions. Not only biodiesel attracted increased attention but also Hydrogen, Ammonia. Hydrogen and methane have been studied as secondary fuel in the engine in the dual-fuel technique mainly as premixed fuel in diesel engines. finally, the after-treatment system selective catalytic reduction (SCR), becomes red-hot in the marine sector for its success to decrease NOx emissions by up to 90%. Some other methods such as waste heat recovery and optimizing engine efficiency just came to the scene.

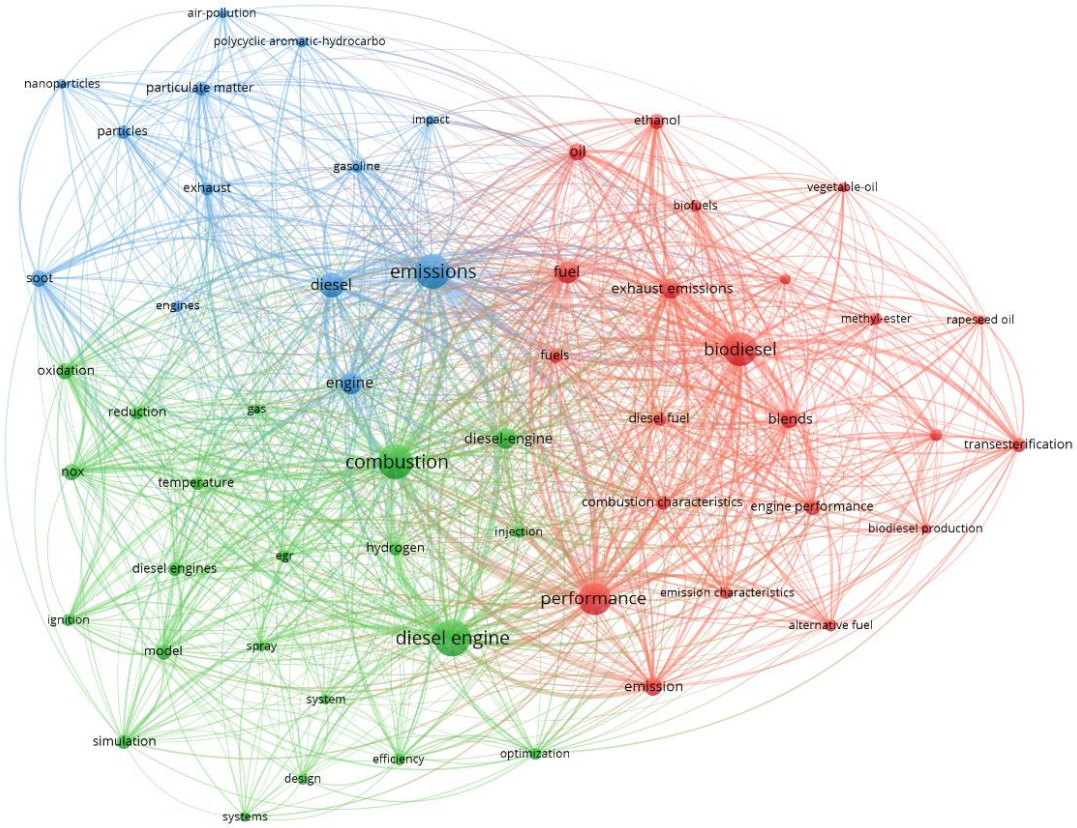

(a)

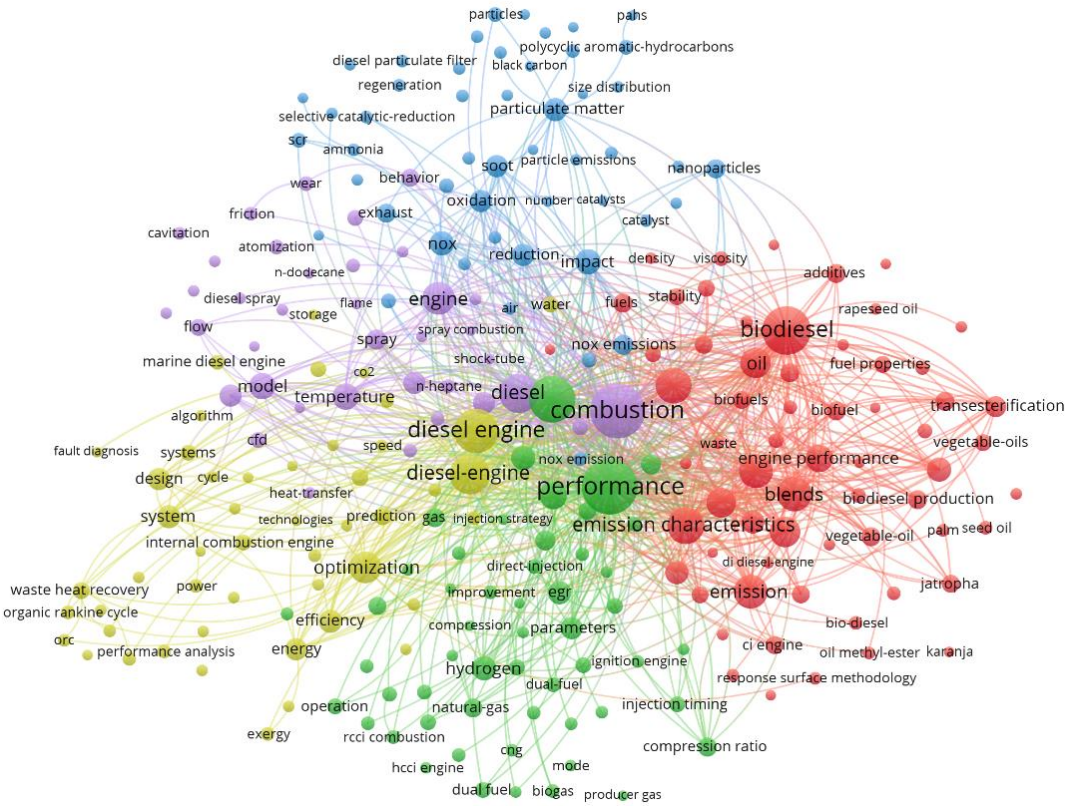

(b)

Figure 1.2 Bibliometric network mapping produced in VOS viewer using search terms of "Diesel" AND "engine" 2004-2023. a) 2004-2013 b) 2014-2023

1.4.Emissions treatment techniques in Diesel engines

Several strategies for reducing the generation of nitrogen oxides (NOx), a key contributor to air pollution, have been developed and applied in marine diesel engines. Therefore, some technologies have been implemented to decrease NOx formation in the last decade [12], including Fuel blending [13], Fuel additives [14], Double-Stage Turbocharging, Fuel Injection Strategy [15], Direct Water Injection (DWI), dual-fuel combustion strategy [16,17], Scavenging Air Moisturizing (SAM), Selective Catalytic Reduction (SCR) [18], nonthermal plasma (NTP) [19], Seawater Flue Gas Desulphurization (SWFGD) [20,21], Exhaust Gas Recirculation (EGR) [22–24], and Water-in-Fuel Emulsion (WFE) [25–27]. Each of these technologies has benefits and drawbacks, and the ideal option may differ based on the exact demands and requirements of a certain application. Overall, the use of these technologies is helping to reduce the emissions from marine diesel engines and to improve air quality.

1.4.1.Fuel blending

Fuel blending is the process of combining two or more fuels to produce a blended fuel that decreases pollution emissions such as nitrogen oxides and particulate matter. Murugesan et al. [28] conducted a comprehensive investigation on the influence of Euglena Sanguinea biodiesel-diesel blends with hydrogen and Graphite oxide nanoparticles as a fuel on diesel engines. The results showed that using 20% biodiesel with regular diesel reduces BTE by 4.1% while also marginally lowering CO, THC, and smoke emissions. As 80 ppm nanoparticles were used, CO emissions were reduced by 10.2% when compared to diesel fuel. The addition of hydrogen to the Nano-biodiesel blends enhanced the BTE and resulted in a reasonable reduction in CO, smoke, THC, and NOx concentrations in the exhaust gases. Ganesan et al. [29] performed an experimental study to evaluate the effect of combining n-pentanol cottonseeds with oil biodiesel on the engine's combustion, performance, and emissions characteristics in dual-fuel mode. The results revealed a 45 percent and 44.2% decrease in smoke and NOx, respectively. Meanwhile, THC and CO emissions increased dramatically, particularly at medium load. When utilizing 20% n-pentanol in the Reactivity-Controlled Compression Ignition (RCCI) mode, the Brake Thermal Efficiency (BTE) improved by 7%.

1.4.2.Fuel additives

Chemical substances added to fuel to improve its qualities and mitigate emissions are known as fuel additives. They can be mixed into diesel, kerosene, or other fuels to improve combustion efficiency, decrease engine wear, and reduce emissions. To achieve better emission reductions, fuel additives can be employed alone or in conjunction with other technologies. Kumar et al. [30] investigated the impact of hydrogen addition on the combustion duration of a diesel engine powered by tri-ethylene glycol mono methyl ether (TEGMME) and diesel. The results revealed that using diesel-TEGMME enhanced the combustion length based on diesel, however using hydrogen reduced the combustion duration for the diesel-TEGMME blends by 21.5%. Vinayagam et al. [31] propose a novel method for lowering hydrocarbon and carbon monoxide concentrations in diesel engine emissions. The efficiency of the catalytic impact of the nano-additives to the Silkworm Oil Methyl easter as a post-combustion technique in terms of THC and CO reduction was investigated. According to the findings, the post-combustion approach efficiently decreases CO and THC emissions by 85% and 90%, respectively.

1.4.3.Double-Stage Turbocharging

Double-stage turbocharging utilizes two turbochargers to compress air into the engine. As a result, it increases fuel efficiency and reduces emissions. Double-stage turbocharging is becoming more frequent in today's internal combustion engines to boost efficiency and output. To compress the air before it enters the engine, two turbochargers are installed in series. The first turbocharger is designed for slower speeds, while the second is designed for higher speeds. Higher compressed air may be supplied into the engine with this technique, resulting in more driving power. In many cases, dual-stage turbocharging is helpful. The first advantage is higher fuel economy as a result of the engine's increased efficiency. Because of the double-stage turbocharging, which compresses the air entering the engine, more air is available to combine with the fuel during combustion. As a result, gasoline is used more efficiently, using less fuel to provide the same amount of power. As a result, by reducing fuel consumption, double-stage turbocharging improves both the environment and customers' money. Second, using multiple turbochargers reduces emissions. Modern engines are designed to generate less emissions during combustion in order to fulfill severe emission rules. The use of double-stage turbocharging reduces emissions of carbon dioxide, nitrogen oxides, and particulate

matter. Because it boosts engine efficiency while requiring less fuel to maintain a consistent level of power, double-stage turbocharging reduces pollutants. Last but not least, a two-stage turbocharger boosts engine performance. More air may be combined with the fuel using double-stage turbocharging, resulting in a more efficient combustion process. As a result, the engine generates greater power, which is advantageous in a range of situations, such as racing automobiles and heavy-duty trucks. There are several disadvantages to employing a dual-stage turbocharger. The high cost of this technology is one of the key obstacles. The usage of two turbochargers might raise maintenance expenses due to the engine's complexity. Often, turbo lag, a delay in engine response caused by the turbochargers' need for time to spool up, occurs when two turbochargers are used.

1.4.4.Fuel Injection Strategy

Fuel injection strategies involve the timing and amount of fuel injected into the engine. Optimizing fuel injection can improve combustion efficiency and reduce emissions. Imhof et al. [32] developed an RCEM machine with marine diesel engine dimensions. The machine investigated the high injected NG simulating GI engine experimentally. The results showed a comparable heat release rate for the diesel and GI methods. Back Diffused Laser was used to study the characteristics of the flame. The gas flame showed a lower brightness than the diesel and, as a result, lower NOx emission reaching a 75% reduction. Nayak et al. [33] studied how advanced injection timing at different loads affected the engine performance, emissions, and combustion characteristics. Different Waste Oil Methyl Ester blends were injected as a primary fuel, while biogas was introduced through the inlet manifold. The results showed that THC, NOx, soot, and CO were significantly reduced. Zarrinkolah et al. [34] investigated the effects of direct injector spray angles on the methane slip. Methane slip is reduced by 16.4% and 42.5% when the spray diesel angle is increased from 60° to 90° and 120°. As a result, NG engine emissions could be controlled by simpler processes than pretreatment or post-treatment. Using a variety of biodiesels, Jaliliantabar et al. [35] examined the effects of pilot diesel timing and the EGR system on decreasing exhaust emissions. The study's findings showed that the engine's reaction to varying injection strategies and EGR applications was affected by the fuel's different chemical and physical properties. Using the coffee methyl-ester reduced the combustion duration by 17.7% compared to diesel.

EGR and pilot injection (up to 86% and 29.3%, respectively) reduced NOx emission, but the combustion quality was altered due to changes in the combustion efficiency.

The time and amount of fuel injected into the engine are aspects of fuel injection techniques. Fuel injection optimization can enhance combustion efficiency and lower emissions. Imhof et al. [32] developed an RCEM machine with the specifications of a marine diesel engine. The high injected NG imitating GI engine was studied experimentally by the machine. The results revealed that the heat release rate for the diesel and GI techniques was equivalent. Back Diffused Laser was used to investigate the flame's properties. The gas flame was brighter than the diesel flame, resulting in a 75% reduction in NOx emissions. Nayak et al. [33] investigated how improved injection time affects engine performance, emissions, and combustion parameters under various loads. As a main fuel, several Waste Oil Methyl Ester mixes were injected, while biogas was supplied through the intake manifold. THC, NOx, soot, and CO levels were dramatically reduced, according to the findings. Zarrinkolah et al. [34] examined the methane slip effects of direct injector spray angles. When the spray diesel angle is adjusted from 60° to 90° and 120°, methane slip is reduced by 16.4% and 42.5%, respectively. As a consequence, rather than pretreatment or posttreatment, NG engine emissions might be regulated by simpler techniques. Jaliliantabar et al. [35] investigated the effects of pilot diesel timings and the EGR system on exhaust emissions using a variety of biodiesels. The study's findings revealed that the engine's response to varied injection techniques and EGR applications was influenced by the fuel's chemical and physical qualities. When compared to diesel, using coffee methyl-ester reduced combustion time by 17.7%. Although EGR and pilot injection lowered NOx emissions by up to 86% and 29.3%, respectively, the combustion quality was altered due to changes in combustion efficiency.

1.4.5.Direct Water Injection (DWI)

Direct water injection involves introducing a tiny quantity of water into the combustion chamber of an engine. This contributes to lower peak combustion temperatures and lower NOx emissions. Water injection into the combustion chamber through a separate nozzle was proven to lower NOx emissions by 50-60%, although at the cost of higher fuel consumption. The dual injection valve, which injects both fuel and water, is critical to the design concept. The combination nozzle is equipped with two needles, one for injecting water and the other for injecting fuel. Water injection absorbs the heat the combustion chamber before the fuel is burned, reducing the production of

nitrogen oxides (NOx). A high-pressure water pump is used to achieve water pressures of 200-400 bar. Before being supplied to the injectors through a pressure control valve, the water is filtered and the pressure pulses are dampened. Water injection time may be easily adjusted using electronic controls. Injecting water for a longer or shorter amount of time changes the water/fuel ratio. Sun et al. [36] used a three-dimensional simulation model to investigate the effect of direct water injection on marine diesel engines. Water quantity was shown to have a negative influence on cylinder pressure, temperature, indicated power, and NOx emissions. NOx emissions were decreased by up to 55.6% when DWI was applied to the engine during the compression stroke. Water injection temperature has little effect on marine engine combustion and emissions. The reported power decreased when the water injection happened during the compression stroke. The late combustion phase water injection timing, on the other hand, resulted in an increase in indicated power. It is possible to reduce NOx emissions by timing water injection during the compression stroke. NOx emissions are decreased by 40% when water is injected during the compression stroke than when water is injected during the combustion phase.

1.4.6.Dual-fuel combustion strategy

Dual-fuel combustion is the use of two fuels in a single engine, commonly natural gas and diesel. This results in more complete combustion and lower emissions. LNG has gained popularity as a hydrogen fuel source since it is sulfur-free and low in carbon. LNG can decrease carbon dioxide emissions from heavy fuel oil by roughly 28% [37]. Recently, there has been a continuous growth in global LNG supplies [38]. Natural gas (NG) is a mixture of gases, the majority of which are methane [39]. This high methane concentration allows NG to have a distinct combustion behavior in both a diffusive combustion engine and a premixed combustion engine. Premixed and direct injection were the two major strategies utilized to use NG as a dual fuel (DF) in marine diesel engines [39]. MAN employed direct injection to produce its first ME-GI engine in 2012, whereas Wärtsilä has been manufacturing its series of DF engines based on premixed technology since 1987 [40]. Yu et al. [41] modeled and evaluated the combustion of a maritime two-stroke dual-fuel engine powered by diesel and Diesel Ignited Natural Gas (DING). The combustion time for the diesel case was reported to be greater than that of the DING case. In addition, when compared to diesel, DING considerably reduced local high-temperature regions by an average of 8%. In both radial and axial directions, the flame propagation speed was quicker than that of the diesel fuel flame. Lee et al. [42]

investigated the impact of different NG replacement percentages on diesel combustion and soot emissions. NG extends the flame area and delays ignition. NG enhances the premixed flame and reduces soot. High NG replacement ratios, on the other hand, decrease flame spread in DF mode.

Due to cold spots in the lean-burn combustion for the premixed dual-fuel engine [43], gas engines may produce methane as a methane slip [44], which contributes 25 times more to global warming than CO_2 [45]. As a carbon-free, low-ignition, and highly flammable fuel [46], hydrogen was used in premixed DF engines [47] to reduce CO_2, methane slip, and HC emissions [48]. Meanwhile, the researchers have been investigating the use of methane-hydrogen in diesel engines in order to address hydrogen combustion problems (such as backfire, pre-ignition [49], and anomalous combustion [50]. Cheng et al. [51] used a diesel pilot to examine methane-hydrogen combustion in a single-cylinder diesel engine. The use of hydrogen lowered the combustion time by 45%, increased thermal efficiency by 10%, and reduced the cycle-to-cycle pressure variation by 50%. Kumar et al. [52] examined the effect of di-tert-butyl peroxide (DTBP) on diesel engine emissions and performance. The addition of hydrogen to diesel-DTBP enhanced BTE while decreasing NOx and CO emissions. The Chemkin software was used by Luo et al. [53] to create a 3-D computational fluid dynamics model of a diesel engine with 53 species and 325 reactions. Adding 15% hydrogen at full load reduced BSFC by 4.6% while increasing braking power by 10.3%. Furthermore, utilizing 5% hydrogen increased NOx emissions by 34.5%. Liu et al. [54] developed an automotive-size diesel engine to directly inject hydrogen with a hydrogen replacement of 20-90%. The best injection timing was 40^{o}CA BTDC, which increased IMEP/efficiency by 13.3% while decreasing CO_2 by 85.9%. Liu et al. [55] investigated a direct-injected hydrogen and diesel engine. Early hydrogen infusion increased the rate of heat emission. Combustion-induced noise is decreased by 6 dB at 50% hydrogen substitution at 40^{o}CA BTDC direct injection timing, and NOx emissions are less than 11 g/kWh.

1.4.7.Scavenging Air Moisturizing (SAM)

Scavenging air moisturizing is the process of adding water to the engine's intake air in order to improve the humidity of the air entering the engine. This contributes to a reduction in NOx emissions. Scavenge Air Moisturizing (SAM) technology, also known as Humid Air Engine technology, is a method for lowering engine temperatures and lowering emission levels. The SAM system uses seawater to cool and humidify intake air

after the compressor, then fresh water to eliminate any salt that might cause engine damage. A microcomputer manages the system's particularly developed pieces and supporting hardware. SAM features a saltwater injection stage that can offer approximately 100% humidification and cooling for scavenge air. Freshwater stages remove salt from the system, although salt build-up can occur. This is resolved by chilling the air using an air cooler and creating extra freshwater for stage 2, which is then routed upstream. As a result, the salt level of the freshwater phases may be regulated. Mito et al. [56] utilized the scavenge air cooling in improving the performance of marine diesel engine. This research introduces an innovative method for running single and dual pressure steam power generating cycles by reusing the heat rejected during the scavenge air cooling process and the exhaust gas. To further increase overall efficiency, a thermodynamic study of the suggested systems was carried out to determine the best operating parameters. Each component's energy/exergy efficiency was calculated in addition to its exergy destruction. To evaluate practicality and output power under non-ideal conditions, a performance analysis was carried out. The environmental and financial benefits of the proposed designs are weighed and evaluated. Overall, the data demonstrate that the proposed cycle improved efficiency by 5.1 % over the conventional system, and it also boosted power production by 1210 kW, or 9.7 %. The described technology also dramatically improved exergy efficiency by 6.6%. In addition, annual carbon dioxide emissions were cut by 4790 metric tons thanks to the waste heat recovery system.

1.4.8.Selective Catalytic Reduction (SCR)

Meanwhile, the most often employed approaches for regulating diesel engine emissions in the maritime industry are exhaust gas aftertreatment technologies such as selective catalytic reduction (SCR) and lean NOx catalysts (LNCs) [57,58]. These technologies are often put in the vessel's exhaust system and function similarly to those utilized in the automobile industry. However, there are some similarities between the processes employed in the automotive and maritime industries. Because of the larger potential environmental effect of marine ships, regulation standards for diesel engine emissions in the marine industry are often stricter than those in the automobile sector. As a result, the procedures employed in the maritime industry to regulate emissions may be more modern and complex than those used in the car sector. Furthermore, the operating conditions for diesel engines in the automotive and marine industries might be extremely different, which can have an impact on the approaches employed to regulate emissions.

Diesel engines in automobiles, for example, often run at lower speeds and loads than those in maritime boats, which might impact the design and efficacy of pollution control devices utilized. The employment of a catalyst in SCR converts NOx emissions into nitrogen and water. SCR systems may cut NOx emissions by up to 90%.

1.4.9.Nonthermal plasma (NTP)

Nonthermal plasma (NTP) is a method that has gained popularity in recent years as a potential means of mitigating environmental concerns. High-voltage electrical discharges are employed to generate plasma, which creates reactive species capable of oxidizing and breaking down contaminants. NTP has decreased the emissions of various pollutants, notably nitrogen oxides (NOx). NTP can be used in two ways to reduce NOx emissions. The first advantage is that it can convert NO to NO2, which is easier to filter out of pollutants. Plasma-generated reactive oxygen species such as ozone and hydroperoxyl radicals convert NO to NO2. Unlike traditional catalytic converters, which need temperatures above 200 °C, this reaction may occur at considerably lower temperatures. Second, by degrading volatile organic compounds (VOCs) in exhaust streams, NTP can reduce NOx emissions indirectly. Ground-level ozone is hazardous to both human health and the environment, and it is produced when volatile organic compounds (VOCs) react with nitrogen oxides (NOx). NTP can reduce the likelihood of volatile organic compounds (VOCs) to react with nitrogen oxides (NOx). The use of catalysts, which might be expensive and only need to be updated seldom, is unneeded with NTP. Because NTP is a continuous process, it may be used in conjunction with other pollution control technologies like as catalytic converters to obtain even larger emission reductions. NTP has shown promising results in reducing NOx emissions in a variety of applications, including diesel engines, gas turbines, and power plants. However, NTP is not without its difficulties. The massive amount of energy required to produce plasma is an issue. As a result, the strategy may become less cost-effective than other means of lowering emissions. Secondary pollutants, like as ozone, may be produced by the plasma, affecting both human health and the environment.

1.4.10.Seawater Flue Gas Desulphurization (SWFGD)

SWFGD includes scrubbing exhaust emissions with saltwater to eliminate sulphur dioxide and other pollutants. This can help in lowering emissions and improving air quality. Yang et al. [20] investigated NOx and SO_2 removal from simulated ship

emissions using wet scrubbing based on seawater electrolysis technology. Increases in active chlorine concentration, NO input concentration, reaction temperature, and concentrations of coexisting gases (CO_2 and O_2) all improved NOx removal, whereas increases in gas flow rate had the reverse effect. The pH of the electrolyzed seawater had a substantial impact on the effectiveness of NOx removal. The ability of single and multiple stage reactors to remove NOx and SO_2 concurrently was then explored. The new technology based on a $Na_2S_2O_8$/urea composite system was used by Xi et al. [59] to concurrently eliminate NO and SO_2 from marine diesel engine emissions while lowering nitrate residues in cleaning wastewater. Overcoming SO_2 release and efficiently absorbing NO needs a temperature over 60°C and a $Na_2S_2O_8$ concentration in the $Na_2S_2O_8$/urea solution of more than 0.05 mol/L. Urea efficiently reduced residual nitrate content and increased NO absorption at values less than 2 mol/L.

1.4.11.Exhaust Gas Recirculation (EGR)

Exhaust gas recirculation (EGR) is a technology used in internal combustion engines to minimize nitrogen oxide (NOx) concentrations [38,43]. It returns a part of the engine's exhaust gas to the combustion chamber, where it is mixed with the incoming air and fuel combination. This process reduces the quantity of oxygen available for combustion, lowering peak combustion temperatures, which might result in NOx generation. EGR can reduce NOx emissions by up to 90% [60] via three main mechanisms [61]: the thermal effect, which refers to the reduction in peak combustion temperature due to the presence of EGR [62], the dilution effect, which refers to the dilution of the air/fuel mixture with exhaust gas, lowering oxygen concentration and combustion temperatures [63], and the chemical effect, which refers to the reaction of EGR with NOx in the exhaust gas to form less harmful compounds. EGR, on the other hand, can raise the risk of knocking, extend after-burning, and result in increased amounts of carbon monoxide, soot, unburned hydrocarbons, and particulate matter. Water-in-fuel emulsions can improve brake thermal efficiency and lower NOx emissions while simultaneously increasing CO emissions. Low combustion rates and flame propagation are also disadvantages of the EGR and water techniques. The engine's unique circumstances, such as temperature history, boundary conditions, and operating parameters, can all have an impact on the combustion process and emissions output. Zhang et al. [64] investigated the effect of in-cylinder soot characteristics on oxidation performance under EGR conditions. The simulation focused on the oxidation-dominant

phase, which reported an increase in the rate of in-cylinder soot oxidation. EGR reduces soot oxidation by lowering flame temperature as well as oxygen and OH concentrations throughout the combustion. Gad et al. [65] conducted a thorough investigation on the effects of various mixes of mandarin peel waste oil and diesel on diesel engines. The analysis was then expanded to anticipate the impact of enriching the blends with propanol while taking EGR installation into account. The results revealed a decrease in HHR, CO, HC, and smoke opacity, but an increase in NOx emissions.

1.4.12.Water-in-Fuel Emulsion (WFE)

WFE usually involves emulsifying water and fuel. By promoting more complete combustion and lowering peak combustion temperatures, this can assist to minimize emissions. Mukhtar et al. [66] employed an emulsified fuel containing varying percentages of biodiesel and ethanol as a fuel for a single-cylinder diesel engine. The results showed that the test fuel's in-cylinder pressure and heat released rate surpassed those of pure diesel. The HRR profile exhibited a negative value during the ignition delay period due to evaporation. The most significant discovery of the study was that the load-shortening of the test fuel ignition delay time demonstrated verification of the micro-explosion phenomenon occurring without load, peak HRR, or combustion pressure. Park and Oh [67] investigated flame visualization, basic combustion properties, and emulsion fuel emissions. Emulsion fuel lowered nitrogen oxide emissions by 19.6% and smoke emissions by 66.3%. The in-cylinder pressure and heat release rate of the emulsion fuel were greater than those of the diesel fuel. Furthermore, the combustion time was 12.3% shorter than with pure diesel. Abdollahi et al. [68] investigated the impact of nano-emulsion biodiesel fuel on the combustion and emissions of a single-cylinder diesel engine. The results show that nano-emulsion fuel increased diesel engine power and torque by 4.84 and 4.65%, respectively, when compared to diesel fuel. The use of nano-emulsion fuel reduced CO, UHC, NOx, and soot opacity emissions by around 10%. However, there was a 7% rise in CO_2 emissions.

1.5.Novelties and Objectives within the Thesis

The main aim of this study is to investigate and develop methods in the diesel engine and gas engine aiming to reach as high-efficient engine considering the environmental impact. The project starts with a study of the spray of the diesel fuel and the gas jet. This project applied a Particle Image Velocimetry (PIV) measurements to

study the entrainment process of both diesel and high-pressure-direct-injected gas fuel, for the first time in engine field. The scattered light of the spray was suppressed by the fluorescence PIV, and the velocity field around the spray could be analyzed accurately. In the section, properties such as penetration length, cone angle, profile, and ambient velocity field around a diesel spray were investigated in detail using a pressured constant-volume chamber (CVC) and a dynamic 2D PIV system. The CVC has a cylindrical shape (bore 150 mm, height 350 mm). The PIV system revealed the velocity field around the spray and the spray silhouette in a laser sheet section. Also, these measurements were performed to the pre-chamber gas engine. A mixture entrainment process of torch flames is measured using the PIV.

After calculating the air entrained in the diesel spray and gas jet body the study moved to study the effect of applying different techniques on the combustion and the emissions of the diesel engine. In this context, we studied the effects of combining the EGR and WEF techniques on the NOx emissions in marine-scale diesel engine. Although some researchers studied WFE and EGR, the detailed combustion process and NOx reduction mechanism in WFE and EGR combination are still not well understood. As known, it is a competitive and challenging matter to calculate the NOx distribution or in-cylinder gas compositions versus crank angle by only analyzing measured data from experiments. Hence, A numerical calculation code was used to reveal the combustion mechanisms with WFE and EGR combination. This section is organized as follows: Early model calibration involved testing various EGR and WFE modes in a Rapid Compression Expansion Machine (RCEM) and obtaining shots, pressure measurements, and emissions data from in-cylinder combustion. Also, study two EGR system methods: Constant Air Suction (CAS) and Constant Oxygen Charge (COC) utilizing a 1D GT-Power simulation model and next, initiating and verifying the KIVA-3V code against the experimental data and using the calibrated model to simulate the combustion process and NOx emissions. The novelty of this study was primarily demonstrated in two following aspects. Firstly, a simulation platform based on the KIVA-3V code was established and utilized to calibrate the EGR and WFE with newly developed code to simulate the emulsified fuel. Secondly, the produced code was utilized to investigate a variety of EGR/WFE combinations and their impacts on in-cylinder combustion and NOx emissions. The objectives of this study are a) reveal combustion processes and NOx reduction mechanisms under the WFE/EGR conditions. b) Calculate the emulsified fuel concentration to shorten the afterburning duration in the EGR method. C) the effect of injection timing, pressure, and nozzle

diameter on the WFE is examined. From these techniques, WFE is expected to solve the problem of afterburning and improve thermal efficiency with a high NOx reduction ratio.

The project then moved to study the impact of diluting the methane gas as a direct injected fuel in marine diesel engine. Generally, direct injection technology seems to help reduce the rate of methane slip and decrease THC emissions. However, the gas is more challenging to burn than diesel because of the lower momentum of the gas jet. The lower momentum leads to lower gas-air entrainment, a gas-gas mixing phase. Based on this fact, adding an inert gas to the methane gas can increase the momentum somehow, like the Water-Fuel Emulsion (WEF). In other words, diluting methane with inert gas can be considered the gaseous version of the WEF. Although several researchers are keen to study the gas injection in the Dual fuel engine, limited studies concentrate on investigating the possibility of enhancing the Gas injection combustion by increasing the gas momentum. Consequently, in this section, an RCEM with an optical system has been used to study the effect of blending two inert gases, Carbon dioxide and nitrogen with methane as a direct-injected fuel along with the WEF. This study aims to a) Visualize the flame morphology using instantaneous direct photos from the in-cylinder for the different test fuels. b) Measure the flame penetration length of the test fuels using the instantaneous in-cylinder shadowgraphs. c) Calculate the heat release rate from the measured in-cylinder pressure to emphasize the in-cylinder combustion performance. d) Measure the produced emissions at each case to obtain the environmental impact from applying each fuel.

Hydrogen, as a zero-carbon content fuel, shines in the engine field as the magic solution to GHG. Yet, the hydrogen combustion never went smoothly. Several researchers utilized the methane-hydrogen blends as a premixed fuel in diesel engines aiming to reduce GHG emissions. Nevertheless, Premixed methane-hydrogen led to abnormal combustion and knocking [51]. Some other researchers investigated the direct injection of methane or hydrogen in the diesel engine cylinder, but the direct injection of the hydrogen-methane blend as a directly injected fuel in the diesel engine has yet to be studied. In this section we used a rapid expansion-compression machine (RCEM) with an optical system to examine methane-hydrogen blends as a direct-injected fuel that can eliminate backfire, pre-ignition, abnormal combustion, and knocking and promote a low methane slip in direct injection diesel engines. This work consists of two parts. The first is studying the methane-hydrogen blend jet characteristics in the nitrogen ambient by measuring the penetration of the methane and methane-hydrogen blends with the same

pressure ratio and studying the effect of different pressure ratios on the methane-hydrogen jet characteristics. The second is studying the combustion behavior of different hydrogen-methane blends using direct photos, shadowgraphs, in-cylinder pressure, and the emission characteristics under two different compression pressures. The novelty of this work is a) studying the jet characteristics of the methane-hydrogen blends under different pressure ratios. b) examining the combustion and emissions of the directly injected hydrogen-methane blends as a primary fuel.

1.6.Thesis Outline

The framework of the Ph.D. thesis consists of five main chapters as follows:

Chapter 1:-

Introduces the background and the literature review in the engine field.

Chapter 2:-

Outlines the main test rig applied in this study.

Chapter 3:-

Discusses the air entrainment in the diesel spray and methane jet based on experimental and numerical studies.

Chapter 4:-

Discusses applying Exhaust gas recirculation and water emulsion simultaneously in marine diesel engine based on experimental study and numerical calculations.

Chapter 5:-

Discusses applying inert gas as a methane dilution as a direct injection in marine diesel engine based on experimental study.

Chapter 6:-

Discuss applying Hydrogen-methane mixture as a direct injection in marine diesel engine based on experimental study.

Chapter 7: conclude the thesis results and findings.

Chapter 2

Materials & Methods

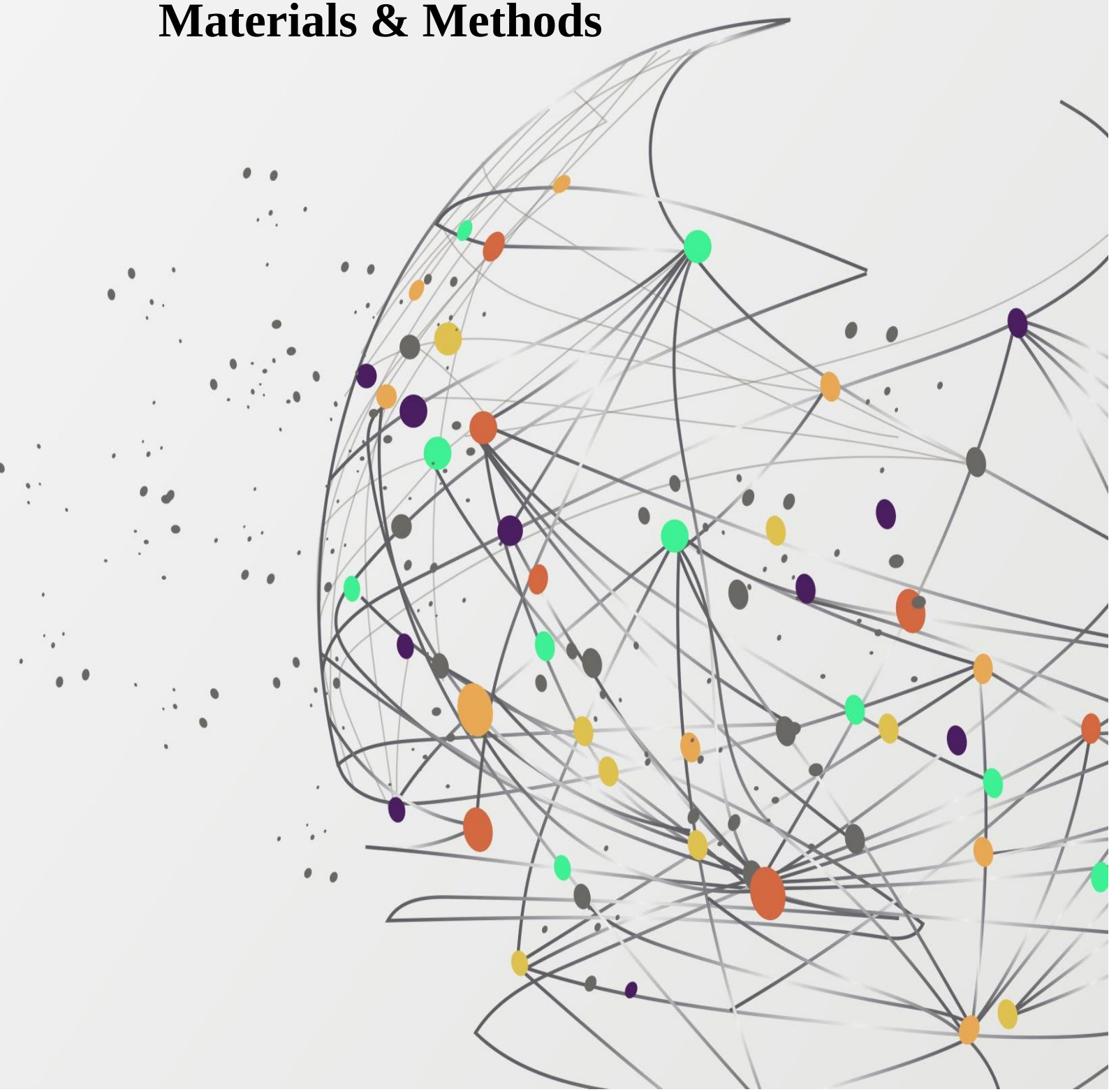

The specifications of the rapid compression expansion machine (RCEM) and its associated control system, as well as the optical system, are covered in this chapter. Moreover, this Chapter extends to cover the shadowgraph concept and the PIV measurements application. The RCEM in this chapter represents the primary equipment used in this thesis. It is worth noting that the cylinder head described below is intended to be adjusted as necessary to study the combustion of other types of engines (i.e., diesel engine, gas engine, and even constant volume chamber); any changes will be illustrated in the subsequent chapters.

2.1.Refraction of light in non-uniform media

This section describes how light refracts in a non-uniform medium before going deeper into the shadow graph and PIV approaches. Light travels in a straight path in a medium with a constant refractive index or light speed. However, if the temperature and pressure of the medium changed, the refractive index will also vary locally, causing light to refract according to a specified law. Consider the flow in the x-direction represented in Figure 2.1(a).

When a parallel ray is projected from the side in the z-direction, it is refracted upwards in the plane ABCD in the same way as light is refracted when it passes through an optical prism, where the refractive index (n) of the flowing material rises in the y-direction. Figure 2.1(b) shows an enlarged view of part of the plane ABCD in (a). Let the speed of light at y=y be C, and the speed of light at y=y+dy be $C + (\partial C/\partial y)dy$ is $\{C + (\partial C/\partial y)dy\}dt$. Therefore, the difference in traveling distance is $ds = -(\partial C/\partial y)(dydz/C)$, and the refraction angle $d\theta$ of the wavefront is described in Equation (2.1). Using the relationship n=C_0/C, the Equation can be substituted for Equation (2.2). The local refraction angle in the interval dz. The total refraction angle θ_y in the y direction from the plane AB to the plane CD of Figure 2.1(a) can be calculated by integrating Equation (2.2), resulting in Equation (2.3). When the refraction angle also changes in the x direction, the total refraction angle θ_x in the x direction is similarly given by the Equation (2.4). When considering a gas as a medium, its refractive index (n) is typically close to 1.

In this case, the Gladstone-Dale equation relates the refractive index to the density (ρ) of the gas as in this equation n=1+K ρ. Where K is a positive constant that depends on the type of airframe, but to be clearer, it varies slightly with wavelength. Applying this formula between the density and the refractive index, the refraction angles of Equations

(2.3) and (2.4) can be substituted into Equations (2.5) and (2.6). The density is determined approximately by the temperature, and the refractive index is given as a function of temperature.

$$d\theta \cong \frac{ds}{dy} = -\frac{dz}{C}\frac{\partial C}{\partial y} \tag{2.1}$$

$$d\theta = \frac{dz}{n}\frac{\partial n}{\partial y} \tag{2.2}$$

$$\theta_y = \int_0^d \frac{1}{n}\frac{\partial n}{\partial y}dz = -\frac{dz}{C}\frac{\partial C}{\partial y} \tag{2.3}$$

$$\theta_x = \int_0^d \frac{1}{n}\frac{\partial n}{\partial x}dz \tag{2.4}$$

$$\theta_x = \int_0^d \frac{K}{n}\frac{\partial \rho}{\partial x}dz \tag{2.5}$$

$$\theta_y = \int_0^d \frac{K}{n}\frac{\partial \rho}{\partial y}dz \tag{2.6}$$

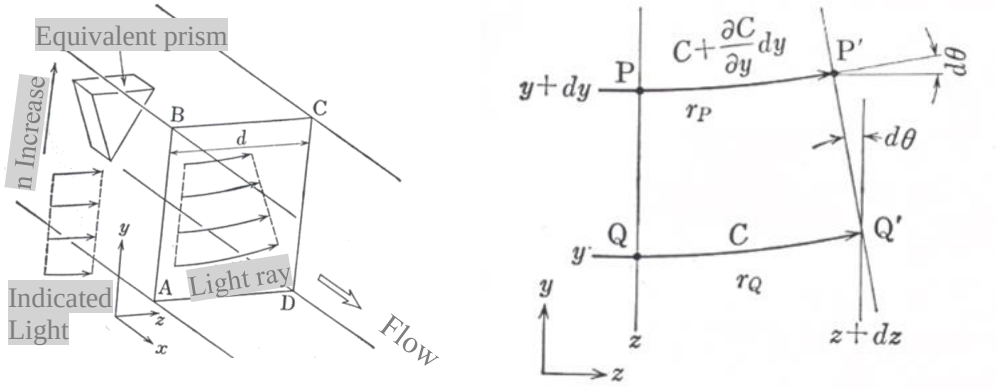

Figure 2.1 Light ray refraction theory

2.2.Shadow graph method

The principle and equipment are simple, and it has been used for the visualization of shock waves and wave phenomena for a long time. It utilizes the change in the refractive index due to the density change of the medium, Figure 2.2 shows its principle.

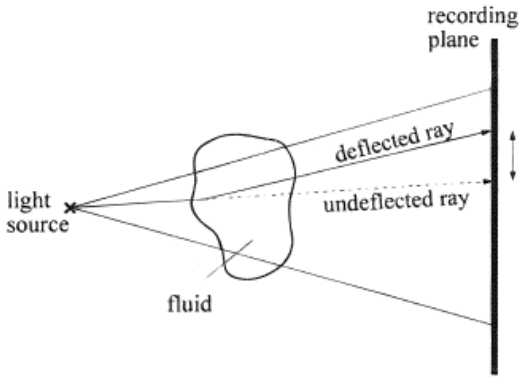

Figure 2.2 Shadow graph principle

Light from a point source S is bent when passing through an observation gas with nonuniform density and forms an image with gradations of brightness on the screen. For simplicity, we assume that the density change is two-dimensional and does not change in the x direction, which is perpendicular to the plane of the paper. From Equations (2.5) and (2.6), the refraction angle of the ray r_A passing through point A can be described as in Equations (2.7). As refractive index n=1+K ρ, assuming that the density varies only in the y-direction, the total refraction angle of the ray r_A can be described as in Equation (2.8). If the density gradient $d\rho/dy$ is constant in the y-direction, all light will be uniformly bent, and the brightness I of the image on the screen will not change. Therefore, it can be seen that the change in brightness ΔI appear due to the change in the density gradient. Therefore ΔI can be calculated as in Equation (2.9). Subsequently, the contrast on the screen or film surface obtained by the shadowgraph method is proportional to the second derivative of the gas density, that is, the change in the density gradient.

$$\theta_y = \int_0^d \frac{K}{n}\frac{\partial \rho}{\partial y} dz \tag{2.7}$$

$$\theta_y = \frac{Kd}{n}\frac{d\rho}{dy} \cong Kd\frac{d\rho}{dy} \tag{2.8}$$

$$\Delta I \propto \frac{\partial^2 \rho}{\partial x^2} + \frac{\partial^2 \rho}{\partial y^2} \tag{2.9}$$

2.3.Particle Image Velocimetry (PIV)

Particle Image Velocimetry (PIV) is an experimental technique for measuring fluid flow velocity. It includes injecting tracer particles into the fluid, which are illuminated by a laser sheet, and then tracking the motion of these particles over time with high-speed cameras. The fluid's velocity is then determined using the movement of the particles during a specified time interval, as shown in Figure 2.3.

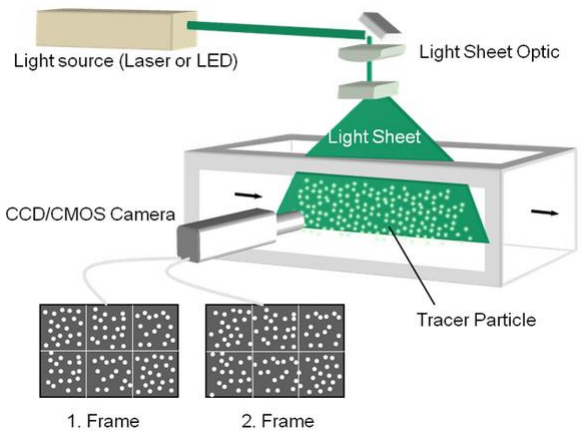

Figure 2.3 PIV principle

PIV is an analysis method that measures the two-dimensional components within a plane that are illuminated as a sheet light through a dedicated optical system. In PIV analysis, the relationship between the thickness of the sheet light and the out-of-plane velocity component perpendicular to that sheet light is important. However, it has been verified that reducing the sheet light's thickness to less than 1/4th of the thickness of the out-of-plane velocity component sheet has minimal influence on the measurement results. The thickness of the sheet light, z_0, is expressed by Equation (2.10), where f is the focal length of a convex lens, λ is the laser's wavelength, and d_b is the laser's diameter.

$$z_0 = \frac{4f\lambda}{\pi d_b} \tag{2.10}$$

PIV directly analyzes tracer particle images, and the scattering characteristics of tracer particles cause variations in the brightness and shape of the particles in the image, becoming a source of error in the measurement. Light scattering is mainly classified into Mie scattering by particles whose diameters are roughly equal to or larger than the wavelength λ of the incident light and Rayleigh scattering by smaller particles than λ. In PIV, light scattering occurs mainly due to Mie scattering, and the scattering intensity is expressed by the parameter a_P in Equation (2.10), where D is the particle diameter. For tracer particles in PIV measurements with particle diameters of 1 μm to several tens of μm at wavelengths of about 500 nm, the scattering intensity can be proportional to the square of the particle diameter.

$$a_p = \frac{\pi d}{\lambda} \tag{2.11}$$

Particles handled in PIV are subjects that resemble point light sources, and it is important to design the imaging system to image them brightly. The brightness of the lens system is inversely proportional to the square of the F-value (aperture value), and as the lens system's aperture is reduced, bokeh called Airy disks appear. The diameter of the Airy disk, d_a, is expressed by Equation (2.12), where M is the lateral magnification of the lens system, and F is the F-value. The size of the tracer particle on the imaging surface is expressed as the square root of the sum of the diameter of the actual particle and the diameter of the Airy disk.

$$d_a = 2.44\lambda(1 + M)F \tag{2.12}$$

Tracer particles cannot follow the fluid due to the inertia of the particles and show delayed behavior compared to the fluid. This followability is an important issue in PIV measurements, and various studies have been conducted. The Basset-Boussinesq-Oseen

equation shown in Equation (2.13) is a non-steady motion equation that describes particle motion.

$$\frac{\pi d^3}{6}\rho_p\frac{du_p}{dt} = 3\pi v\rho_f d(u_f - u_p) + \frac{\pi d^3}{6}\rho_f\frac{du_f}{dt} + \frac{1}{2}\frac{\pi d^3}{6}\rho_f\left(\frac{du_f}{dt} - \frac{du_p}{dt}\right) + \frac{3}{2}d^2\sqrt{\pi v}\int\frac{d\xi\left(\frac{du_f}{dt} - \frac{du_p}{dt}\right)}{\sqrt{t-\xi}} \quad (2.13)$$

u_P, u_f, ρ_P, ρ_f represent the particle and fluid velocities and densities, respectively. The left-hand side represents the particle's inertia. The first term on the right-hand side represents the influence of viscous resistance. The second term represents the direct effect of the density difference between particles and fluids. The third term represents the additional mass term required to accelerate the particles. Additionally, particles are affected by gravity and sink in the fluid. The sedimentation velocity, u_{ps}, is expressed by Equation (2.14), where g is the acceleration due to gravity.

$$u_{ps} = \frac{1}{18}\left(\frac{\rho_p}{\rho_f} - 1\right)\frac{gd^2}{v}\left(1 + \frac{2al}{d}\right) \quad (2.14)$$

An approximation to a continuous gas jet was applied to a diesel spray in the early phases of air entrainment in the fuel. The momentum hypothesis of a diesel spray was proposed by Wakuri et al. [69]. According to the theory, a spray is a combination jet of ambient gas and diesel fuel that occurs immediately after high-pressure fuel injection into a high-density medium. Hiroyasu et al. [70] effectively created different spray properties based on their experimental work. Several in-situ measuring techniques have been developed recently to capture the inner spray structure. Xia et al. [71] investigated spray injection and atomization in marine diesel under various situations. Kannaiyan et al. [72] investigated the impact of nanoparticles on spray behavior under air conditions. Yu et al. [73] examined the atomization of diesel spray and combustion parameters at 350 MPa injection pressure using a constant-volume chamber containing a mixture of hydrogen and air. It is obvious that air entrainment into a spray body has a significant impact on spray quality. However, the instantaneous entrainment flux has received little attention because of the difficulties in identifying the spray boundary as well as the velocity fields around the spray at the same time. The air entrainment process into a diesel spray and the gas jet was thoroughly explored in this chapter by observing the development process of a single diesel spray/gas jet in a Constant Volume Chamber (CVC). The RCEM was employed as a CVC by holding the piston at a sufficient volume clearance to be charged by the desired ambient.

2.4.The Rapid Compression-Expansion Machine description

The RCEM layout visualized in Figure 2.4 has specifications quite close to those of a real marine diesel engine (see Table 2.1). The RCEM is accelerated to 350 rpm by a 75 kW electric motor. An inverter (Model FRENIC 5000P11) adjusts the speed of the electric motor, and a clutch connects the motor to the RCEM. The RCEM is coupled to a preheating and pressurizing heat tank, which establishes the composition (temperature and pressure) within the cylinder. A Kistler piezoelectric pressure sensor Model 6061B is used to measure the pressure within the cylinder. Tank air is supplied to the in-cylinder at the set pressure and temperature, typically within ± 0.1bar ± 5^{o}C. With this layout, we can reduce the stroke to 260 mm. As can be seen in Figure 2.4, the RCEM contains two injectors, one of which is utilized for the gas jet and the other for the GO pilot fuel. Electronic fuel injection (EFI) allows for precise regulation of injection parameters such as mean working pressure and pulse width in both injectors. As can be seen in Figure 2.5(a), the working GO circulates between the working GO pump, the working GO tank, the accumulator, and the bottom section of the EFI while being pressured by the working GO pump. Once injection begins, the electronic valve is adjusted to cut off the flow of fuel, forcing the working oil to drive the compression piston. The gas injector, shown in Figure 2.5(b), uses a similar injection approach, with its operation predicated on releasing the pressurized gas to flow inside the cylinder via the EFI.

Diesel engines often include fuel injectors mounted in the cylinder head(s), with the nozzle spraying fuel at an angle into the combustion chamber through an umbrella-shaped spray pattern. This common shape has the potential to reduce the diesel spray area to less than half the bore size. Instead, the gas and diesel injectors in this machine are positioned out to the side of the combustion chamber to maximize the fuel's possible travel time. To obtain a maximum distance of 200 mm, a current process has been implemented, tilting the diesel pilot injector by 15 degrees from the horizontal. In order for the visualizing system to record the in-cylinder combustion process, two quartz windows have been installed on both sides of the RCEM. The spray of various injected fuels may be measured with this RCEM because it was designed to function as a Constant Volume Chamber (CVC). By keeping the piston at its top dead center, the RCEM may be turned into a CVC, which has enough volume to be charged by the desired ambient.

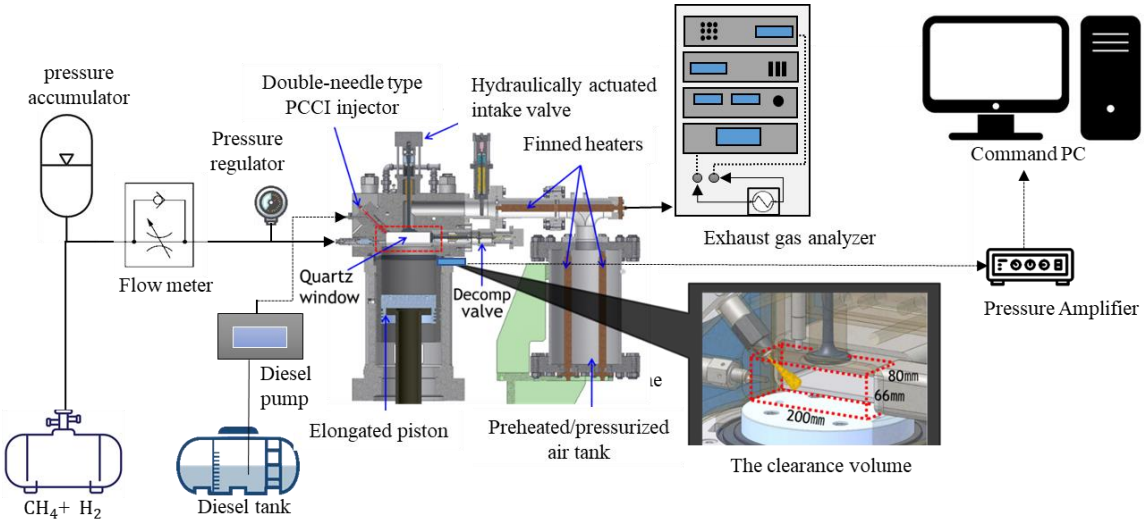

Figure 2.4 Experimental test rig layout.

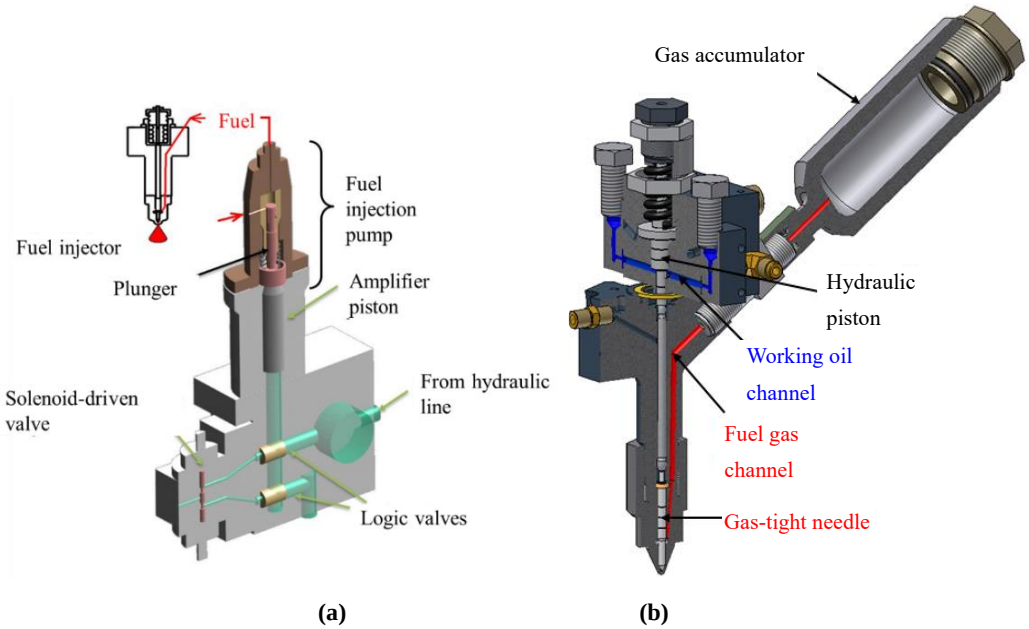

Figure 2.5 The injectors details a) diesel injector, b) gas injector

2.5.Optical technique specifications

Thanks to the two see-through windows, the visualization system can track the movement of the flame within the cylinder. Two high-speed cameras (PHANTOM v1610 and FASTCAM SA-Z) plus a laser source make up the vast majority of the visualizing system (Lee Laser, LC880). The basic configuration of the optics is shown in) Figure 2.6. In order to create parallel light beams that travel into the combustion chamber, the laser beam must first pass through a concave mirror. This necessitated a separation of 3 meters between the laser and the first concave mirror. The high-speed camera model PHANTOM v1610, with specifications indicated in Table 3.1, was set up with a half

mirror between the first concave mirror and the combustion chamber to receive directly reflected beams from the in-cylinder continuing combustion. Meanwhile, the in-cylinder beams are able to instantly identify the shadows cast by the in-cylinder combustion. The light is then focused by the second concave mirror onto the lenses of the second high-speed camera, a FASTCAM SA-Z, with the characteristics listed in Table 3.1. This technique provides a synchronized direct photographs and shadowgraphs.

Table 2.1 Specifications of the RCEM.

Parameter	Specifications
Stroke and bore	260 mm and 240 mm
Clearance volume	200 mm × 66 mm × 80 mm
Compression ratio	10
Engine speed	350 rpm
Quartz window	200 mm ×50 mm ×100 mm

Table 2.2 Specifications of the applied high-speed cameras.

Camera	PHANTOM v1610	FASTCAM SA-Z
Sensor	CMOS image sensor	CMOS image sensor
Resolution	Max 1024×768 pixels at 20000 fps, 36 bits color	Max 1024×1024 pixels at 20,000 fps, 36 bits color
Frame rate	Max 100,000 fps	Max 2,100,000 fps

2.6.Control and measurement system

An AD5435 High-Speed Measurement and System Controller instantaneously controls experiment activation and data extraction. Meanwhile, various PCs were used to link and manage the high-speed cameras (PCs). When the command PC operator activates the driving motor, the signal is transmitted through the HSMS, enabling the motor to run while rotary crank angle encoder records crank angle pulses at intervals of 0.1 degrees. The valves and high-speed cameras, among other devices, are then commanded into action by HSMS. Except for the flame pictures from the high-speed cameras, all measured data is gathered and saved on the command PC. Crank pulses from the crank angle encoder perfectly synchronize the flame pictures with the other measured data (i.e. in-cylinder and pilot injection pressure data, valve lift data of the pilot injection valve, and gas injection valve). In addition, when RCEM is used as a constant-volume combustion chamber, the time between shadowgraph captures is determined by the camera's frame rate, while the HSMS determines when to begin taking pictures.

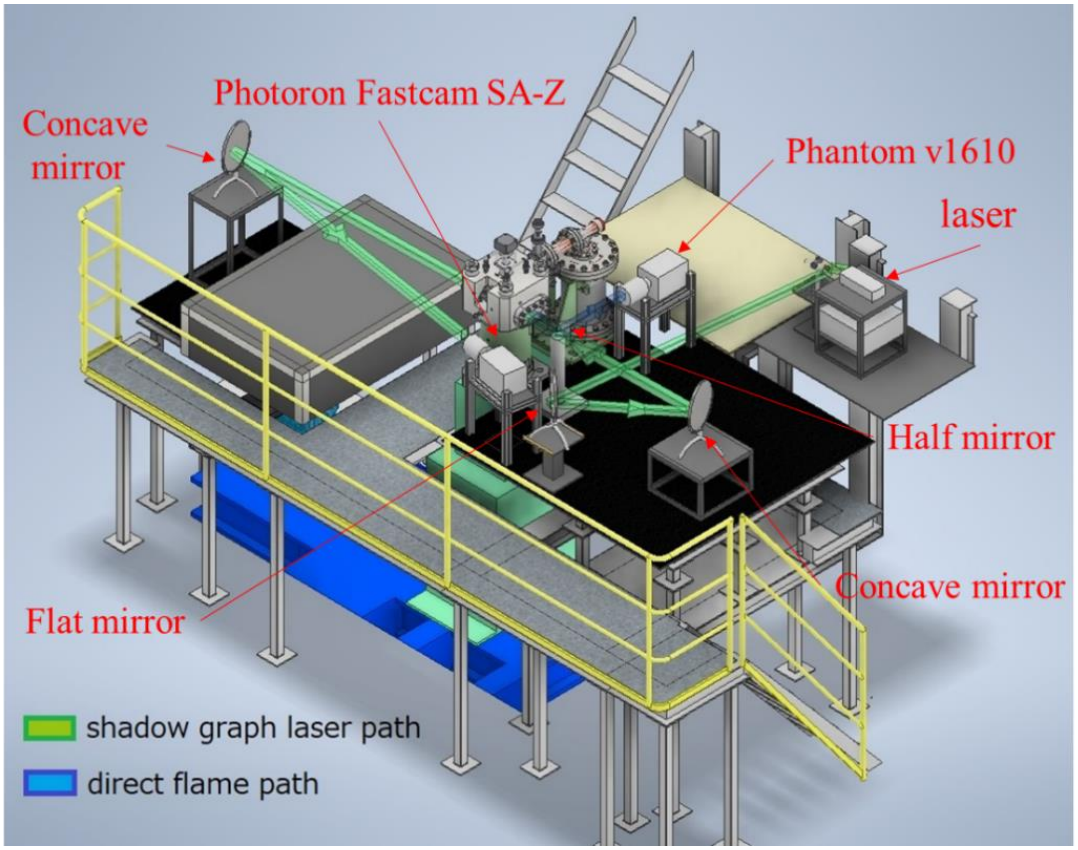

Figure 2.6 The optical system configuration.

2.7.Fluorescence PIV measurements application strategy

The key parameters of the implemented PIV system are shown in

Table 2.3. Only when the ambient temperature is high, the air replaced by nitrogen gas. This is a schematic diagram of the experimental setup and optical system. To measure the amount of air entrainment using Fluorescence PIV, it is necessary to measure the spray contour, therefore, it is necessary to measure the contour of the spray on the opposite side of the PIV camera. Another high-speed camera was installed to measure the spray. The laser beam passes through a rod lens and forms a sheet, and by illuminating the inside of the cylinder, it is possible to capture a two-dimensional flow field. Figure 2.8 illustrates a SCF560 filter fitted to the camera lens to exclude the laser light with a 532 nm wavelength while allowing the light discarded from the fluorescent with a 590 nm wavelength to pass through.

Table 2.3 Specifications and configurations of PIV system

High-speed camera for PIV	High frequency light source for PIV

Type	SA-Z Monochrome (Photoron)	Nd:YAG pulse laser	LDP-100MQG (Lee Laser)
Frame rate	20,000 fps	Wavelength	532 nm
Resolution	1,024 ×512 pixels	Pulse width	200 ns
Exposure time	23.39 μs	Pulse energy	2.0 mJ/pulse
Lenses	Micro NIKKOR 105 mm, F2.8 +2.0-power teleconverter	Frequency	20 kHz (Δt = 50 μs) for spray 40 kHz (Δt = 25 μs) for gas jet
		Timing controller	LC880 (Labsmith)
Suspending tracers in CVC		PIV analysis system	
Type	Godd Ball, B-5C (Suzuki Yushi Industrial Co., Ltd)	PIV software	Koncert II (Seika Corporation)
Material	Spherical hollow SiO_2 particle	Algorithm	Reflexive cross-correlation method
Mean diameter	2.0~2.5 μm	Window size	16 × 16 pixels
Bulk density	180~450 kg/m^3	Overlap	50%

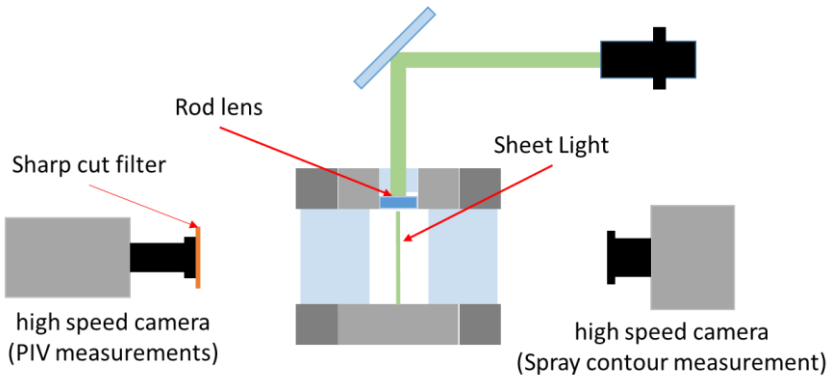

Figure 2.7 **Fluorescence PIV measurements arrangement**

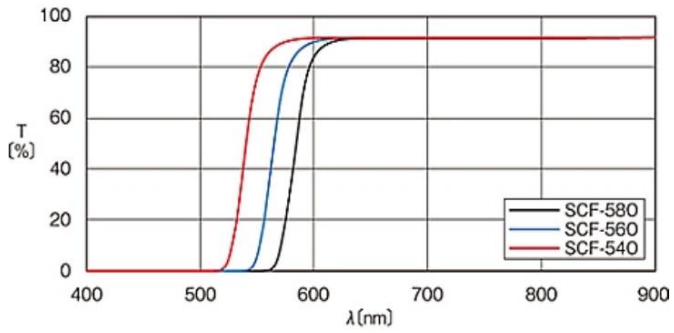

Figure 2.8 **Frequency characteristics of sharp cut filter transmittance versus wavelength.**

2.8.Air entrainment calculation method

When injecting a diesel or methane with a high pressure at an ambient, the ambient starts to entrain the body of the injected fluid. This entrainment has been classified into three zones based on the spray/jet body. The classification of the ambient flow around the spray divided into the following three categories. a) Entrainment Section: where a quasi-stationary spray develops from the nozzle outlet according to the spray angle, and the surrounding fluid flows into the spray due to the pressure difference between the inside of the spray and the surrounding fluid. b) Recirculation Section: In this region, there is no influx of surrounding fluid into the spray because it moves with the spray droplets. c) Capturing section: in which the surrounding fluid is pushed out at the tip of the spray, but because the tip of the spray reaches at a speed faster than the speed of the surrounding fluid, the spray develops while swallowing the surrounding fluid.

In this study, we applied the above concept to the gas jet and calculated the amount of air introduced in the gas jet. Figure 2.9 shows the outline of the jet in the calculation of the amount of air introduced and the concept of the velocity vector at the analysis points on the outline. Assuming that the jet is axially symmetrical with respect to the injection direction, the outline of the jet obtained from the image is divided into N truncated cones that reflect the contour shape divided by the measurement unit length Δx [mm]. Then, the surface area S_i, the atmosphere introduction velocity v_{ent_i} at the representative point on the surface, and the atmosphere introduction rate $\dot{M}_a$ are obtained for the i-th truncated cone from the injection hole. Assuming that v_{ent_i} is constant on the surface of the truncated cone, the flow velocity vector obtained from PIV is obtained for four points around the representative point, and the weighted average of the reciprocal of the distance is calculated, Equation (2.15) determines v_{ent_i}. The volumetric air introduction amount to the truncated cone i at the elapsed time t ASOE (After Start Of Ejection) is the product of S_i and v_{ent_i}, which gives t[ms ASOE] The air introduction rate $\dot{M}_a$ at is expressed by Equation (2.17). Where, Air entrainment velocity [m/s], Side area of truncated cone i [m^2], and Air entrainment rate to jet [kg/s].

$$v_{ent_i} = v_{ix} sin\theta_i + v_{iy} \cos\theta_i \tag{2.15}$$

$$S_i = 2\pi y_i \Delta x cos\theta_i \tag{2.16}$$

$$\dot{M}_a = \rho_a \sum_{i=1}^{N} S_i v_{ent_i} \tag{2.17}$$

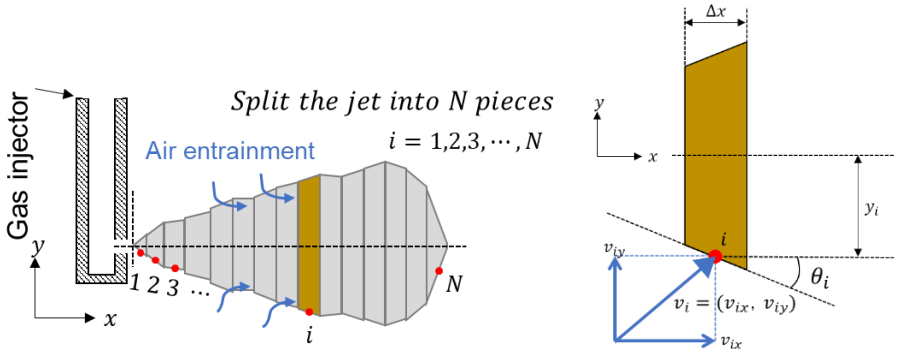

Figure 2.9 Air entrainment calculation method

Chapter 3

Air entrainment in diesel spray and methane jet

3.1.methodology

This chapter contains a discussion for the results obtained from the PIV measurements for both diesel spray and methane jet. In case of diesel spray, fluorescence PIV was applied to overcome the scattered light on the diesel body that illuminates the PIV measurements.

3.2.PIV measurements for the methane jet

With the use of PIV and a high repetition pulse laser, we were able to see and quantify the air flow during its introduction into the high-pressure Methane jet. Several pressure and temperature regimes were tried out on methane gas. In the instance of methane gas, we employed a 0.4-hole injector with an injection pressure of 20, 30, and 40 MPa at 293 K. The jet's PIV data are displayed in Figure 3.1. Exclusion flow propagates radially from the jet's tip in the jet's Capturing Section, whereas in the jet's Entrainment Section, flow persists from the jet's base and faces inward. The flow field around the jet was also found to be larger than expected, with velocities of roughly 1.0 to 2.0 [m/s]. Atmospheric velocity introduction dispersion at the spray boundary as seen from the direction of the injection axis is seen in Figure 3.2. PIV data shows that the jet actively generates vortices and experiences significant air entrainment.

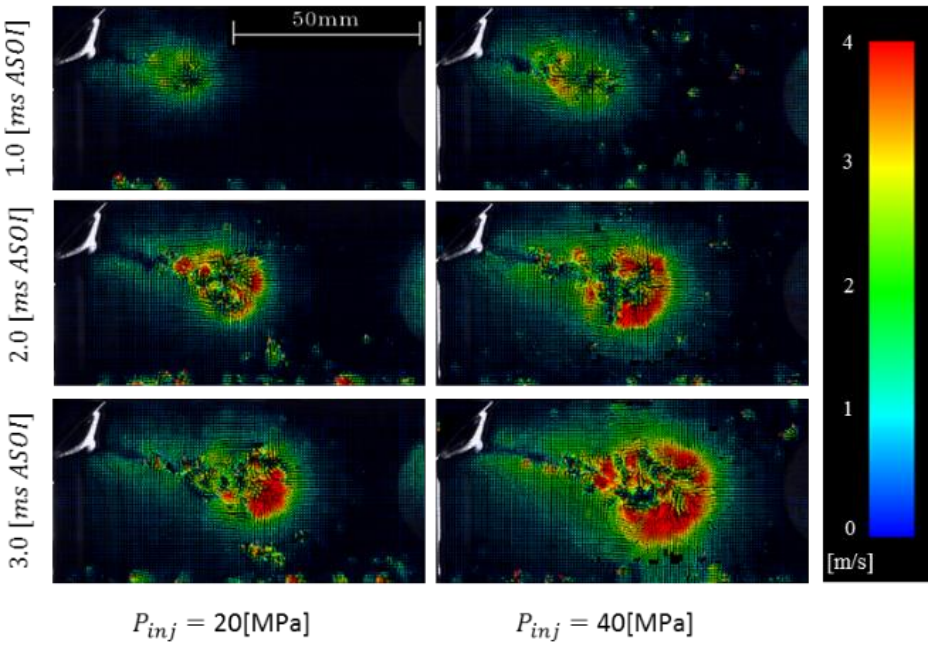

Figure 3.1 Flow field around Methane jet at 36.3 kg/m^3 ambient density

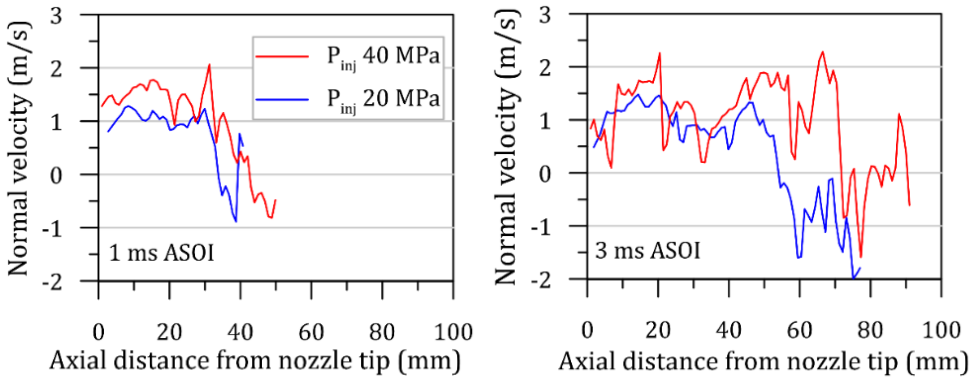

Figure 3.2 Distribution of accompanying flow flowing into the spray ρa = 36.3 [kg /m^3]

The rate of mass introduction into the atmosphere and the total mass introduced over time are visualized in Figure 3.3. The total mass of the ambient atmosphere supplied was shown to rise with increasing injection pressure for both spraying and jetting, as seen in the graph below. Total air entrainment and air entrainment rate vs. time at an ambient pressure of 36.3 kg/m^3 However, the ratio of spray to jet is indicated to be roughly the same, therefore this measurement is accurate even when only the introduction from the Entrainment Section is examined. Furthermore, it appears that the entrainment of a huge atmosphere owing to the large-scale vortex structure, as illustrated in Figure 3.4, is one of the causes for the significant introduction of jets from the Entrainment Section.

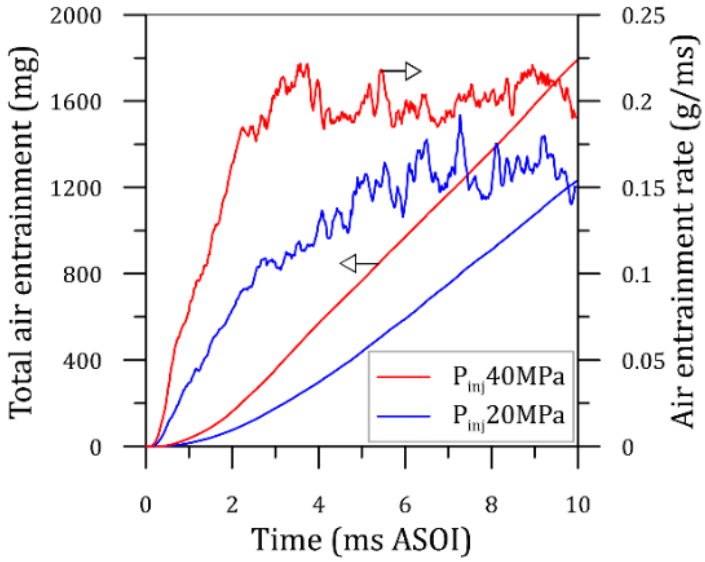

Figure 3.3 Air entrainment for methane jet under different injection pressures

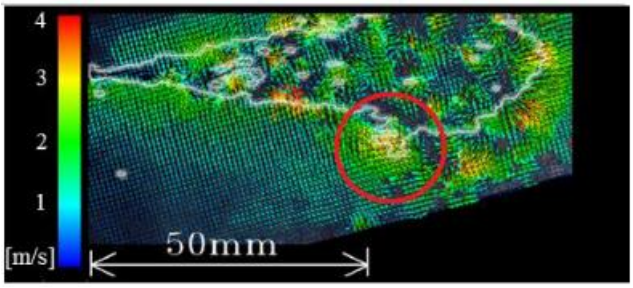

Figure 3.4 Distribution of the accompanying flow flowing into the spray and the moment of introduction of the atmosphere by the vortex seen in the jet P_{inj}=40[MPa], density= 36.3[kg/m^3]

3.3.PIV measurements for diesel spray

The effects of injection pressure, ambient density, and temperature on the air entrainment characteristics of light oil were analyzed using the contour generated from the photo for the spray. Table 3.1 describes the experimental conditions of CVC's fuel injection and inner ambient. The ambient temperature was set to near non-evaporation level (301 K) and active evaporation level (823 K) thanks to CVC's high flexibility in setting ambient temperature and pressure separately, with the ambient density, one of the most important indexes for spray atomization, fixed at three levels by adjusting the ambient pressure one by one. Table 3.2 depicts the experimental settings employed in this investigation and specifies the tracer particles. Total air entrainment was calculated using spray surface area estimates at two distinct injection pressures of 60 and 70 MPa. Entrainment seems to accrue after 1ms After Start Of Injection (ASOI) in the case of high injection pressure, but it exhibits more steady values in the case of 60 MPa.

Table 3.1 Experimental conditions

Fuel injection			Atmospheric conditions			
Fuel	Hole dia. d_{inj} [mm]	Pressure P_{inj} [MPa]	Gas	Temp. T_a [K]	Pressure P_a [MPa]	Density ρ_a [kg/m^3]
Gas oil JIS#2 Liquid	0.16	60	Air	301	1.66	19.3
		70			0.91	10.5
		80			0.1	1.20
		60	N_2	823	4.5	19.3
		70			2.5	10.5
		80			0.18	1.20

Table 3.2 Experimental conditions

Fuel	Light oil JIS#2
Nozzle diameter	0.125 mm
Nozzles number	6 and 8

Injection pressure	60 and 70 MPa
Injection time	500 μs
Ambient gas	Nitrogen
Ambient pressure	1.56 MPa
Ambient Temperature	296 K

Spray observation at low and high ambient density and evaporation rates are shown in Figure 3.5. Since the sheet light that lights the area around the nozzle comes from the top left, the spray image is also unbalanced. The droplet density at the spray tip and the dispersed light intensity at the spray tip both decrease under evaporation conditions, yet the range may still be determined accurately. The spray's spread angle is also shown to decrease close to the injection hole and increase toward the spray's tip. Air entrainment into a spray or jet can be difficult to calculate due to the jet body's brightness, which prevents detection of particle velocity in the detached region surrounding the spray or jet body. Tracer particles were released into the air and used to measure the spray's velocity using fluorescence PIV.

Spray penetration at different injection pressures, ambient densities, and ambient temperatures are displayed in Figure 3.6. At 301K, as shown in Figure 3.6(a), the density of the diesel spray has a negative effect on its penetration into the air due to the drag force of the surrounding environment. At (1.2), (10.5), and (19.3) kg/m^3 ambient density, the spray penetration length reached 165 mm at (1, 6, and 9)ms after start of injection (ASOI). Figure 3.6(a) shows that in the event of a high ambient temperature, the spray penetration achieved a length of 165 mm at (1, 9 and 11)ms ASOI and densities of (1.2), (10.5), and (19.3) kg/m^3. Due to an increase in evaporation at the spray's tip, an increase in ambient temperature reduced its ability to penetrate. It is clear that, with the exception of the low air density condition, the spray reach distance has a well-established time-dependent tendency that is first proportional to around 0.3ms ASOI and thereafter proportional to the square root.

Figure 3.7 shows that the spray angle is exactly proportional to the ambient density. Spray penetration reduces as ambient density increases. This might be because the air-fuel mixture, which contains fuel droplets, exchanges momentum with the surrounding fluid in a high-density air in a quasi-steady condition with a consistent injection rate. Furthermore, at the same injection condition, the higher the ambient

temperature the wider the cone angle. The velocity vector distribution of the ambient air determined by PIV is shown in Figure 3.8. The PIV analysis was only conducted on the left side of the well-lit spray during the spray measurement. There are exclusion flows that extend radially around the tip of the spray, and when they wrap around, an accompanying flow that flows into the spray is produced on the spray's side surface. Under the identical parameters of density and injection pressure, the spray in the evaporation condition is slightly smaller and stronger exclusion flow generated. This shows that the fuel vapor is maintained in the spray during the evaporation condition, thus the momentum exchange between the spray tip and the extruded ambient air is more positive, and the state shifts to a state similar to a steady gas jet.

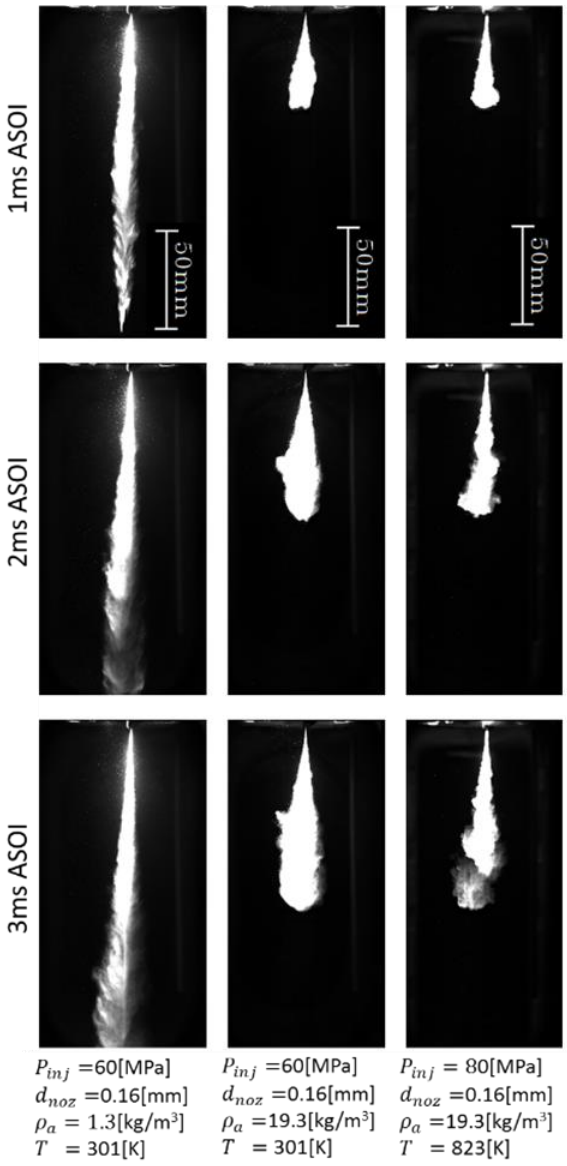

Figure 3.5 Spray growth with time ASOI (After Start of Injection)

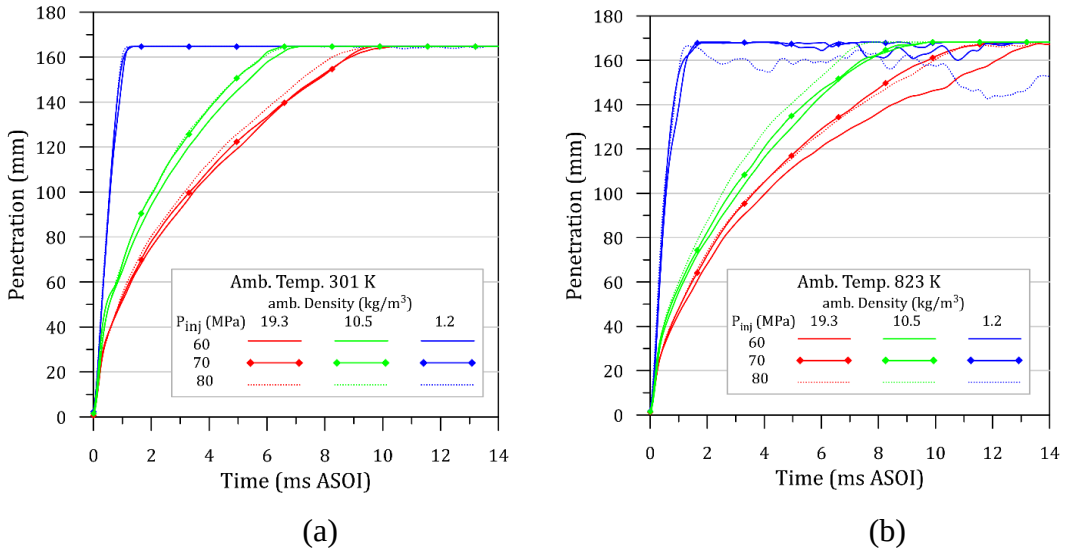

Figure 3.6 **Diesel spray and methane jet penetration versus time.**

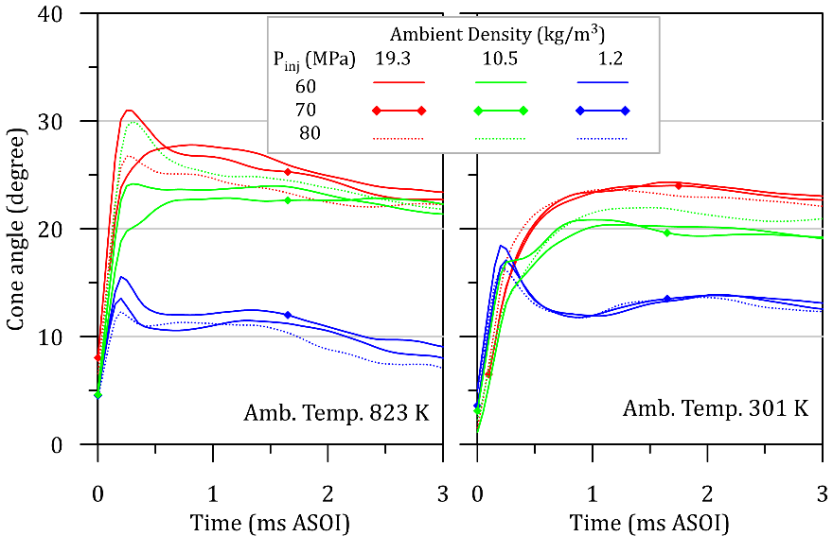

Figure 3.7 **Spray cone angle versus elapsed time ASOI**

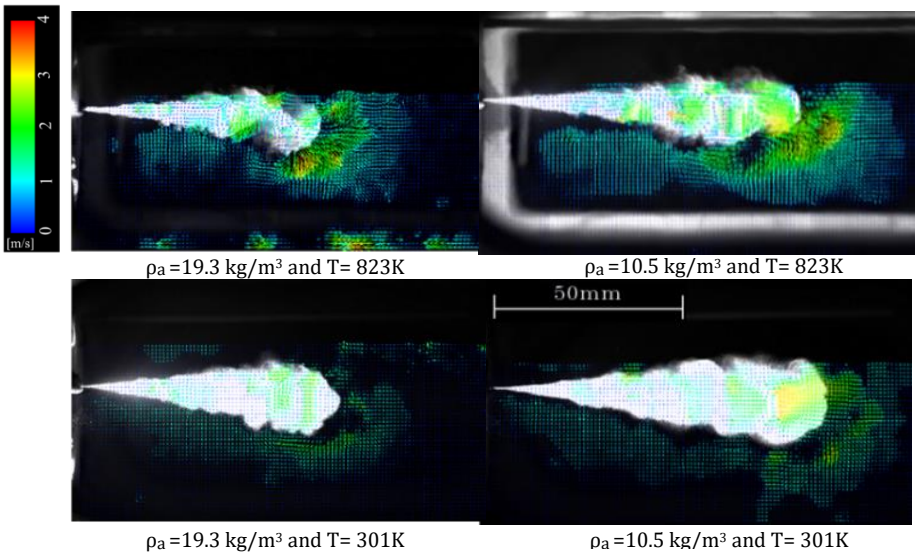

Figure 3.8 **Flow field of surrounding air at 2.5ms ASOI at 80 MPa injection pressure**

According to Figure 3.9, as the spray expands, the introduced mass flux in both the Capturing Section (CS) and the Entrainment Section (ES) grows proportionally to the time after injection. The injected mass flow at the CS, on the other hand, is 3 to 4 times that of the ES. Under evaporation circumstances, the diameter of the ES reduces and the surface area reduces, so the introduced mass drops, however at the CS, the maximum value of the introduced flux surpasses the non-evaporation condition as the spray develops and the evaporation progresses. Figure 3.10 depicts the spray surface area vs time under various situations. The surface area has been seen to grow dramatically at extremely low density because of the high relative speed between the spray and the ambient. Then, when the ambient density increased, the contact surface area decreased due to the less turbulent spray surface.

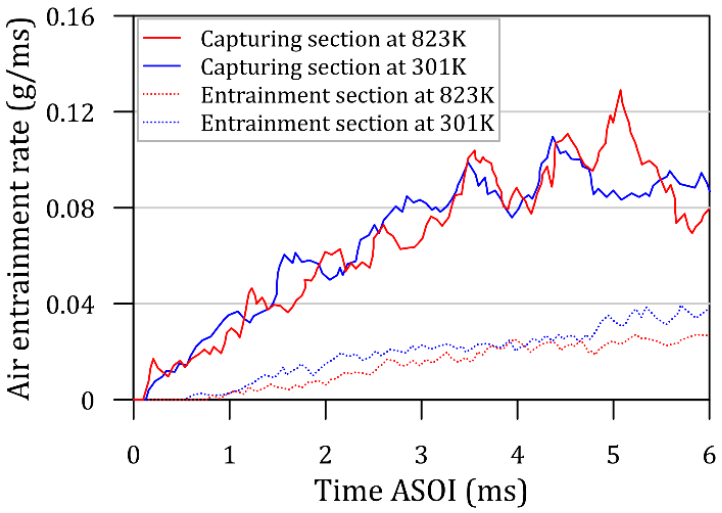

Figure 3.9 Sectional air entrainment rate

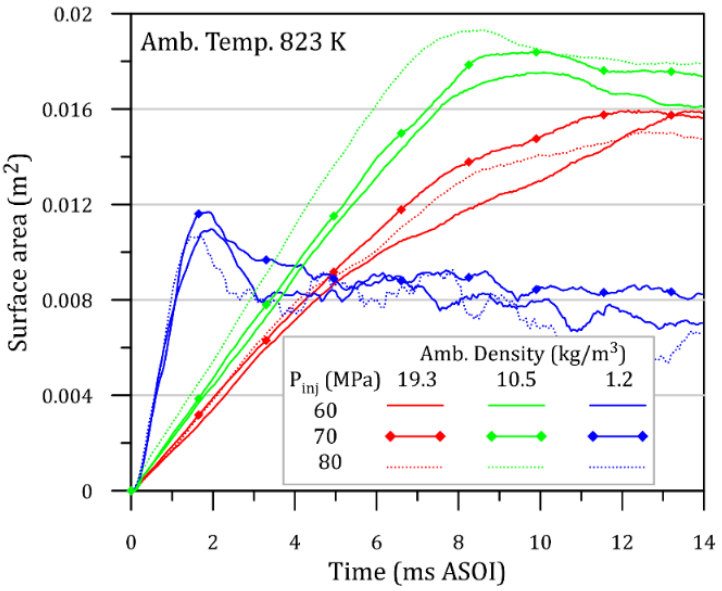

Figure 3.10 spray surface area over time

Figure 3.11 depicts the rate of air entrainment vs time and total injected mass versus time under various injection pressure and ambient conditions. Because the spray extends fast, increasing the surface area, there is no substantial influence of injection pressure or ambient density on the air entrainment rate, as shown in Figure 3.11(a). When seen in Figure 3.11(b), the total quantity of ambient air supplied increased slightly as the injection pressure increased at the same ambient density. In general, raising the injection pressure to accelerate evaporation, increasing the atmospheric temperature, and increasing the atmospheric density reduce the introduced mass in ES while increasing the maximum value in CS. It was determined that the impact of injection circumstances and atmospheric conditions on atmosphere introduction is minimal.

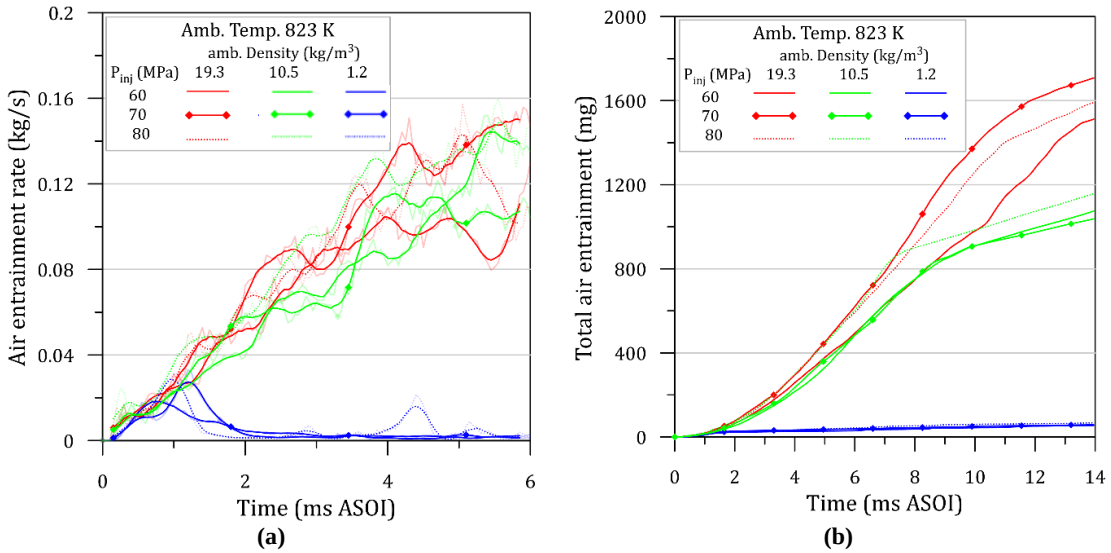

Figure 3.11 air entrainment rate and total air entrainment respect to time

Identical circumstances of the experiment were replicated in the spray simulation using the CFD programme CONVERGE. Discrete Droplet Model (DDM) for spray; KH-RT model for break-up; NTC collision model for collisions; Frossling model for evaporation; and RNG k- model for turbulence. Mesh size within the truncated cone with a diameter of 10 mm at the injector and a spread angle of 24 degrees is evenly minimized at 0.5 mm, the outside diameter is 100 mm, and the height is 200 mm. The injection hole is located 4 mm below the upper surface of the cylinder. There was a one-millimeter gap between the interior of the cylinder and the mesh. Also, the marker gas is injected at the position h = 10 and 70 mm from the upper end of the container on the central axis of the container, and then air flow is tracked by changing in the concentration distribution of marker gas with spray development. The spray reach range is 97% of the fuel mass. The

spray boundary is determined by setting the fuel volume fraction in the cell to 0.01% or more as the threshold value.

Figure 3.12(a) depicts the time-varying velocity field surrounding the spray as the spray develops, and Figure 3.12(b) depicts the spray contour using the definition and the vector display that simply represents the flow direction of the atmosphere. There is a significant flow just after the injection hole opens and at the injection hole's tip during the first stage of injection. It is also highlighted that the flow velocity from the downstream end of the catching part to the upstream entrainment section is counterclockwise to the spray. The relative velocity, which indicates air entry from the spray tip, is confirmed by the fact that the anticipated flow velocity surrounding the spray is almost twice as high as the PIV measurement result but less than 1/10 of the spray progress rate.

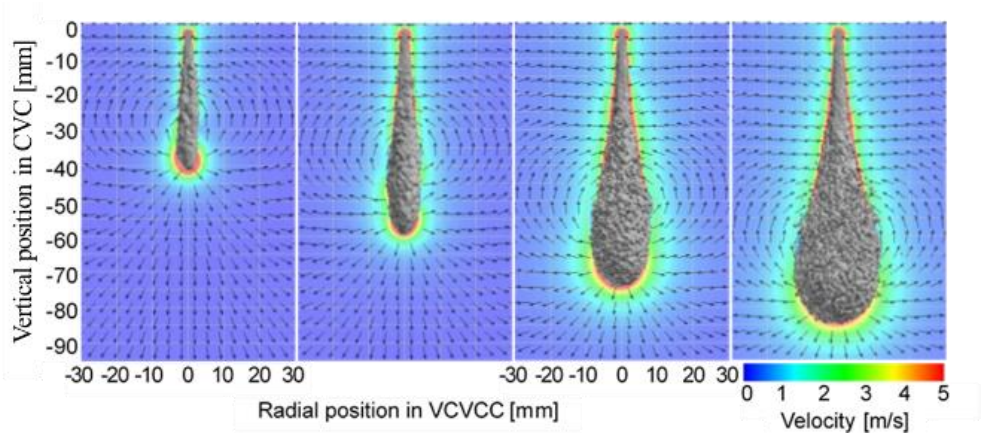

(a)

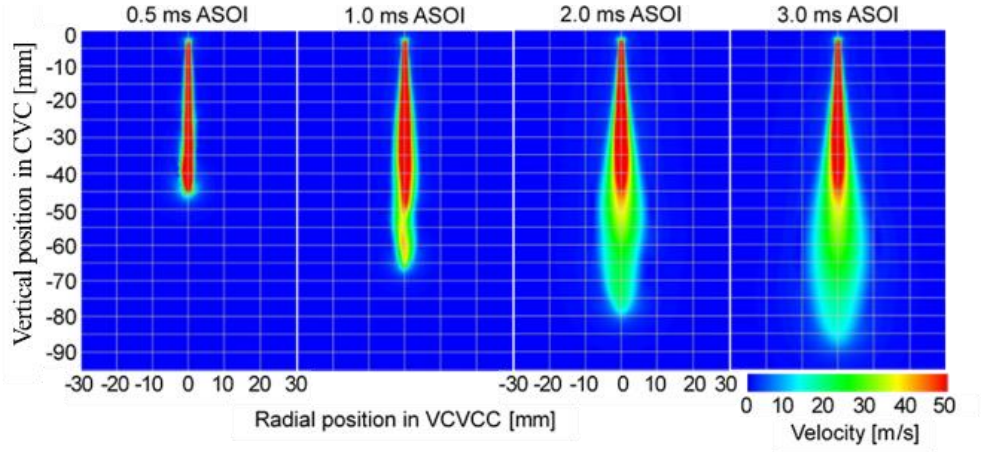

(b)

Figure 3.12 Flow velocity distribution in the spray over time (P_{inj} = 60 MPa).

Figure 3.13 shows the process of introducing the marker gas into the spray when the injection position h = -10 mm, with the mass fraction of the marker gas superimposed on the spray contour. The spray reaches the injection position just before 0.2ms ASOI,

then proceeds through the marker gas, and is introduced along the spray core until 0.5ms ASOI exceeding the split distance (40 to 45 mm) and reaches the spray tip. In this way, the atmosphere existing in front of the spray at the initial stage of spraying is introduced linearly into the spray along the accompanying flow on the spray surface. It is known that the droplets at the tip of the spray with remarkable deceleration are updated by the subsequent spray droplets with higher speed, but even in this calculation example, the marker gas starts from around the spray center axis after 2.0ms ASOI. It has moved to the outer ring of the spray tip. Figure 3.13(b) shows the introduction process when the injection position h = -70 mm. The arrival time of the spray at the injection position is delayed to 1.6ms ASOI, and the marker gas is deformed before it arrives due to the exclusion flow before the spray. The developed spray cannot penetrate the marker gas and proceeds in a state where the marker gas is deformed into a horseshoe shape and attached to the front part of the spray. However, at 2.0ms ASOI, some of the deformed marker gas penetrates the spray, and at 3.0ms ASOI, the whole is present in the spray. These processes are like the introduction of atmosphere in CS, but the measurement results show that the introduction of atmosphere in CS is observed from the initial stage of injection, and further study is required.

When the injection position h = -10 mm, the mass fraction of the marker gas is overlaid on the spray contour, as shown in Figure 3.13. Before 0.2ms ASOI, the spray reaches the injection spot, travels through the marker gas, and is injected along the spray core until 0.5ms ASOI, at which point it has already surpassed the split distance (40 to 45 mm) and has arrived at the spray tip. The atmosphere in front of the spray at the beginning of the spraying process is injected into the spray in a linear fashion along the flow accompanying the spray surface. Although it is well-established that faster-moving spray droplets eventually catch up to the slower-moving droplets at the spray's tip, in this calculation example, the marker gas does not begin to move until after 2.0ms after the first appearance of the spray (ASOI). It's now located on the spray tip's outer ring. The initialization procedure at an injection point of h = -70 mm is depicted in Figure 3.13(b). Due to the exclusion flow in front of the spray, the spray's arrival time is delayed to 1.6ms ASOI, and the marking gas is distorted before it reaches. Because the generated spray is too narrow, the marking gas is distorted into a horseshoe shape and attaches to the spray's leading edge as it moves forward. At 2.0ms ASOI, however, part of the distorted marker gas makes its way into the spray, and by 3.0ms ASOI, the whole cloud is present in the spray. These mechanisms are similar to the atmospheric introduction in CS, however the

measurement findings reveal that the atmospheric introduction in CS is detected from the earliest stage of injection.

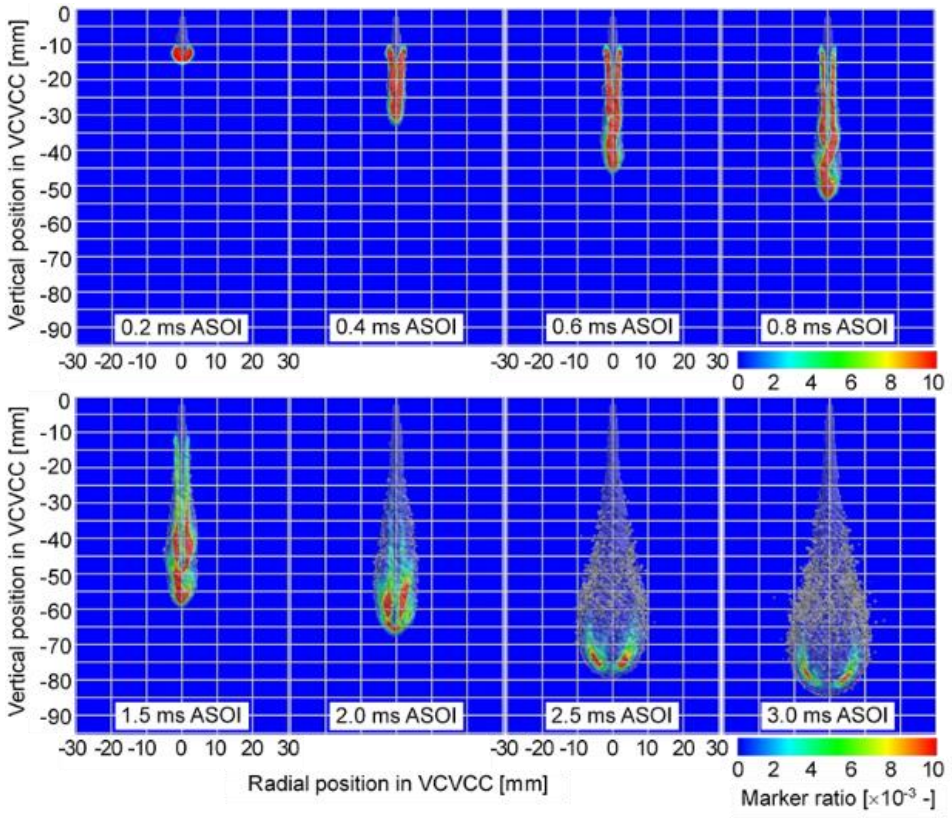

(a)

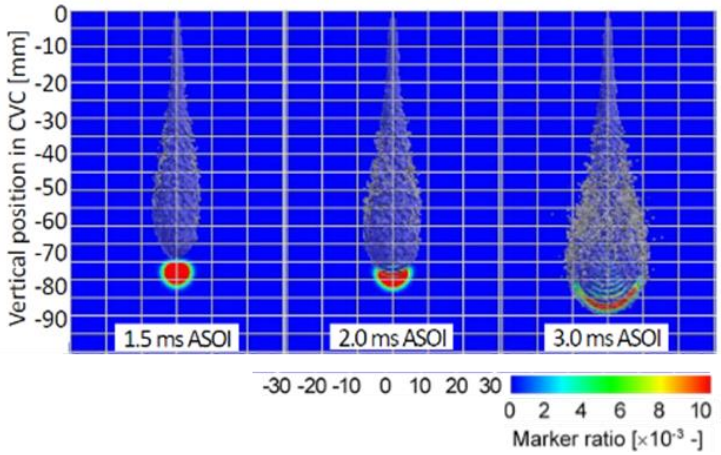

(b)

Figure 3.13 Mass fraction distribution of marker gas around a spray (a) marker gas position h = -10 mm (b) marker gas position h = -70 mm

3.3.1.Fluorescence PIV

Simultaneous measurements of an inflow field surrounding the spray by dynamic PIV with a high-repetition pulse laser and of the spray contour information from the Mie scattering light of the spray droplets allowed for the determination of the instantaneous entrainment mass into the spray body. Mie scattering is an elastic scattering of light that

happens when incoming light interacts with particles that are the same size as or bigger than the wavelength of the light. The dispersed light produced by the interaction of the laser light with the fuel spray droplets is known as Mie scattering light. We learned about the spray's composition and density from the scattered light, which in turn revealed the droplets' sizes, velocities, and concentrations. Figure 3.14 represents the contour extracted from the image for the spray was used to indicate the light oil injection process, the effect of the ambient temperature on the air entrainment, and a comparison of the air entrainment characteristics between sprays and jets that reach the same extent at room temperature, all in steady state conditions under different injection pressures.

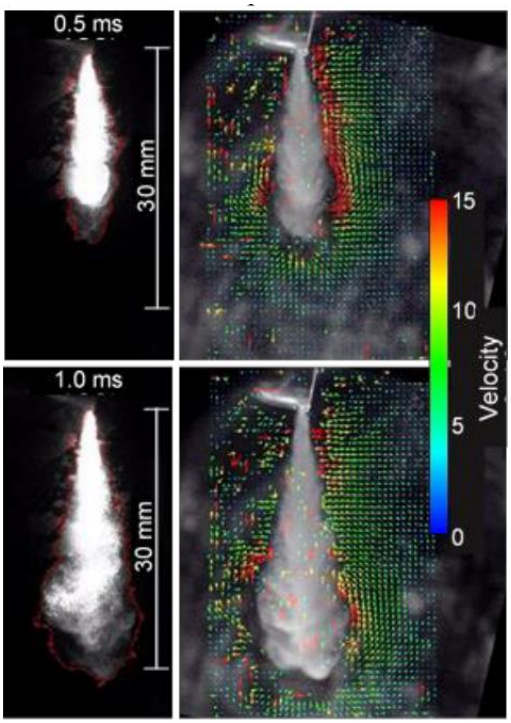

Figure 3.14 Comparison between the method in this study and the conventional method (left is conventional method while right is fluorescence PIV method)

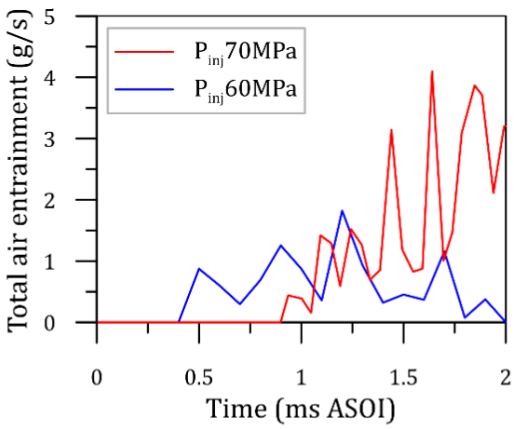

Figure 3.15 Air entrainment rate at 60 MPa and 70 MPa injection pressures

Chapter 4

Exhaust gas Recirculation and Fuel Emulsion in diesel engine

4.1.methodology

This chapter explores, at a constant total heat release, the effects of combining EGR and water-in-fuel emulsion (WFE) approaches. Initially, the EGR and WFE were investigated experimentally, and subsequently the study was expanded to include a wider variety of percentage combinations using the KIVA-3V code. By diluting the intake air with pure nitrogen at a constant injection pressure rating of 150 MPa, three different oxygen concentrations (21%, 18.3%, and 16.3%) were used to conduct the experimental EGR instances.

In this study, an engine layout was used to determine the percentages of inert gas and oxygen present in the engine's incoming, outgoing, and recycled exhaust gases. Intake and exhaust mass balance for a non-EGR supercharged diesel engine at 100 units of air mass flow rate is shown in Figure 4.1. Some assumptions were considered to make this process workable. (1) It is assumed that the mass concentration of oxygen in the air is 20%, with the remaining 80% being inert gas. (2) Fuel weight is not considered. (3) The mass of C and H was disregarded, and the water and carbon dioxide produced were added to the inert gas on the assumption that combustion was complete. (4) Without considering the influence of the load, we assume that the mass oxygen concentration in the product of full combustion is 10%. It is important to note that the oxygen content is denoted in the denominator and the inert gas content is denoted in the numerator. But that doesn't make it a fraction.

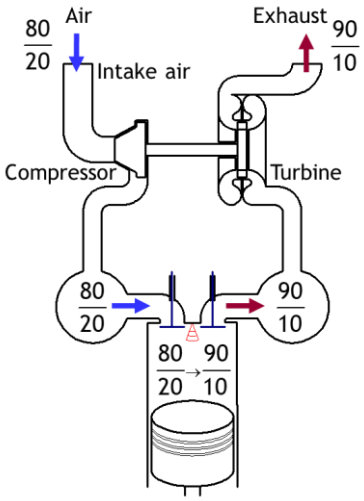

Figure 4.1 The mass balance for a non-EGR supercharged diesel engine

- Constant Air Suction: CAS

When using CAS, the engine intake is not modified in any way compared to the non-EGR situation. Recirculated exhaust gas contains the same proportion of inert gases to oxygen as non-EGR exhaust gas. Increasing the flow coefficient through the engine to. Figure 4.2 shows the CAS mass balance together with two different values of α (1.25, 1.5). The mass balance reveals that to get an oxygen concentration of 18% in the intake air, a value of 1.25 for the increase α coefficient is needed. While calculations suggest that a 50% EGR should be guaranteed to attain an oxygen concentration of 16.7% with equals 1.5.

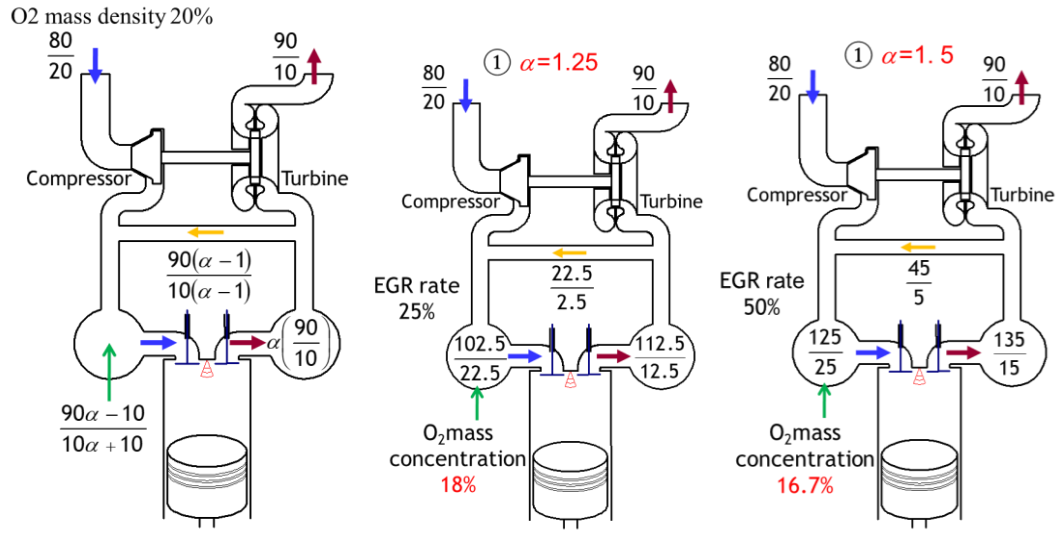

Figure 4.2 mass balance of a diesel engine with EGR in the CAS case

- Constant Oxygen Charge (COC)

When no EGR is present, the intake air volume can be decreased until the mass of oxygen in the supply air is identical to the mass of oxygen in the intake air. Reduce the air intake in the COC by a factor of till it is the same as the intake in the absence of EGR. Simultaneously, Equations (4.1) and (4.2) might be used to determine x and y. Figure 4.3 displays the mass balance for COC using the reduction factors (β) of 0.90 and 0.86 as examples. The figure shows that oxygen concentration of 18% may be achieved by using a reduction factor (β) of 0.9 and recycling 20% of the spent gases. Using a reduction factor of 0.86, which enables a low rate of EGR (from 28% to 16.7% of the oxygen concentration in the in-cylinder content), yielded the most beneficial results.

$$x = \frac{80\beta + 10}{2\beta - 1} \tag{4.1}$$

$$y = \frac{200(8\beta + 1)(1 - \beta)}{(2\beta - 1)} \tag{4.2}$$

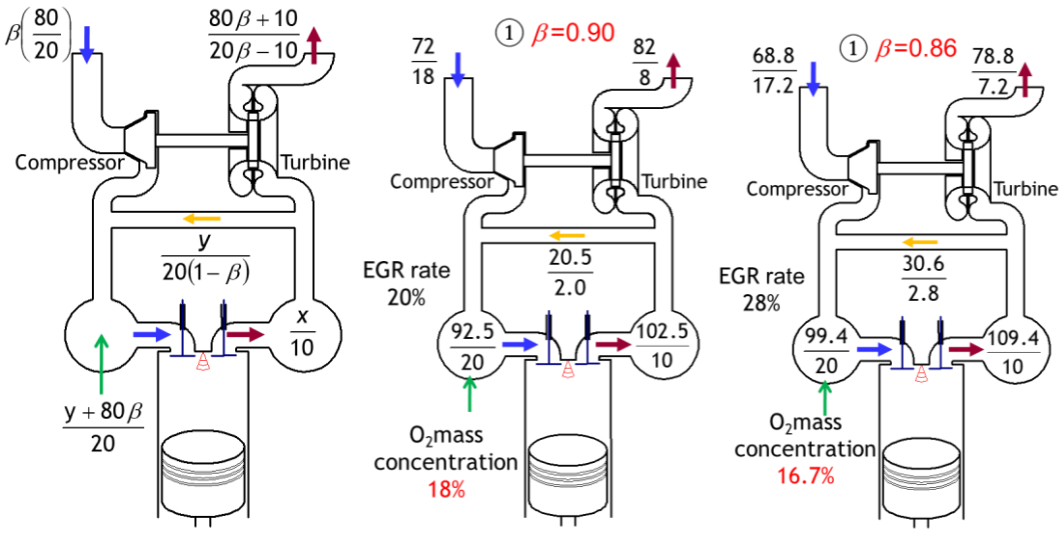

Figure 4.3 mass balance of a diesel engine with EGR in the COC case

A 1D simulation model of a marine diesel engine was developed in the GT-Power environment [62]. GT-power [61] provides a reliable method for calculating indicated thermal efficiency (ITE), brake-specific fuel consumption (BSFC), and a residual gas percentage (RGF). A complete 1D simulation model was built using the lab's RCEM setup. Figure 4.4 presents the 1D GT-Power simulation model used in the test RCEM. GT-power code is used to model the engine, and the simulated and experimental results are compared. The 1D GT-Power model is highly sensitive to changes in geometry, rules, and efficiency. Therefore, the bore, stroke, compression ratio, valve diameter, valve lift, valve timing, turbocharger maps, etc. [63] of the test engine are all factored into the boundary conditions of the 1D simulation model. Boundary factors including shape, regulation, and performance can significantly affect the outcomes of a 1D GT-Power simulation. For this reason, the bore, stroke, compression ratio, and injection time of the test engine were all input into the software from the corresponding construction charts and RCEM sensors. The Shell Global Combustion Model (SGCOM) was used for the analysis; this is a comprehensive, multi-zone model that allows for precise forecasting of combustion analytics, engine performance, and emissions in both spark-ignition (SI) and compression-ignition (CI) engines.

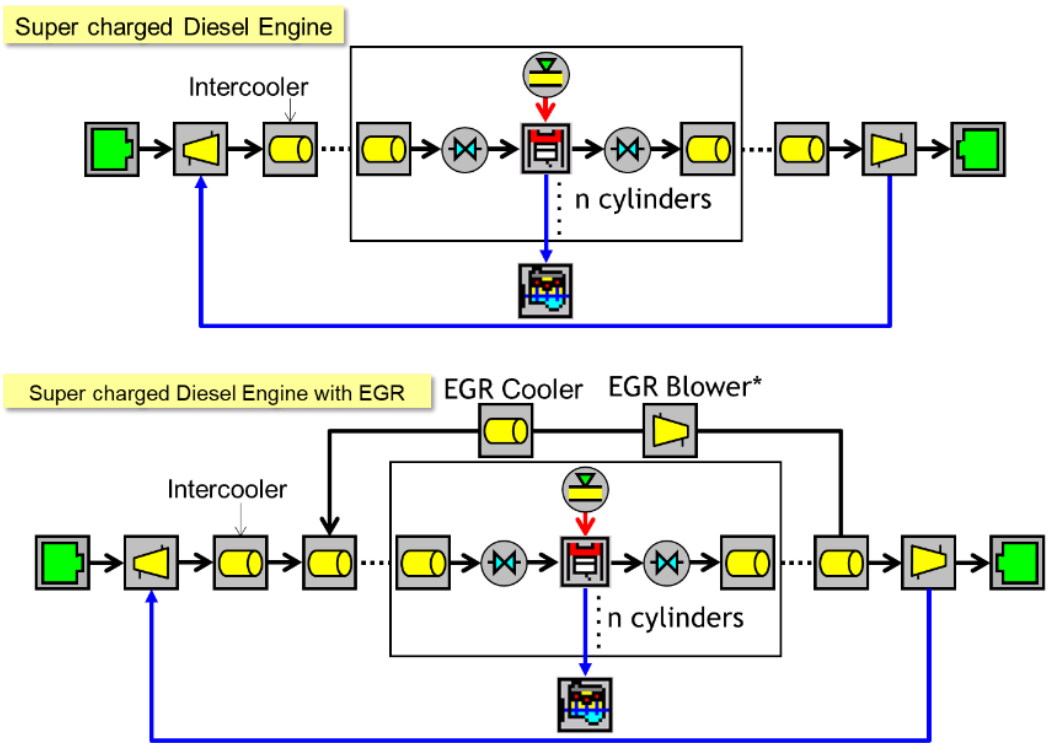

Figure 4.4 Diesel engine model simulated using G.T. Power (with and without EGR)

WFE was used in two different scenarios, each including a different percentage of water (0, 25, and 40 v/v). To stabilize the water dispersion, 0.9% pharmaceutically active agent (Sorbitan monolaurate) is added to the water prior to mixing with the fuel [74]. As can be seen in Figure 4.5, the water-fuel emulsion was accomplished manually by placing the necessary additives in separate tanks and then mixing them together. In addition, the fuel and water were instantly combined using a circular homogenizer before being fed into the RCEM. In the last set of tests for this experimental investigation, four different configurations of EGR and WFE were put to the test. Since the amount of the emulsified fuel is more than the gas oil, the injection duration, injection pressure, or nozzle hole size must be increased when WFE is used. As can be seen in Table 4.1 and Table 4.2, all three scenarios were used in this analysis. In Case 1, the injection was left in for a further 5 minutes, bringing the total to 33.3 or 37.4^{o}CA. Case 2's injection pressure ranges from 80 to 125 MPa, with a maximum of 150 MPa. In Case 3, the nozzle hole diameter is between 0.5 and 0.6 mm. In Case 3, the available injectors only had 0.5- or 0.6-mm nozzle holes.

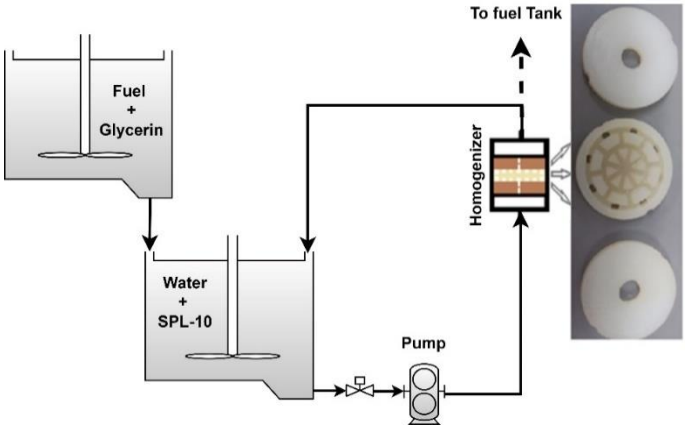

Figure 4.5 The instantaneous emulsion system before injection

Table 4.1 Experimental conditions in EGR.

	Exhaust gas recirculation			
Initial Oxygen concentration [vol%]	21.0	18.3	16.3	
Timing of injection start [deg. ATDC]	-5.2	-5.1	-5.1	
Injection duration [deg.]	20.3	20.7	20.6	
	EGR and WFE combinations			
Initial Oxygen concentration [vol%]	18.3		16.3	
Fuel	WFE25	WFE40	WFE25	WFE40
The ratio of water to fuel [vol%]	25	40	25	40
Timing of injection start [deg. ATDC]	-4.8	-5.2	-4.8	-5.2
Injection duration [deg.]	24.6	29.3	25.1	29.4

Table 4.2 Experimental conditions of WFE.

	Base	Case 1	Case 2			Case 3
Initial Oxygen concentration [vol%]	21.0					
Fuel	Gas oil	WFE25	WFE40	WFE25	WFE40	WFE40
The ratio of water to fuel [vol%]	0	25	40	25	40	40
Timing of injection start [deg. ATDC]	-3.1	-4.4	-4.4	-6.3	-7.0	-3.1
Injection duration [deg.]	25.4	33.3	37.4	28.7	29.6	25.9
Injecting pressure [MPa]	80	80		125	150	80
Diameter of nozzle hole [mm]	0.5					0.6

While optical experiments to enhance experiment analysis have become commonplace, data obtained directly from combustion images is quite sparse. To get over this limitation, several researchers have turned to the two-color technique (TCM) [75,76] for analyzing combustion images. The thermochromic meter (TCM) may be used to analyze combustion images and calculate the flame temperature. By applying TCM processing on photos of combustion, we may get a concentration value at a given location

for the flame's temperature, soot, and NOx emissions [84]. In this research, the soot particles in a diesel flame are used to determine flame temperature by emitting light at two different temperatures. TCM stands for "two-color method" since it compares results from two measurements taken at different wavelengths.

The TCM is used in Figure 4.6(a) by separating the blue and red light from the emitted light. Figure 4.6(b) is an illustration of the high-speed camera Model FASTCAM SA4 being used to take direct images of the in-cylinder combustion, which are then processed using the two-color method. Each collected image was examined according to the colour of every individual pixel. Due consideration was given to the digital RGB values of the real flame photographs, and the exposure situation was changed accordingly while filming. The range of RGB values is 0-255, and extremes may be reached if an unsuitable setting is used. The exposure conditions were set such that the brightest spot in the resulting flame image would provide a value less than 255. It was thought that the soot particles' temperatures were not significantly different from those of the combustion gas. Equations (3.3), a derivation of the Hottel-Broughton equation, is used, where C_2 is second radiation constant in Plank's law, α : constant (1.38 at visible light range), T is the absolute temperature of the soot particles, λ_1 is the blue wavelength which was set to 450 nm. λ_2 is the red color wavelength which was set to 620 nm.

$$\lambda_1{}^{\alpha} \ln\left[1 - exp\left\{-\frac{C_2}{\lambda_1}\left(\frac{1}{T_{a1}} - \frac{1}{T}\right)\right\}\right] = \lambda_2{}^{\alpha} \ln\left[1 - exp\left\{-\frac{C_2}{\lambda_2}\left(\frac{1}{T_{a2}} - \frac{1}{T}\right)\right\}\right] \quad (4.3)$$

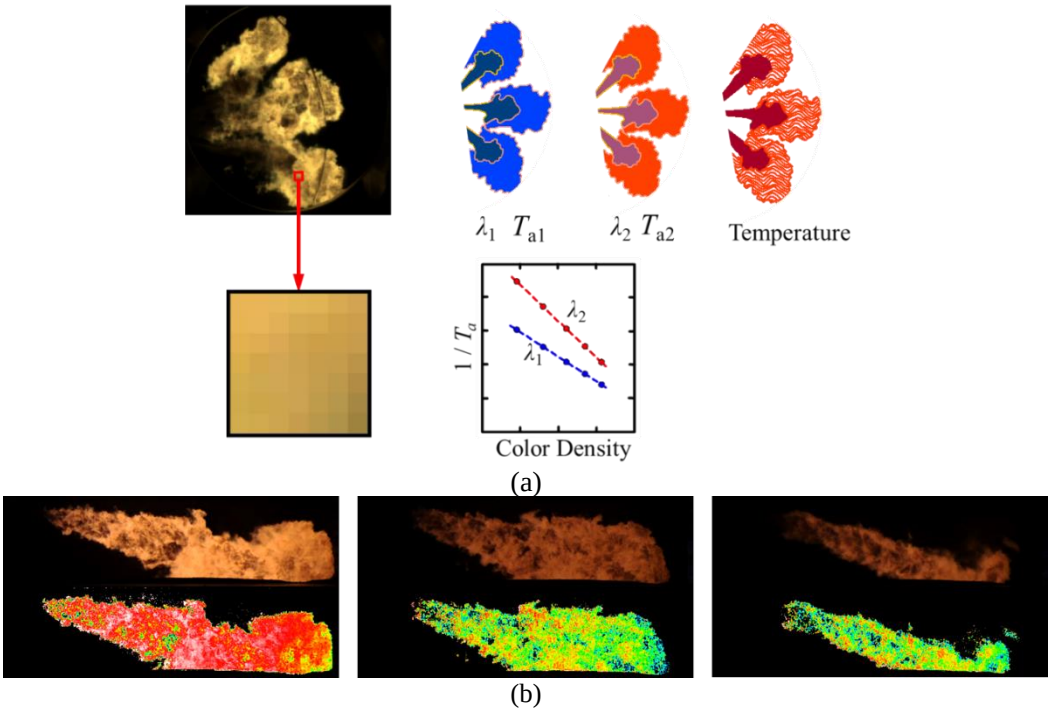

Figure 4.6 Two-color method definition and the application process

4.2.The numerical study

The simulation research was run using four different scenarios, with the water-to-fuel ratio set at 0, 10, 25, and 40. Initially, however, there was a unity-step variation in oxygen content between 16 and 21 %. This range was specifically selected since it included four scenarios where the experimental and simulated research overlapped. KIVA was developed at Los Alamos National Laboratory and is a 3D Computational Fluid Dynamics (CFD) software. The third iteration of KIVA, written in Fortran77, KIVA-3V can calculate combustion processes in a wide range of engines and engine operating parameters. While the KIVA software is useful for combustion calculations, the emulsified fuel with WFE is not considered in the regular KIVA code, making it harder to know combustion under WFE circumstances. Thus, a new model for understanding emulsified fuel was developed in this study. The term "fuel-water concentric spherical model" describes this configuration. The emulsified fuel droplets are shown as two-layered concentric spheres in Figure 4.7, with the outer layer being the fuel that evaporates first. When the fuel is completely vaporized, the inner layer water droplet evaporates. The fuel-water concentric sphere model depicts emulsified fuel evaporation from a mixture of fuel and water. Figure 4.7 represents the model's assumption of two types of droplets: fuel droplets and water/fuel droplets. The ratio of fuel droplets to water/fuel droplets shows the emulsion's water content.

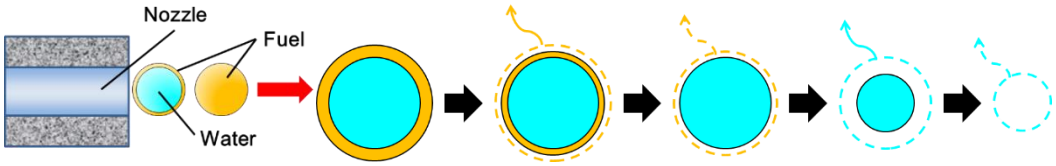

Figure 4.7 Fuel-water evaporation model process

Assuming fuel is injected as spheres with a diameter equal to the nozzle hole, KIVA utilizes the Blob Method. Based on user input, the fuel sphere or fuel-water concentric sphere is injected, and the radius of the water sphere relative to the fuel-water concentric sphere is fixed. To modify the water-to-fuel ratio in WFE, the injection frequency of fuel-water spherical mixtures is varied. KIVA-3V's disintegration model was tweaked to account for fuel and water's concentric spheres. Two separate analytical models make up the break-up model: the Kelvin-Helmholtz (KH) model [77] and the Rayleigh-Taylor break-up model (RT) [78]. When fuel droplets are subjected to unstable surface waves generated by aerodynamic forces, the KH model predicts the formation of new, smaller droplets. Since the KH model's unstable surface wave has such a short

wavelength, the smaller droplets that break off from the parent droplet may be thought of as fuel-only spheres. The RT model, also known as the secondary break-up model, proposes that droplets disintegrate because of the drag force created by the relative velocity between the droplet and the air. In the modified evaporation model, the time step is broken into smaller ones so as not to disrupt the mass balance of fuel if the amount of vaporized fuel is more than the amount of fuel already present in the droplet. In this investigation, the evaporation process was implemented by modifying the evaporation calculation subroutine program.

KIVA uses the Blob Method that assumes fuel is injected as spheres whose diameter is the same as the nozzle hole of the fuel injector. The radius of the water sphere to the fuel-water concentric sphere is set to a constant, determined by users' input data, and which fuel sphere or fuel-water concentric sphere is injected. The total water-to-fuel ratio in WFE is adjusted by changing the injection frequency of fuel-water concentric spheres.

The fuel-water concentric sphere model modified the break-up model used in KIVA-3V. The break-up model consists of two analysis models: the Kelvin-Helmholtz (KH model) and the Rayleigh-Taylor break-up model (RT model). KH model is the primary break-up model in which fuel droplets break up due to unstable surface waves made by the aerodynamic forces, and new tiny droplets are formed. The wavelength of the unstable surface wave in the KH model is so small that the new droplets which split off the parent droplet are treated as the spheres of only fuel. The wavelength Λ and the growth rate of the wave Ω are calculated by equations 3.4 and 3.5. Where the diameter of the new droplet $d_n = 2 \cdot B_0 \cdot \Lambda$, and B_0 is set to 0.61.

$$\Omega \left[\frac{\rho_l {r_0}^3}{\sigma}\right]^{0.5} = \frac{0.34 + 0.38 \cdot {We_g}^{1.5}}{(1+Z)(1+1.4 \cdot T^{0.6})} \tag{3.4}$$

$$\frac{\Lambda}{r_0} = 9.02 \frac{(1+0.45 \cdot Z^{0.5})(1+0.4 \cdot T^{0.7})}{(1+0.865 \cdot {We_g}^{1.67})^{0.6}} \tag{3.5}$$

RT model is the secondary break-up model in which the droplets break up due to the drag force made by the relative velocity between the velocity of the droplet and air. The disintegration of the drop is induced by the inertia of the liquid if drops and ligaments leaving the nozzle with high velocities are strongly decelerated by the aerodynamic drag force F_{aero} It was calculated by equation 3.6. Dividing the drag force by the drop's mass, the interface's acceleration can be found in equation 3.7, C_D is the drop drag coefficient.

$$F_{aero} = \pi r^2 C_D \frac{\rho_g {u_{rel}}^2}{2} \tag{3.6}$$

$$a = \frac{3}{8} C_D \frac{\rho_g {u_{rel}}^2}{\rho_l r} \tag{3.7}$$

Neglecting liquid viscosity, the growth rate Ω, and the corresponding wavelength Λ of the fastest growing wave are described in equations 7 and 8 seting C_3 value to 0.1.

$$\Omega = \sqrt{\frac{2}{3\sqrt{3\sigma}} \frac{\left[a(\rho_l - \rho_g)\right]^{3/2}}{\rho_l + \rho_g}} \tag{3.8}$$

$$\Lambda = C_3 \cdot 2\pi \sqrt{\frac{3\sigma}{a(\rho_l - \rho_g)}} \tag{3.9}$$

In addition, the evaporation model was modified to describe the evaporation processes of emulsified fuel. The new evaporation model of emulsified fuel assumes that the outer fuel evaporates first, then the inner fuel starts to evaporate. The evaporating mass flow is calculated by equation 3.10. The amount of evaporating liquid at a one-time step is calculated from equation 3.10.

$$\dot{m}_{evap} = d_{drop} \pi \rho_l D \ln\left(\frac{1 - Y_{f,\infty}}{1 - Y_{f,R}}\right) S_h \tag{3.10}$$

$S_h = 2.0 + 0.6 Re^{1/2} {S_c}^{1/3}$, $S_c = \mu_g / (\rho_g D)$

In the modified evaporation model, if the amount of the vaporized fuel $\dot{Q}_{fuel}$ is larger than the amount of existing fuel in the droplet, the time step *dt* is divided into the smaller ones not to break the mass balance of fuel. The subroutine program calculating evaporation was modified to implement this study's evaporation process. Table 4.3 illustrates the applied models in the simulation study.

Table 4.3 Analysis models in KIVA-3V

Phenomena	Analysis Model
Primary breakup	Blob model
Secondary breakup	**Modified KH**-RT model
Evaporation	Model of Amsden (water, fuel) + **Two-step evaporation of coaxial drops of water(inner) and fuel (outer)**
Turbulence	RNG k-ε model
Ignition and Combustion	Shell and CTC model

4.2.1.Validity Assessments of Numerical Analysis Calculation

The experimental testing of the EGR, WFE, and their combinations in this paper were performed using an RCEM. KIVA-3V was used to run the simulation, and the fuel-water concentric sphere model was used for the simulation. The constants in the analytical model were assumed to have the same values across all of the different scenarios. The water-to-fuel ratio and the starting concentration of oxygen were both set to the same levels as in the trials. Figure 4.8 illustrates the RCEM calculation domain in KIVA-3V. The predicted cell count for the combustion chamber is 76,000, and the minimum cell length is 5 millimeters. In this investigation, a calculational time step of up to 4 s was used. The potential for droplets to collide was neglected in the computations.

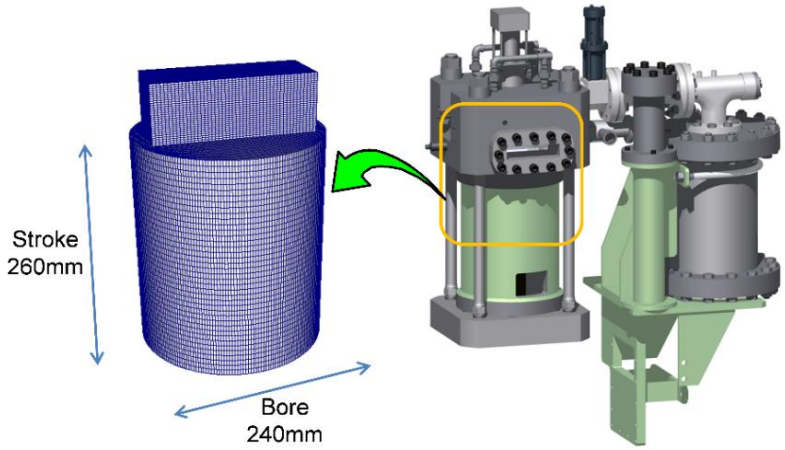

Figure 4.8 The computational domain of RCEM applied in KIVA-3V

The calculated and experimental NOx emissions are compared in Figure 4.9. The predicted NOx emissions are very similar throughout the range, except for the case of a 40% water emulsion, as shown in the figure. As a result of this concordance, it can be concluded that the NOx emissions from the water emulsion may be reliably estimated using the KIVA-3V method utilized in this research. Meanwhile, the rate of heat release is compared between the experimental and computed situations in Figure 4.10. As can be seen in the figure, the calculated Heat Release rate profile is consistent with the experimental examples, with a minor erroneous peak at 15^{o}CA that has no discernible impact on the overall profile. All instances of WFE show a reduction in heat release rate following injection, as seen in the figure. The afterburning time was extended in both the trials and the computations when WFE was used.

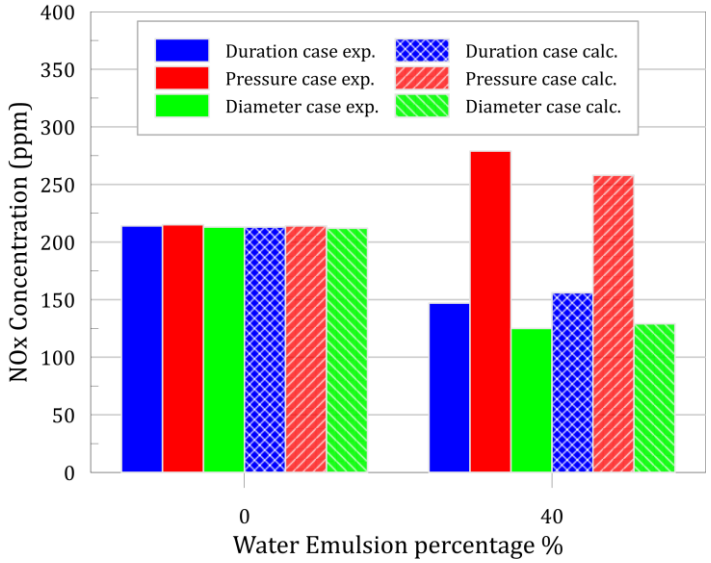

Figure 4.9 NOx emissions in the WFE calculations versus the experiments

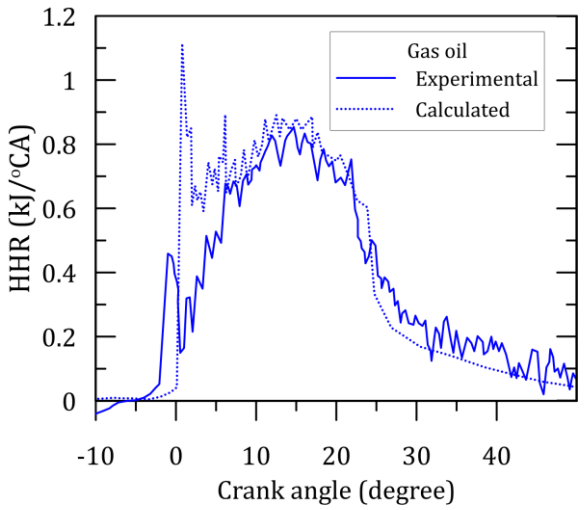

(a)

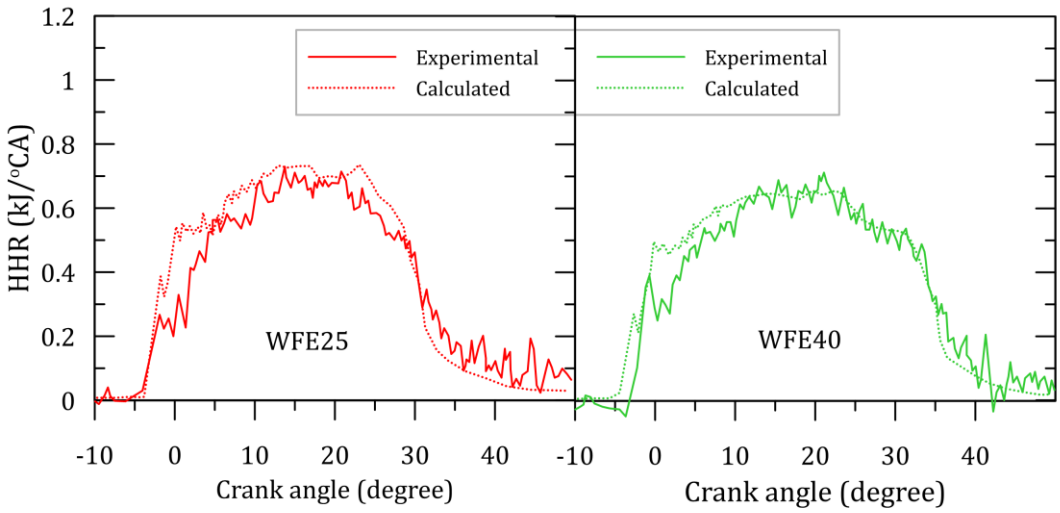

(b)

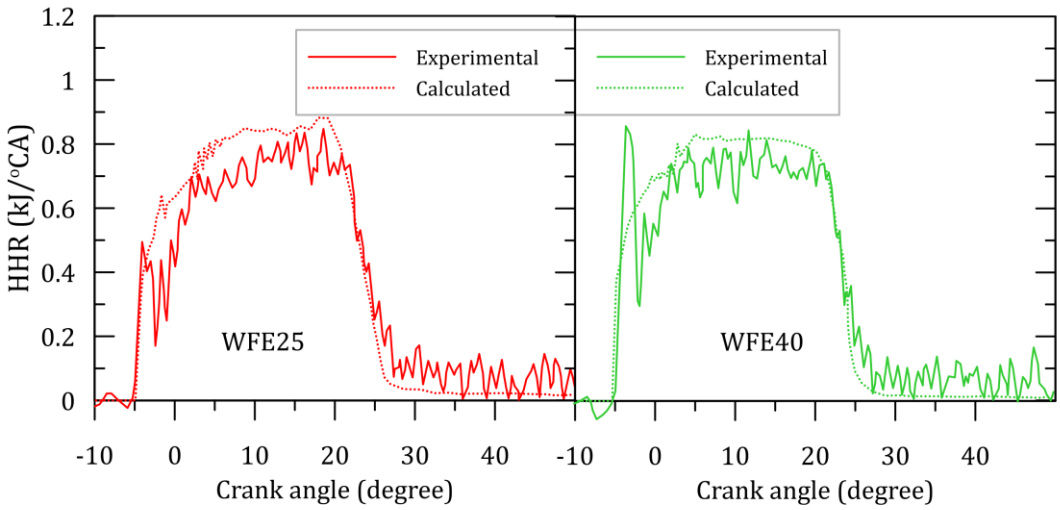

(c)

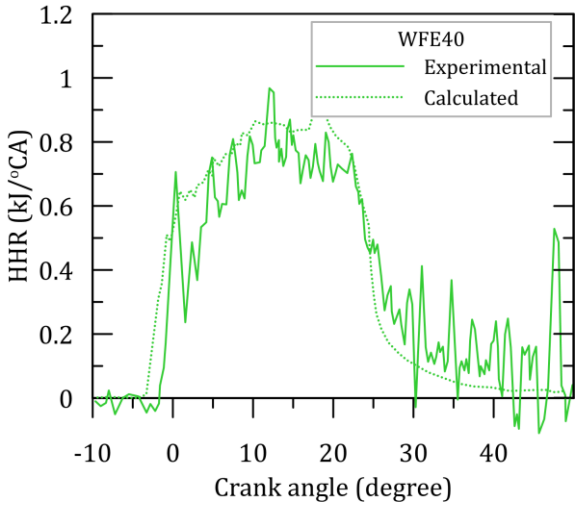

(d)

Figure 4.10 Heat release rate versus crank angle in both experiment and calculated cases a) the heat release rate for a) the gas oil as a base case b) duration case c) pressure case d) diameter case

4.2.2.Uncertainty Analyses

Some inaccuracy and error is to be expected in experimental test outcomes. Experiment accuracy can be affected by several aspects, including but not limited to observations, experiment design, testing equipment employed, experimental settings, equipment calibration, environment, and findings. The precision and correctness of the experimental results were checked using an uncertainty analysis. Table 4.4 provides an overview of the experimental uncertainties and errors. The random variations in the observed data were predicted using analytic methods with the help of Equation (3.4).

$$w_R = \left[\left(\frac{\partial R}{\partial X_1}\cdot w_1\right)^2 + \left(\frac{\partial R}{\partial X_2}\cdot w_2\right)^2 + \ldots\ldots + \left(\frac{\partial R}{\partial X_n}\cdot w_n\right)^2\right]^{1/2} \qquad (4.4)$$

Where w_R is the uncertainty of the measured parameters; $w_1, w_{21}, w_3, \ldots, w_n$ is the error in the independent variables.

Table 4.4 The uncertainty in the measurements and the calculations.

Instrument	Range	Accuracy	Uncertainty (%)
Injection pressure sensor	0-5000 bar	±5 bar	±0.4
Intake pressure sensor	0-2 bar	±0.006 bar	±0.25
In-cylinder pressure sensor	0-250 bar	±0.125 bar	±0.5
CO	0-100 ppm	5 ppm	±0.2
HC	10-20000 ppm	10 ppm	±0.2
NOx	10-10000	10 ppm	±0.25
Calculated quantities			Uncertainty (%)
Flame temperature (TCM)			0.3%
Flame temperature (calculated)			2.5%
IMEP			1.3%
NO			1.5%

In this section we used the software that had been built in our laboratory by Matsumoto et al. [79], we supported some of the results by his previous calculations and here are some of his work as quotation “

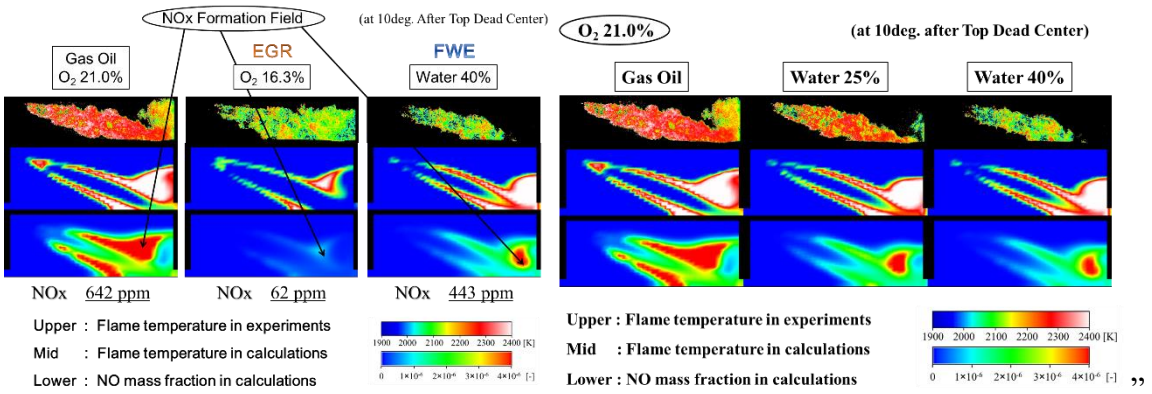

4.3.Flame temperature distribution under EGR,WFE and their combination

Once injected into the engine cylinder, diesel fuel typically self-ignites due to the high temperature and pressure of the surrounding environment. Air entrained into the spray body before ignition supplies oxidizing oxygen. Diesel sprays have a rich core of

combustion because of the minimal air entrained in the spray body, but a lean mixture on the spray's surface due to the entrained air's intensity [48]. The major cause of soot and NOx production is the variation in air/fuel ratio over the spray body. Several scientists have demonstrated the relationship between local temperatures and equivalency ratio after conducting comprehensive studies [80]. Using this map, we may predict that rich area temperatures and equivalency ratios cause NOx and soot emissions to begin at around 2200 K. The flame temperature distribution shown in Figure 4.11 is based on TCM's analysis of pictures taken during experiments. Because the TCM estimated the distribution based on the summation from back to front, there are gaps in the temperature profiles of the combustion flame.

High-temperature spots in the gas oil became less concentrated when the initial oxygen content dropped, as seen in Figure 4.11. For example, in the absence of EGR (% O_2), 95% of pixels on the spray body recorded temperatures higher than 2200 K, 67% of pixels on the spray body achieved this amount at 18.3% O_2, and 8% of pixels on the spray combustion temperature recorded more than 2200 K in the 16.3% O_2 condition. Comparing the (WFE25 with % O_2) instance to the other cases demonstrates that the same impact is also visible in the water emulsion cases. The percentage of captured 2200 K images dropped from 95% in the gas oil example to 74% in the WFE25 with 21% oxygen and 6% in the (WFE25 with 21% oxygen) case. The flame temperature is significantly reduced due to the super positioning (combining the EGR and WFE), with just 3% of the pixels surpassing 2200 K in the case of WFE25 with 18.3% O_2, and local temperatures being dropped below 2100 K in the other three situations. EGR led to a rise in atmospheric carbon dioxide and water vapor concentrations [81]. Since carbon dioxide and water vapor have a lower boiling point than air, they absorb more heat from the flame. As a bonus, the introduction of the inert gases (carbon dioxide and water vapor) reduces the interaction between the spray surface and the oxidizer (oxygen into the environment), resulting in a delayed oxidation process and a consequently slower flame speed [82]. In contrast, WFE lowers the flame temperature by increasing the amount of water evaporation, whose latent heat cools the flame and reduces the number of hot spots [67]. The high latent heat of water and the powerful influence of EGR on the flame speed work together to lower the flame's local spot temperatures.

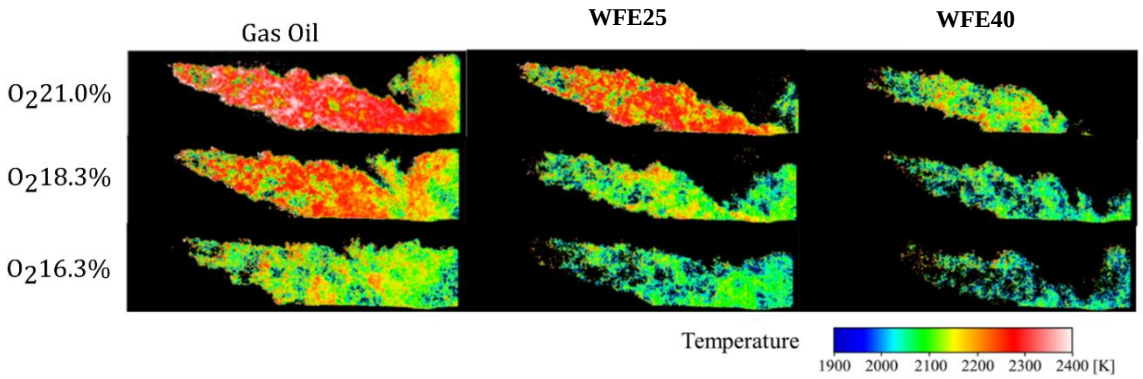

Figure 4.11 Flame temperature distributions calculated by the two-color method at 10°CA ATDC

When changing injection period in the WFE, the temperature and NO fraction distributions are shown in Figure 4.12. The TCM used these images to determine the flame's temperature, which is seen in the upper graph. The NO mass fraction distributions and temperature distributions were shown using the computation results and the visualization program Ensight 8.2. The flame temperature has been observed to reduce considerably when using the two-Color technique, although as can be seen in the image, this effect is not shown in the calculations. As the calculated combustion area grew, the burnt gas temperature increased, and the area along the right wall of the combustion chamber experienced high temperatures. The NO emissions were completely different between the EGR and WFE examples and the pure gas oil cases, even if the flame temperature seems lower in the higher photos. The NO mass fraction distributions calculated by KIVA-3V show that the majority of NO was generated towards the flame front during combustion. However, in the case of EGR, the amount of NO generated was lowered equally. The results of the KIVA-3V calculations showed that EGR and WFE use very different mechanisms for reducing NOx emissions. With EGR, NO byproducts were decreased drastically and consistently. The flame cools down since there is less Oxygen in the air during EGR conditions. Because the Zeldovich process [38] is sensitive to both temperature and the concentration of Nitrogen and Oxygen, there is a synergistic impact that reduces NO production. Despite appearances to the contrary, the front edge of the combustion flame in WFE cases was found to have high temperatures and a considerable amount of NO product. As the water ratio grew, the NO production region in the WFE scenario moved to the combustion flame's leading edge.

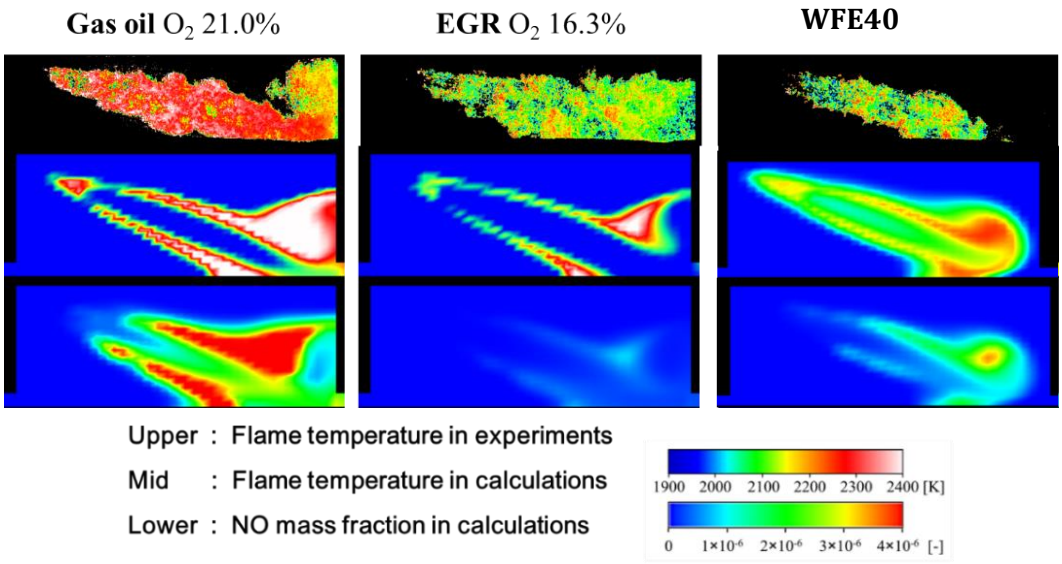

Figure 4.12 The calculated flame temperature and NO compared to the actual photos at10°CA ATDC

The in-cylinder pressure profiles for the CAS and COC examples as a function of the crank angle are depicted in Figure 4.13. As can be seen from the figure, the EGR rate has a far greater impact on the in-cylinder profile in the CAS scenario than it does in the COC situation. The peak pressure that can be reached inside the cylinder is affected by the charging pressure. In addition, installing an EGR in the intake manifold can have an effect on the combustion that occurs within the cylinder itself. This is because a high concentration of carbon dioxide can increase the heat capacity of the ambient temperature within the cylinder, resulting in a slower flame speed and a lower temperature at which combustion occurs. In the case of CAS, a rise in the charge pressure results in an influence on the peak pressure of the combustion process. In contrast to the situation of COC, an increase in the charge pressure results in a marginal rise in the peak pressure produced by the combustion process.

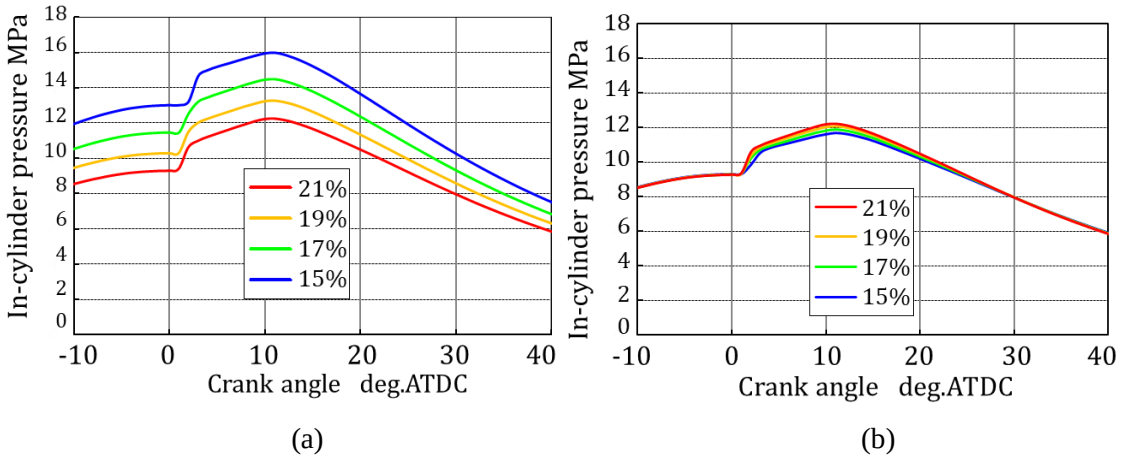

Figure 4.13 In-cylinder pressure versus crank angle for different EGR cases a) CAS b) COC

The rate of heat release is shown as a function of crank angle for both the EGR and WFE scenarios in Figure 4.14. In addition, the first low in thermodynamics is used to determine the heat release rate for the single-zone combustion model [37]. Late crank angle heat release is a sign of afterburning, which reduces overall thermal efficiency. As the EGR technique is used, the oxygen concentration drops and the afterburning time lengthens. Since the fuel-oxygen chemical interaction is slowed by the low oxygen concentration, more fuel remains in the cylinder until a late crank angle, when the cylinder temperature has dropped dramatically. This meant that the heat was still being released far into the late crank angle. However, when WFE is used, the afterburn effect is mitigated. Due to the enhanced velocity of the emulsified fuel provided by the added water mass, WFE increases fuel/air mixing. However, a side impact of WFE is that the fuel's contact area with the ambient environment may be slightly reduced, resulting to less fuel/air mixing. Meanwhile, momentum is the primary driving force; as a result, the majority of gasoline was utilized efficiently, and only trace quantities were left after injection. According to Zhao et al. [83], EGR lengthened both the combustion and afterburning phases. Pan et al. [84] reported an increase in the ignition delay and the HHR peaks when using the EGR.

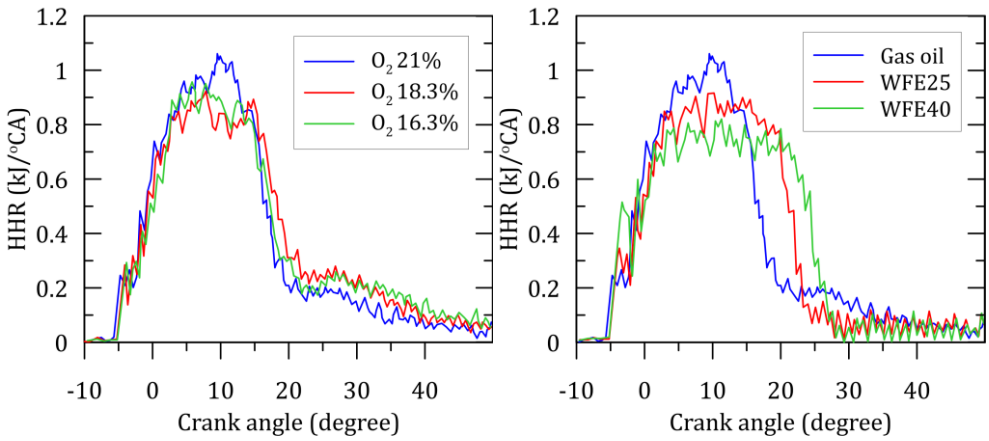

Figure 4.14 Experimental Heat release rate versus crank angle for the two applied cases a) EGR and b) WFE.

The NOx emissions concentrations in the exhaust gas for the various EGR and WFE combination scenarios are displayed in Figure 4.15. In general, when the EGR was used, the NOx emissions dropped from 642 ppm to 182 ppm (18.3 percent oxygen concentration) and 62 ppm (16.3 percent oxygen concentration), recording reduction percentages of 71.7 percent and 90 percent, respectively. While using WFE at 25% and 40% reduces NOx emissions by 2% and 31%, respectively, from 642 ppm to 630 ppm and 443 ppm, respectively. When emulsion is used, the fuel spray momentum is increased,

which improves the mixing of the fuel and air, which in turn reduces NOx emissions. It's possible that the water droplets in a diesel spray will reach the superheated temperature before the diesel fuel, and this micro explosion will help the fuel atomization process forward. Once combustion begins, heat is released, and any remaining water evaporates. The combustion temperature and NOx production are lowered by the heat released during evaporation. Nitrogen molecules, which may react with ambient oxygen at the diesel spray's periphery, are reduced, leading to less NOx production in the EGR instance. Similar reductions in NOx emissions were seen when emulsified gasoline containing water was used in conjunction with EGR. When compared to the pure diesel example, NOx emissions dropped by 91.7% when oxygen content was 16.3%, and by 93.3% when water percentage was 25% or 40%. Water's ability to absorb heat and release it as latent heat during evaporation may be responsible for the lowered flame temperature, which in turn reduces the likelihood of nitrogen-oxygen interaction and boosts the brisk diesel velocity. When the EGR is used, NOx emissions are reduced, notably at low and medium loads, but have essentially no impact at high loads, as shown by Pan et al. [84].

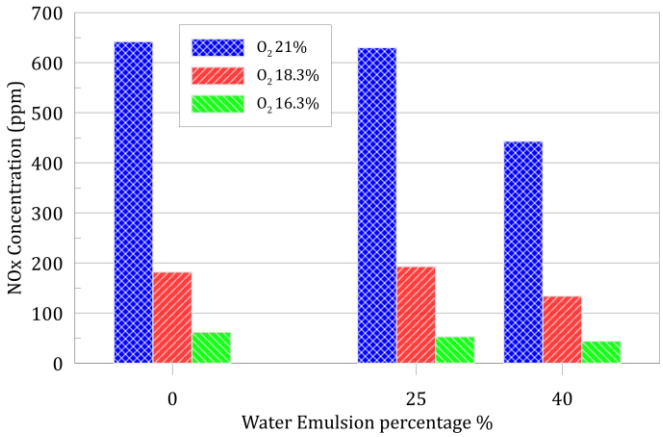

Figure 4.15 NOx emissions concentration in the case of EGR and WFE combination

The CO and HC emissions from the RCEM at varying oxygen percentages are shown in Figure 4.16. Incomplete combustion, which can be produced by low cylinder temperatures and low oxygen concentrations that slow down local oxidation processes, is a common source of carbon monoxide (CO) emissions. There are several potential sources of emissions of unburned hydrocarbons (HC) [63]. Valve overlap during gas exchange allows unburned mixture in the cylinder to escape out the exhaust valve [62]. In addition, when the exhaust valves are opened, the unburned mixture might be emitted from cracks in the combustion chamber. A third reason is that, under cold start conditions, the unburned mixture might be released during the expansion stroke after being absorbed by the lubricating oil used to lubricate the piston and piston rings. Cracks in the

combustion chamber can be a major source of HC formation. Due to a decrease in combustion velocity and flame quenching in the fissures, CO and HC emissions rose as EGR (drop in the oxygen %) was increased [63].

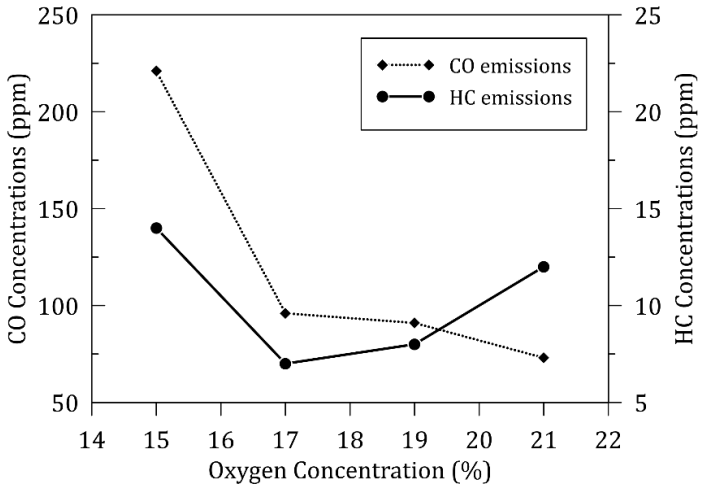

Figure 4.16 CO and HC emissions concentration in the case of EGR

Estimated NO emission decrease from using EGR and WFE gas oil is shown in Figure 4.17. Most of the nitrogen oxides (NOx) produced by diesel engines is "Thermal NO," which is created when nitrogen and oxygen interact directly in a very hot atmosphere [6]. Therefore, the NO emissions from the cylinder are determined here. The amount of NO product was reduced by more than 75% in all cases where the oxygen level was less than 18%. As the amount of water emulsion grew, the effect of EGR on reducing NO was magnified, suggesting that the impact of NO reduction was enhanced when paired with WFE. At 16 % oxygen, the combination of (WFE10), (WFE25), and (WFE40) in the pressure scenario reduced NO by (91, 91.6, and 94)%. This research also included the determination of the Indicated Mean Effective Pressure (IMEP). More often than not, the IMEP dropped by more than 5%; this could be because the longer injection interval leads to a more diffuse fuel-air mixture in the combustion chamber, which in turn leads to a less efficient combustion process. It's possible that the IMEP would be lower if the mixture were more diffuse. Another factor that might reduce IMEP is increased heat loss to the cylinder walls during a prolonged injection duration [13]. To achieve a 5% reduction in IMEP, significant increases in engine propulsion and fuel expenses are necessary. Therefore, in the pressure situation, it is beneficial to use WFE at oxygen concentrations of less than 18.0 percent. There was a 94% reduction in NO product and a 4% increase in IMEP when the oxygen concentration was 16%, the extra water ratio was 40%, and the injection pressure was raised. The NO decrease and the higher IMEP criterion could only be met in this case. In some circumstances, higher NOx and brake-

specific fuel consumption were recorded by Wang et al. [58] when the EGR cooling temperature was raised.

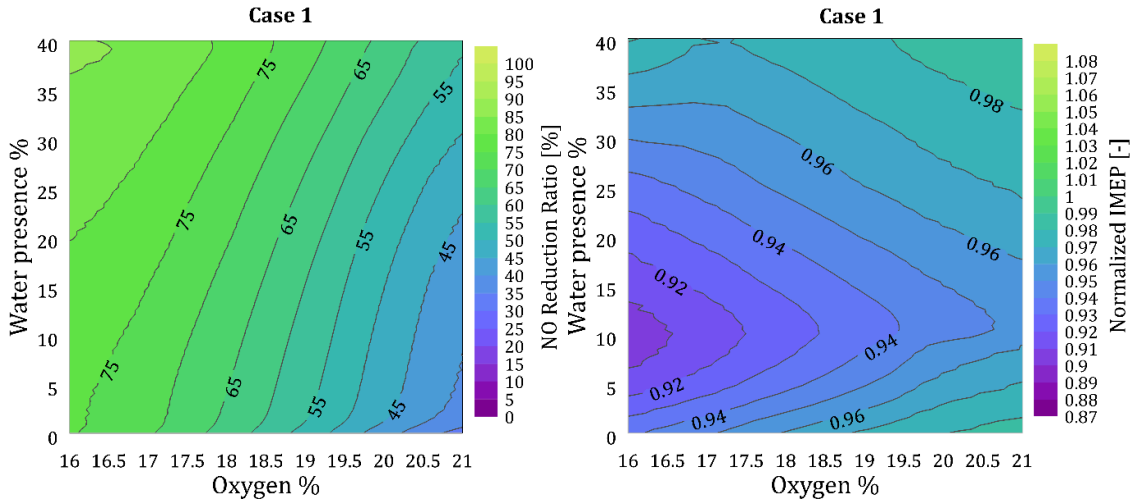

(a)

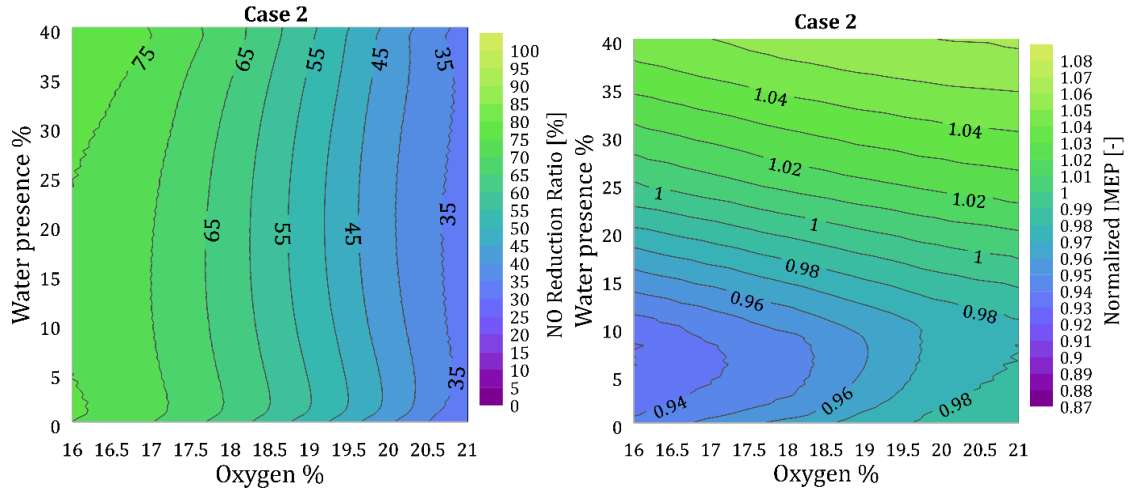

(b)

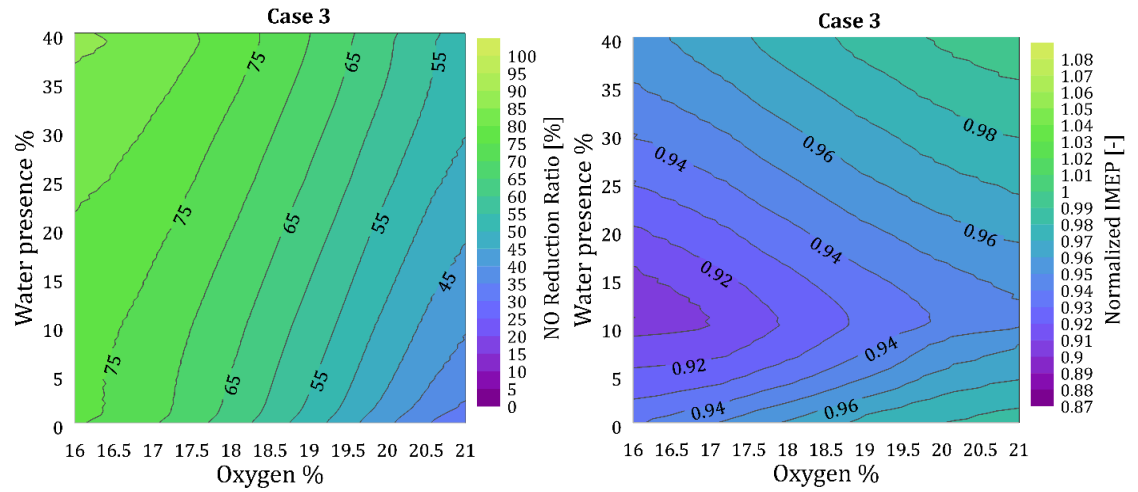

(c)

Figure 4.17 NO reduction and IMEP calculations for EGR and WFE combinations a) injection duration b) pressure c) Diameter case

Chapter 5

Diluted methane and emulsion fuel as a direct injected fuel

5.1.Methodology

This study covers the combustion of methane gas with and without inert gases. Methane has been utilized as a direct-injected fuel combined with, Nitrogen, or Carbon Dioxide gases at blending ratios of (13%), (17.5%), and (24%), and ignited with pilot gas oil (GO). To keep the engine from knocking, we made sure the diluted gas contained at least 70% methane [85]. Both inert gases were blended on a volume basis (v/v percent) to create the diluted gases, which were manufactured using Methane gas at a purity level of 99.9 percent. In addition, the features of water-gas-oil emulsion shown in Table 5.1 have been put to use. Injection state, fuel injection volume, and fuel injection attributes are all displayed in Table 5.1. While Table 5.2 displays the pilot fuel injection conditions and duration.

Table 5.1 fuel properties and injection conditions

Test fuel	Go	GO+ water	CH_4	CH_4+N_2			$CH_4+ CO_2$		
Inert comp. fraction [vol.%]	0	54.6	0	13	17.5	24	14.4	16	17.5
Density [kg/m^3]	887	949	189	217	228	234	249	254	259
LHV [GJ/m^3]	39.3	17.1	9.5	8.3	7.9	7.2	8.1	8.0	7.8
Target injection amount [g]	0.46	0.85	0.4	0.51	0.55	0.62	0.59	0.62	0.64
Target injection heat [kJ]	20								
Injection pressure [MPa]	89.1	60	30.1	30					
Nozzle hole diameter [mm]	0.5	0.8	1.0	1.6					
Inj. timing/duration [^{o}CA]	-6 / 15								
Hole depression angle [degree]	15	15	7.5	15					

Table 5.2 injection condition for pilot fuel

Injection conditions	GO (JIS #2)
Injection pressure [MPa]	40.0
Nozzle hole diameter [mm]	∅0.16
Injection timing/duration [°CA /ATDC]	-8.0 / 7.7
Hole depression angle [degree]	15
Injection heat ratio [%]	~3 % of 20 kJ

5.2.Direct and shadowgraph photos of diluted fuels

Timeframes of combustion processes for pure methane, GO, GO-emulsion, and methane-inert gas mixtures are visualized in Figure 5.1. Injecting the pilot gas oil fuel is the first step in the combustion process for the test fuels. The likelihood of the gas-jet returning and striking the tip of the nozzle is reduced since the set-off length, the distance between the injector hole and the flame, is typically larger than in the case of GO. Diesel fuel has the highest brightness and the lowest cone angle of any fuel. Imhof et al. [32] observed that methane had a dimmer luminosity. The increased hydrogen component of the methane fuel may be to blame, as its regulated combustion phase prevents the formation of Soot. Furthermore, the WEF had the lowest luminosity of all experiments because the water content uses latent energy from the combustion to evaporate, resulting in a lower combustion temperature [7,74]. However, the inert gas made the flame brighter, which may be interpreted as an increase in the amount of mass burned during the premixed combustion stage. It's possible that jet penetration is to responsible for the improved premixed combustion.

The tested diluted fuels' shadowgraphs are represented in Figure 5.2. (Methane, GO, GO-emulsion, Nitrogen, and Carbon dioxide dilutions). Images have typically been compared to the one taken immediately before injection. The direct photographs have been evaluated using a gray pixel matrix. Sometimes the reaction zone of the combustion is much bigger than the brilliant flame, which is depicted by the dark portion of each photo. Pilot gas oil (GO) fuel shows as a brilliant contour when it begins to combust immediately after injection, giving Methane dilution fuel with the ignition, and the expanding Methane jet can be seen in the top lift of each image. The combination of methane and inert gases then burns till the conclusion of the combustion time. Figure 5.3 shows the processed image sample. The gas jet grows till reaching the previously injected gas oil. Using the shadowgraph images, the penetration length of each fuel was calculated. Python Code was developed to detect the penetration length for the gas jet and pilot gas oil, then follow the combustion flame until reaching the end of the visualization window.

All of the test fuels' gas jet and flame penetrations following ignition are shown in Figure 5.4. After igniting from the pilot fuel, the fuel flame spreads along the penetration length with similar behavior, however there are some slight variations in the flame speed. The methane flame had the least penetration of the test fuels, and the GO is not much different from methane. The WEF and methane dilutions, on the other hand,

have longer penetrating times over the whole combustion process. Two percentages, 50% and 80%, of the penetration length were used as benchmarks to make comparisons between the test fuels. The figure shows that the 50% penetration length was obtained at (1.1), (0.8), and (0.1)^{o}CA for pure Methane, GO, and GO-emulsion; (M13), (-17.5), and (-16.4), and (-17.5), and (-0.6), (-0.4), and (-0.4)^{o}CA for M14.4C, M16, and M 17.5C, respectively. Eighty percent penetration was achieved with the aforementioned fuels at (5.8), (6.2), (4.3), and (4.4), (4.5), and (4.4)^{o}CA. Pure methane appears to have a lower penetration rate than nitrogen or carbon dioxide. Blends of methane with nitrogen and carbon dioxide may penetrate the atmosphere up to 50% and 80% farther than methane.

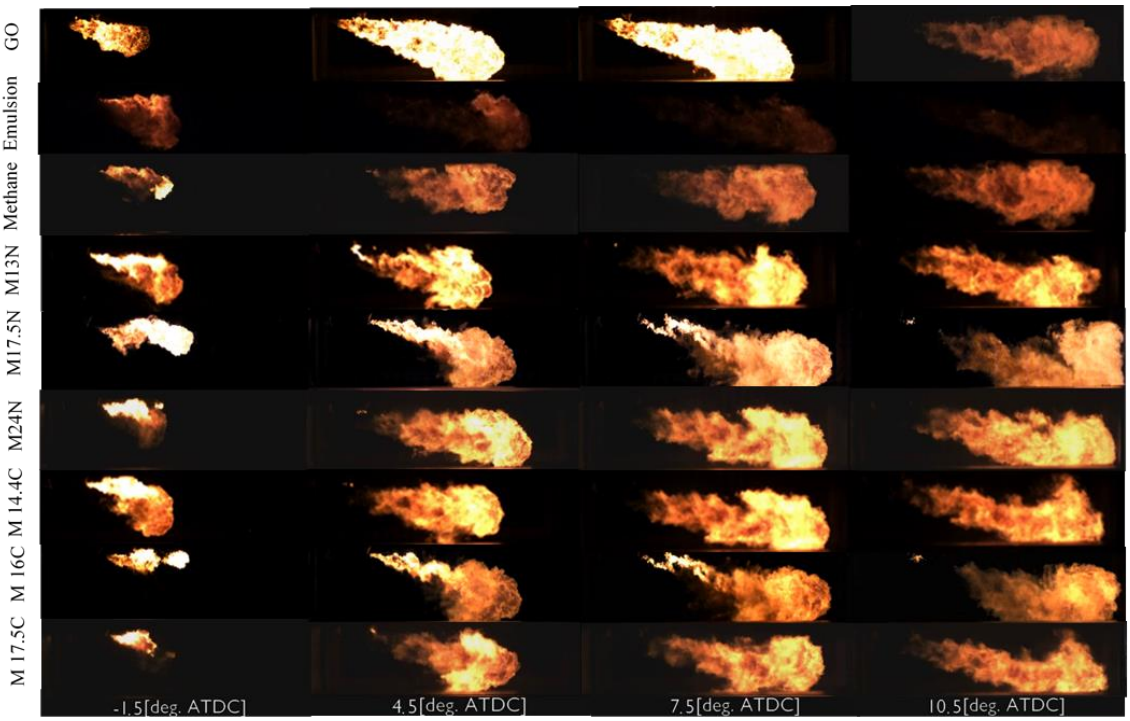

Figure 5.1 direct photos for diluted Methane gas with nitrogen and carbon dioxide gases.

5.3.In-cylinder pressure and heat release rate

Crank angle vs in-cylinder pressure for GO, GO-emulsion, methane, methane-inert gas diluted with nitrogen, and carbon dioxide are plotted in Figure 5.5. The GO was injected 8^{o}CA before top dead center. Gas fuel was supplied after 2^{o}CA to rekindle the flame from the pilot fuel. Cylinder pressure vs. crank angle for the test fuels has the typical motoring pattern, with an initial rapid spike followed by a steady decrease (as seen in the image). The highest pressure measured within the cylinder for GO, GO-emulsion, and methane all hovered around 15.5 MPa. Simultaneously, all dilutions of methane with inert gases showed an increase of roughly 0.5 MPa. These findings corroborate those of Wierzbicki and Mikulski [86]. Diluted methane gas has lower heating values than pure

methane gas, but its peak pressure and pressure rise rate are increased by mixing it with an inert gas, leading to improved flame penetration. A rise in elaborated heat during the premixed combustion phase may account for the diluted fuels.

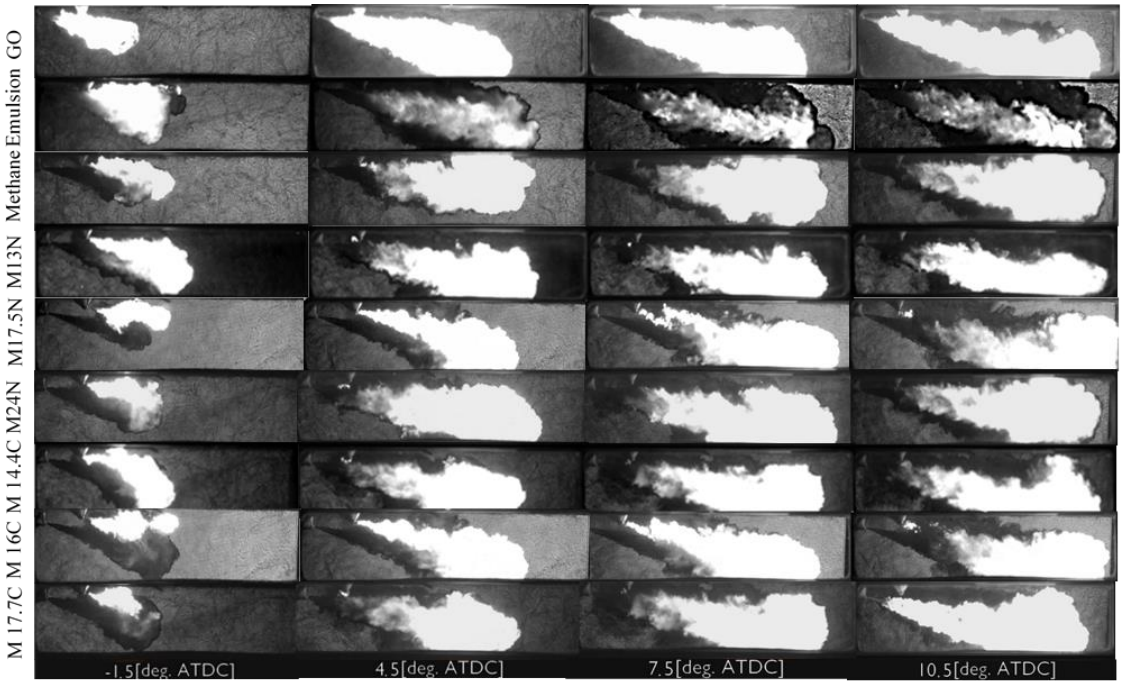

Figure 5.2 Shadowgraph images of diluted Nitrogen and CO_2 gases

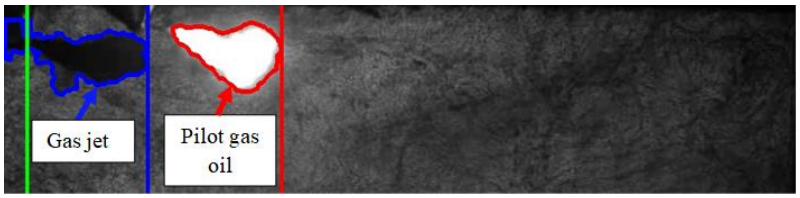

Figure 5.3 Shadowgraph processed image method

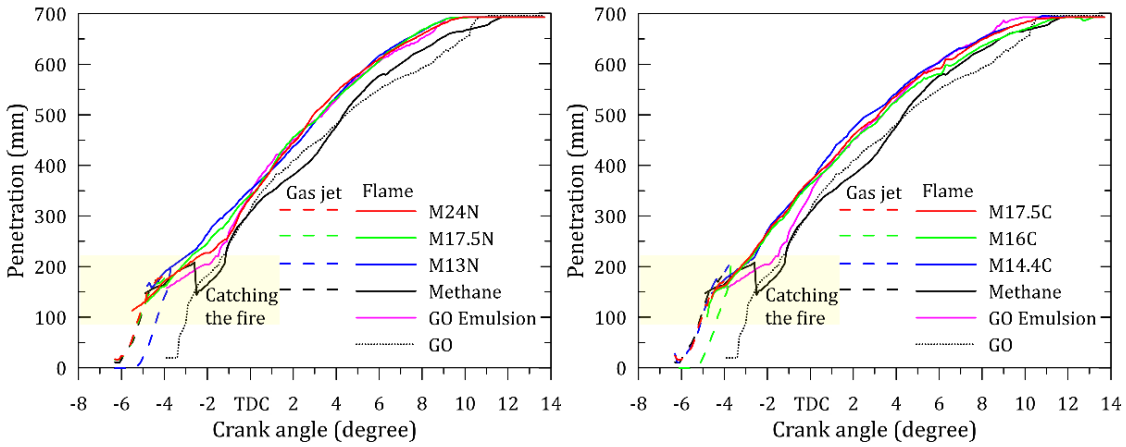

(a) (b)

Figure 5.4 Gas jet and flame penetration versus crank angle for test fuels (a) Methane-Nitrogen Mixture and (b) Methane-carbon dioxide mixture

The rate of heat release was determined by using the observed pressure within the cylinder as a basis for the calculation. Earlier, we talked about the model that had been used to calculate the amount of heat released. Figure 5.6 depicts the Heat Release Rate (HRR) for the gases consisting of methane combined with nitrogen and methane combined with carbon dioxide. The pace at which the pressure is rising can provide some insight into the characteristics of the combustion process taking place within the cylinder [87]. Pure gas oil fuel has been shown to have a lower HRR compared to fuels including methane dilution and gas oil emulsion, respectively. In the case of methane diluted fuels and gas oil emulsion, the amount of heat that is emitted during the premixed phase is more than it is during the pure GO phase. The pace at which heat is released by the emulsion fuel is typically the quickest of all the fuels that were evaluated. While the dilution of methane with inert gases maintains the same trend of the heat that is emitted after the premixed phase. Both [86,88] reported the same set of findings.

Test fuels (GO, GO-Emulsion, methane, methane-nitrogen mixture, and methane-carbon dioxide combination) have their cumulative heat release plotted against crank angle in Figure 5.7. The total amount of heat emitted steadily increased for all test fuels, topping out at about 25^{o}CA. The figure shows that at the outset of burning, both the diluted methane gas and the emulsion fuel release heat more quickly than the pure gas oil. The percentages of heat released at 10, 50, and 90% of the total are useful for describing and comparing the rate of heat release over time. From the figure, the (pure Methane, GO, and GO-emulsion), (M13N, M17.5N, and M24N), and (M14.4C, M16C and M 17.5C) reached CA10 at (1.1, 2.4, and 0.2), (-0.2, -0.2, and 0.2), and (-0.8, -0.4 and 0.1) ^{o}CA, got CA50 at (10.9, 10.5, and 7.6), (8.9, 8.6, and 8.7), and (7.9, 8.2, and 8.4) ^{o}CA, and reached CA90 at (19.1, 17.9, and 21.5), (16.6, 16.9, and 16.1), and (15.4, 15.8 and 15.3) ^{o}CA, respectively. Stewart et al. [89] reached the same conclusion for the behavior of methane gas combustion.

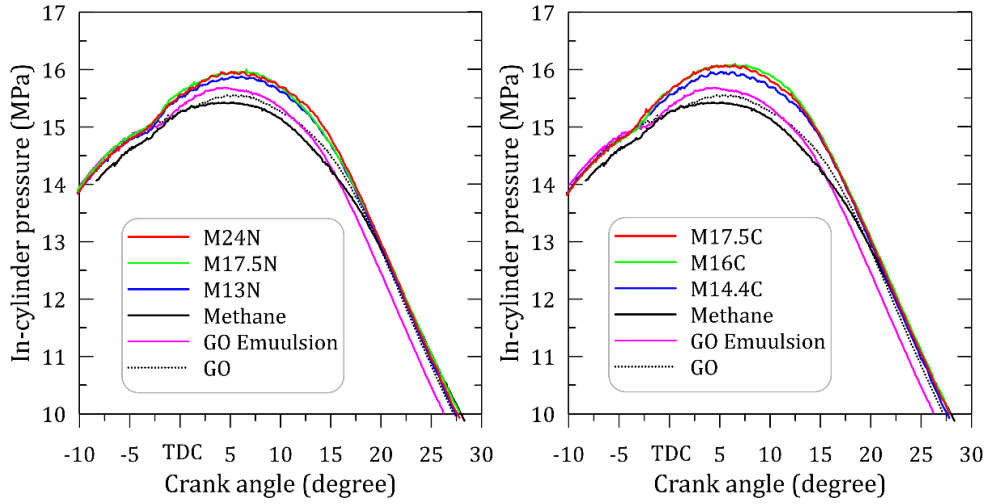

(a) (b)

Figure 5.5 In-cylinder pressure versus crank angle for different tested fuels (a) Methane-Nitrogen Mixture and (b) Methane-carbon dioxide mixture

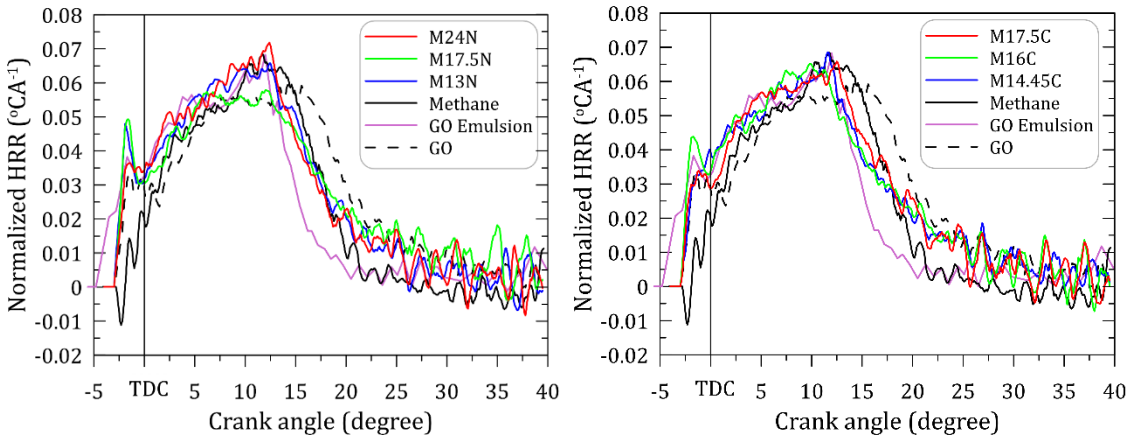

(a) (b)

Figure 5.6 Heat release rate for different tested fuels versus crank angle (a) Methane and Nitrogen Mixture and (b) Methane carbon dioxide mixture

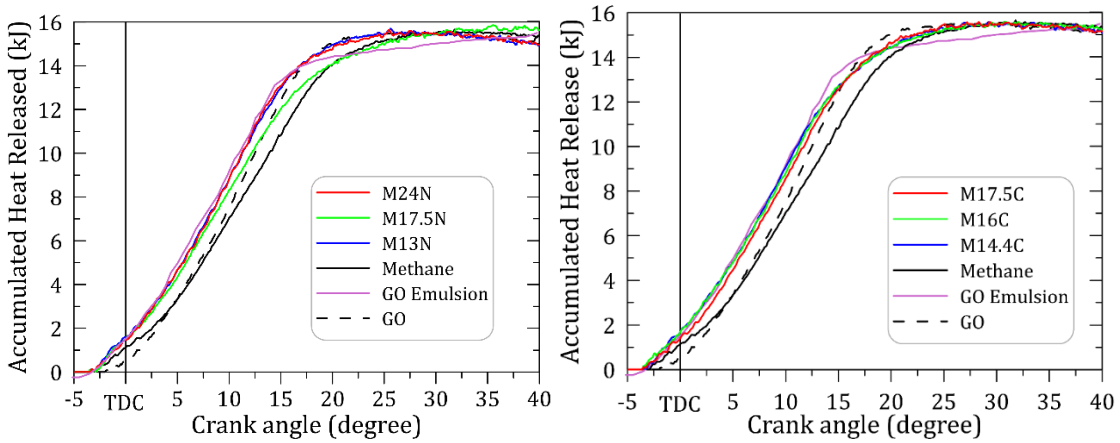

(a) (b)

Figure 5.7 Accumulated heat released for different tested fuels versus crank angle (a) Methane and Nitrogen Mixture and (b) Methane carbon dioxide mixture

5.4.Emissions

The levels of NOx, CO, and HC emissions in the test fuels' exhaust gases are represented in Figure 5.8 All mixtures produced higher HC emissions compared to GO, which are secondary organic compounds created during combustion. The poor reactivity of the methane may be to blame for the rise in HC concentrations. In addition, when nitrogen is added to the methane, the amount of HC produced drops by around 13 percent. The local adiabatic flame temperatures are reduced, which may account for the small drop in HC emissions [90]. Hossain et al. [7] observed similar findings for the emulsion, finding that NOx levels were lower than the GO for all test fuels. NOx emissions were shown to be reduced by blending methane with inert gases as opposed to using pure methane. This reduction may be attributable to the methane-inert blends' extended combustion duration and enhanced premixed phase combustion. Maximum reductions in NOx emissions by blending nitrogen and carbon dioxide are 62% for M17.5N and 54% for M17.5C compared to gas oil emissions. In the instance of gas oil emulsion, NOx emissions were shown to reduce by a whopping 95% Lower NOx reduction may result from the use of methane gas as a diluent since the gas has a lower heat capacity than water emulsion in liquid fuels. Carbon Dioxide levels have also been identified, and unlike with pure methane and gas oil, no discernible distinctions between methane-Carbon Dioxide and methane-Nitrogen have been observed. Kakaee et al. [91] also found the same thing for NG. The effective combustion process may lend credence to this explanation.

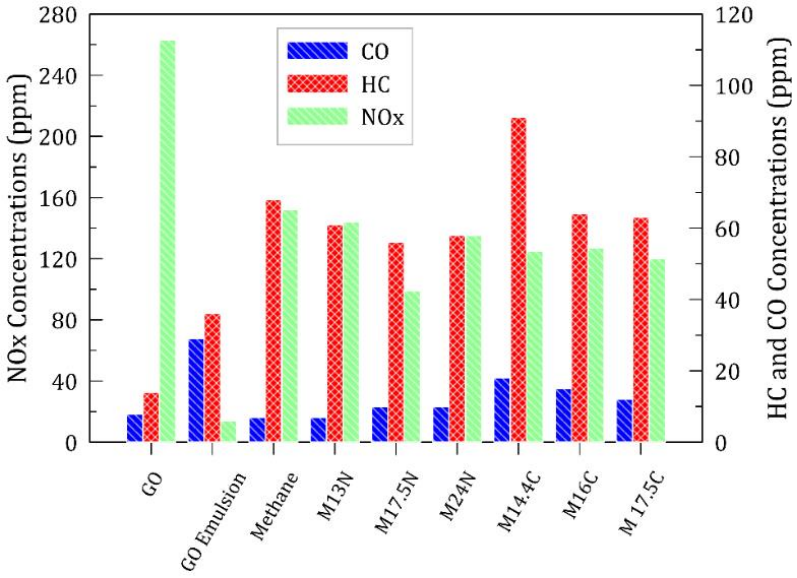

Figure 5.8 Exhaust gas emissions for test fuels

Chapter 6

Methane-Hydrogen as a direct injected fuel

Graphical Abstract:

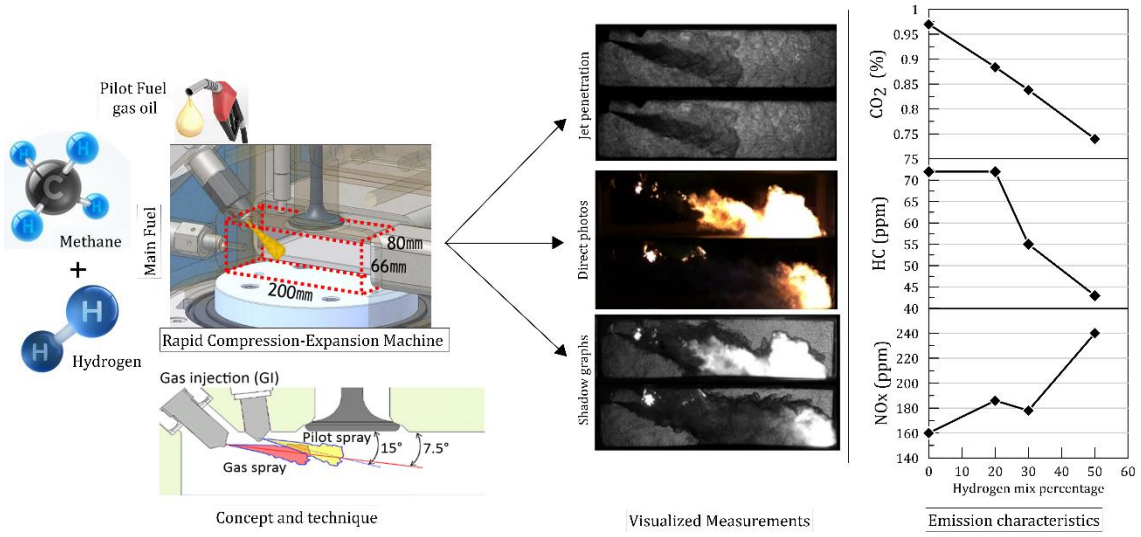

6.1.Methodology

This section describes the use of methane-hydrogen (20, 30, and 50 v/v percent) provided by Fukuoka oxygen co. Ltd, Fukuoka, Japan as the main fuel for a Rapid Compression Expansion Machine (RCEM). Among other researches, Figure 6.1 shows the proportion of applied methane-hydrogen mixing dependent on energy. Two separate investigations form the basis for this research. Methane-hydrogen mixtures with 20, 30, and 50 vol/vol percent hydrogen were injected at 30 MPa into a 3 MPa nitrogen atmosphere and their jets were then investigated. The impact of different injection pressures on M20H jet penetration (15, 22.5, 30 MPa) is also being investigated. In this initial stage, the RCEM was utilized as a constant volume chamber (CVC) by holding the piston at TDC. The shadowgraph method was used to observe the jet's motion in the CVC.

In the second section, synchronized direct photographs and shadowgraph approaches were used to conduct combustion investigation on the hydrogen-methane blends (20, 30, and 50 v/v% of hydrogen) at two compression pressures, 8 MPa and 15 MPa. The HORIBA MEXA-7100FX exhaust gas analyzer was also used to quantify the engine's emissions production. Primary fuel for the RCEM was gas fuel, while the 0.02 cm^3 of gas oil (GO) used as pilot fuel accounted for 3.5% of the total heat release. Methane, hydrogen, and their mixes are listed together with their chemical and physical characteristics in Table 6.1. To guarantee a nearly constant total heat release for all scenarios, the injection parameters of the methane-hydrogen jet were kept the same, as indicated in Table 6.2, while the diameter of the gas injector and the injection pressure were adjusted. The methane-hydrogen jet was ignited using a GO pilot with the injection parameters listed in Table 6.3. Both the GO and the jet were injected at an angle of 15°, apart from the methane, which was injected at an angle of 7.5°.

Table 6.1 Physical and chemical properties of the hydrogen methane mixtures.

Fuel name	CH_4	H_2	M20H	M30H	M50H
Mix rate of H_2 [volume %]	0	100	20	30	50
Molecular weight [10^{-3} kg/mol]	16	2	15.57	15.29	14.44
Density (0°C, 0.101325 MPa) [kg/m^3]	0.71	0.090	0.592	0.529	0.403
Theoretical amount of air [m^3N/m^3N]	9.53	2.38	8.100	7.385	5.955
Lower Heating Value [MJ/m^3]	35.51	10.79	30.56	28.09	23.15
Hydrogen sharing ratio by heat [%]	0	100	7.1	11.5	23.3

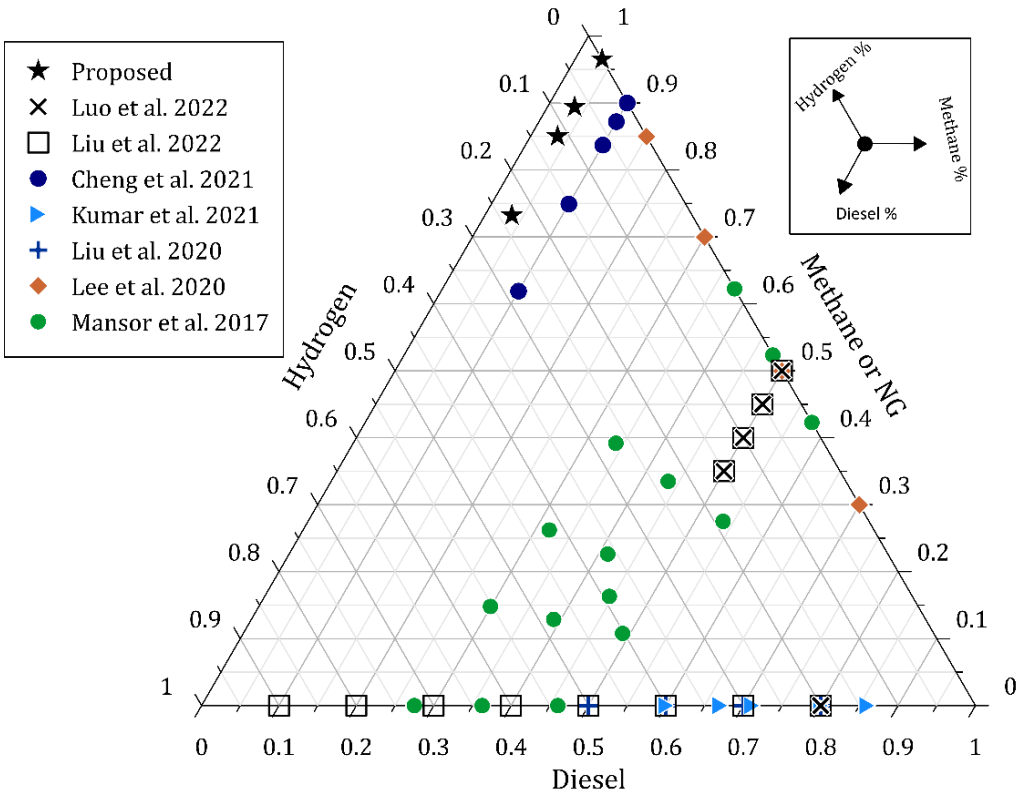

Figure 6.1 Methane-hydrogen mixing percentages in this study and previous studies on energy bases. (Luo et al. [53], Liu et al. [54], Cheng et al. , Kumar et al. [52], Liu et al. [55], Lee et al. [42], and Mansor et al. [92]).

Table 6.2 Injection conditions for the gas jet.

Case name	Compression pressure (8 MPa)			
Fuel	CH_4	M20H	M30H	M50H
Nozzle hole diameter [mm]	1	1.2	1.2	1.2
Angle of injection direction [°]	15	15	15	15
Main injection Pressure [MPa]	30	26.4	27.7	30.7
Main injection start [deg. ATDC]	-5.3	-5.3	-5.3	-5.3
Main injection duration [deg.]	20	20	20	20
Pilot injection start [deg. ATDC]	-6.4	-6.4	-6.4	-6.4
Pilot injection duration [deg.]	7	7	7	7
Case name	Compression pressure (15 MPa)			
Fuel	CH_4	M20H	M30H	M50H
Mix rate of H_2	1	20	30	50
Nozzle hole diameter [mm]	1	1.2	1.2	1.2
Angle of injection direction [°]	7.5	15	15	15
Main injection Pressure [MPa]	30.1	26.5	28	31.2

Main injection start [deg. ATDC]	-5.3	-5.3	-5.3	-5.3
Main injection duration [deg.]	18.5	18.5	18.5	18.5
Pilot injection start [deg. ATDC]	-8.8	-8.8	-8.8	-8.8
Pilot injection duration [deg.]	7.7	7.7	7.7	7.7

Table 6.3 Injection conditions for pilot fuel.

Injection conditions	Gas oil (JIS #2)
Injection pressure [MPa]	40
Nozzle hole diameter [mm]	∅0.16
Inj. timing/duration [°CA /ATDC]	-8.0 / 7.7
Injection angle from the horizontal [degree]	15
Injection heat ratio [%]	~3.5% of 20 kJ

6.2.Experimental Uncertainty Analyses

It is reasonable to assume some level of inaccuracy or uncertainty in the results of experimental tests. Observations, hypothesis testing, test apparatus, conditions, calibration, environment, and readings may all affect the reliability of an experiment. Repairability and correctness of experimental data may be verified by uncertainty analysis [93]. The experimental errors and uncertainties are shown in Table 6.4.

Table 6.4 List the measuring range, accuracy, and uncertainty.

Instrument	Range	Accuracy	Uncertainty (%)
Injection pressure sensor	0-5000 bar	±5 bar	±0.4
Gas pressure sensor	0-5 bar	±0.02 bar	±0.2
Intake pressure sensor	0-2 bar	±0.006 bar	±0.25
In-cylinder pressure sensor	0-250 bar	±0.125 bar	±0.5
CO_2	0.5-20 vol%	0.04%	±0.15
HC	10-20000 ppm	10 ppm	±0.2
CO	0-100 ppm	5 ppm	±0.2
NOx	10-10000	10 ppm	±0.25

6.3.Penetration measurements for the Methane-hydrogen jet

The pressure ratio is a critical variable that can dramatically affect jet properties (the ratio of injection pressure to chamber pressure). The mass flow rate is affected by the pressure ratio. As a result, it is possible to compute the velocity of the incoming jet [94]. More turbulence and faster mixing of the gas and air in direct injection engines may be achieved at higher pressure ratios [95]. This effect was studied and validated by Abdelhameed et al. [96], who found that increasing the injection pressure might raise the average speed of the air entrained in the jet body, hence improving the mixing of the methane and the air. Figure 6.2(a) depicts the M20H jet penetration at three different pressure ratios (5, 7.5, and 10) with injection pressure ratings of 15, 22.5, and 30 MPa and a constant back pressure of 3 MPa. Jet penetration as a function of time ASOI is shown in Figure 6.2(a). Figure indicates that higher injection pressure resulted in deeper jet penetration and wider dispersion of the Methane-blends compared to the methane. For instance, raising the Pr from 5 to 7.5 (50%) and from 7.5 to 10 (33%), respectively, results in a median increase of 18% and 10% in the M20H jet penetration length from 2 to 5ms ASOI. Meanwhile, Yeganeh et al. [97] found that a 20% increase in pressure ratio increases the penetration length by 13% for hydrogen and 17% for methane, respectively.

Figure 6.2(b) illustrates the structure of methane-hydrogen jet in a nitrogen ambient at pressure ratio =10, ($Pr = P_i/P_{ch} = 30\ MPa/3\ MPa$). The figure shows the overall view of the methane-hydrogen blends. Jet penetration measurements for methane-hydrogen mixtures show some variability around the methane penetration (Figure 6.2(b)). Methane-hydrogen mixes, on average, have a shorter penetration length than methane by around 5 percent. Hydrogen molecules are so light that they may increase axial and radial diffusion in the ambient. The shorter penetrating and wider jet found [97] can be attributed to the density difference between methane and methane-hydrogen mixes. Graham's law of diffusion, which states that "the rate of diffusion or effusion of a gas is inversely proportional to the square root of its molecular weight" [98], is consistent with these findings. Under the identical circumstances of temperature and pressure, the rate of diffusion (r) is shown by Equation to be proportional to the square root of the mass density (d) since the mass density is directly proportional to the gas molar mass Equation (5.1).

$$r \propto 1 / \sqrt{d} \tag{5.1}$$

Furthermore, the molecular weight of the CH_4 jet determines its penetrability rather than its dispersion into the ambient environment [94]. These findings are consistent with those of Yeganeh et al. [97], who conducted an experimental comparison of methane and hydrogen jets and found that the latter had lesser penetration.

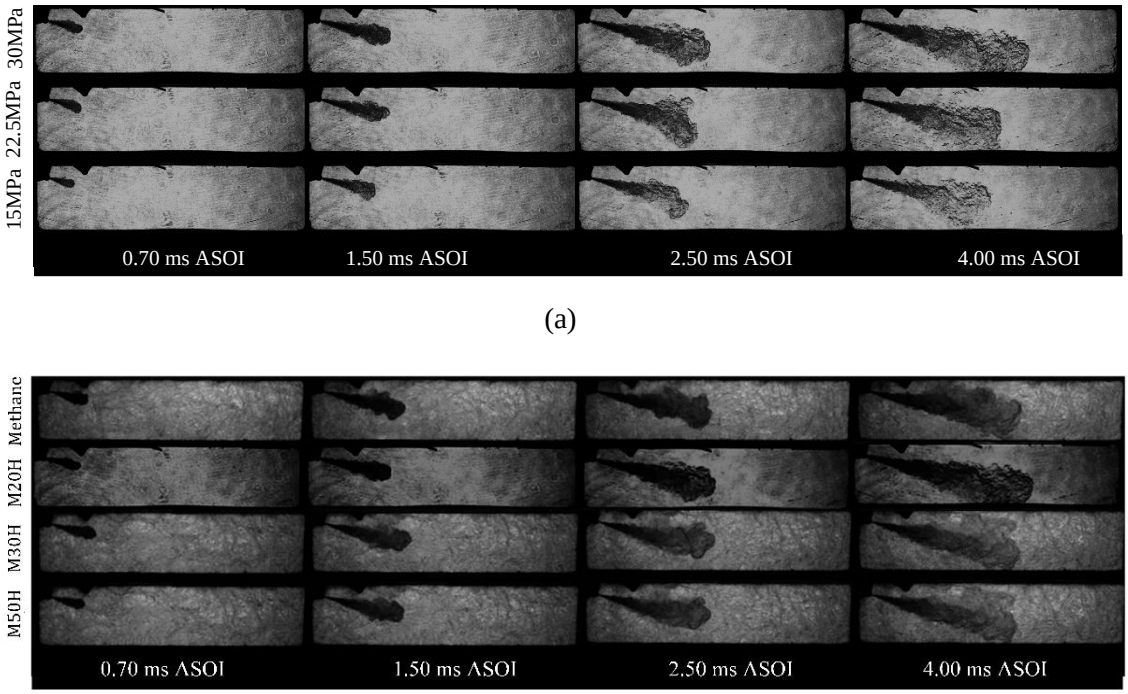

Figure 6.2 Shadow graph for the methane-hydrogen jet in a nitrogen a) M20H under different pressure ratios b) different methane-hydrogen blends (M20H, M30H, and M50H) under constant pressure ratio (*Pr*=10).

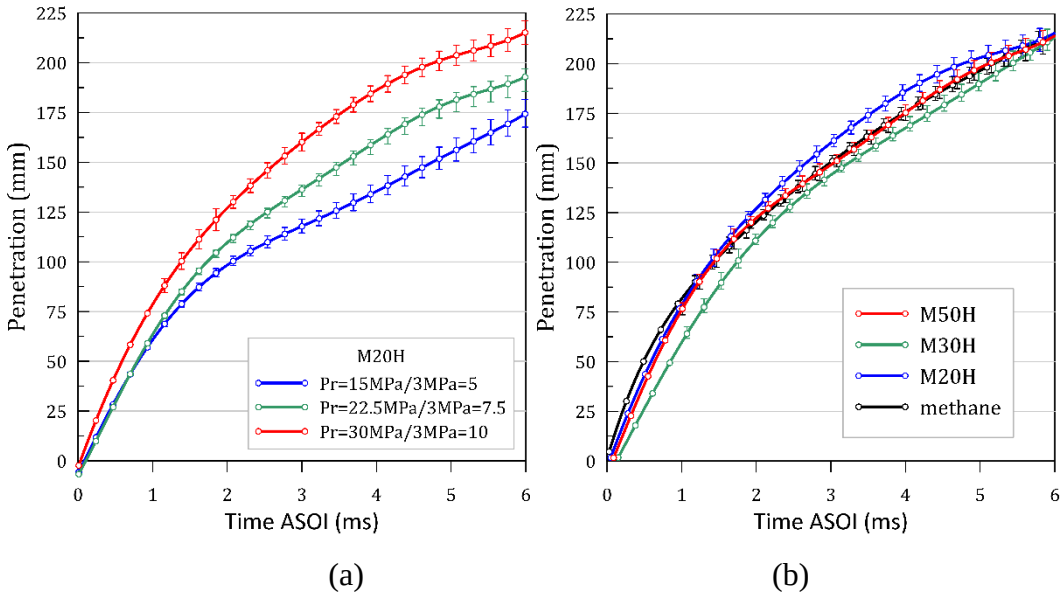

Figure 6.3 Penetration versus time in a nitrogen ambient a) M20H with different pressure ratios and b) different methane-hydrogen blends under the same pressure ratio.

6.4.Direct photos and shadowgraphs

The combustion of hydrogen-methane blends vs crank angle at two distinct compression pressures is visualized in Figure 6.4 using synchronized direct images and shadowgraphs. After injection at 8°CA ATDC, the pilot GO begins combustion, sparking the gas jet into action. The pilot GO fuel burns off almost at -6.9°CA, with an igniting delay of 1.1°CA. Meanwhile, injection of the gaseous mixture began at -5.3°CA, sparking ignition from the pilot GO. Due to the strong reactivity of hydrogen, the combustion process is more robust in methane-hydrogen mixes, resulting in a shorter visible diffusive combustion [77]. Because of this, the hydrogen-methane jets are more vibrant than the pure orange of the methane jet. In contrast, M50H's light blue flame evolved into a sharper one [87].

Chemical reactions can take place throughout a larger area in diffusion flames than in premixed flames, which only have a small reaction zone [80]. The reaction zone of the methane-hydrogen mixes combustion may be seen in the shadowgraphs (see Figure 6.4). When compared to methane, the expansion of the reaction zone for M20H, M30H, and M50H at 8 MPa was 7%, 7.3%, and 7.7%, respectively; at 15 MPa, those values were 10%, 19%, and 30%, respectively. Elemental reactions (OH) involving hydrogen have a role in expanding the reaction zone. Since $CH_4+OH=CH_3+H_2O$ [90], the production of OH promoted the methane's dissociation. However, the shadowgraphs from -1.5°CA to 5°CA ATDC were used to determine flame penetration, an important metric of jet combustion (from the start of combustion until the flame reached the wall). M20H has a flame penetrating property similar to that of methane. The flame penetration for methane at 8 MPa increased to 6% for M30H and 7.5 % for M50H when the hydrogen fraction was raised. Flame M20H penetration at 15 MPa was comparable to methane penetration, but flame M30H and M50H penetration increased by 3% and 8.5%, respectively. The fast flame speed of hydrogen (292 cm/s) contributes to the increased flame penetration [99]. By adding 40% hydrogen to the mixture, the methane flame speed may be increased from 37 cm/s to 53 cm/s [100]. At the same time, it was discovered that the flame jet penetration is negatively correlated with the compression pressure. The penetration lengths of methane, M20H, M30H, and M50H all shrank by 13%, 16%, 19%, and 9.4%, respectively, at 15 MPa compared to the 8 MPa example. The increased drag on the jet's surface is caused by the greater density of the in-cylinder ambient [99]. Air entrainment in the jet

was also boosted by the enhanced turbulence caused by the increased drag on the jet's surface [101]. The improved combustion efficiency of the 15 MPa compared to the 8 MPa can be explained by the larger volume of air entrained in the jet body at the higher pressure.

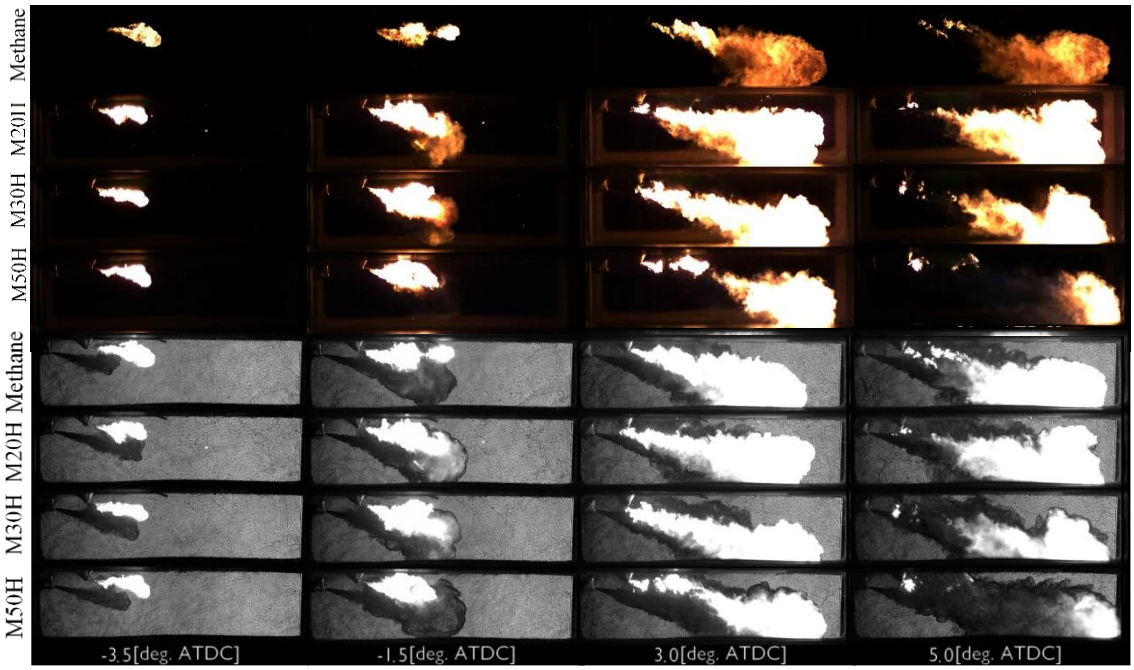

(a)

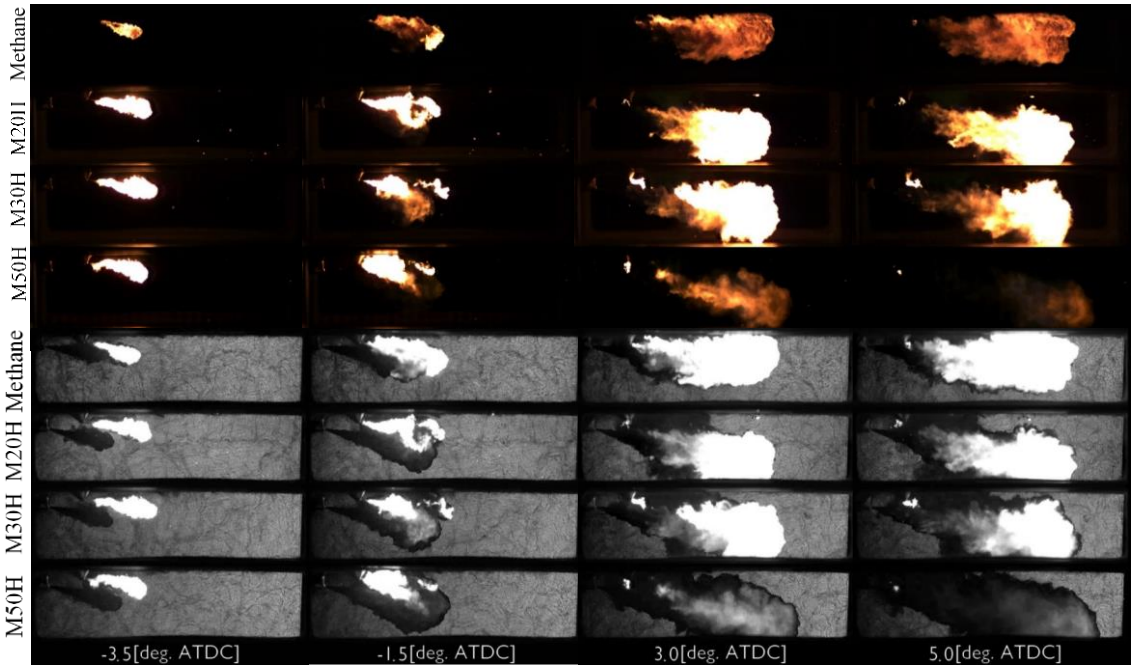

(b)

Figure 6.4 Direct photos and shadowgraphs for methane-hydrogen blends combustion when applying different compression pressures, a) 8 MPa b)15 MPa.

6.5.In-cylinder pressure and heat release rate

Cylinder pressure versus crank angle for various methane-hydrogen mixtures is shown in Figure 6.5. As can be seen in the graph, the higher the compression pressure, the greater the influence within the cylinder. Initial pressure and temperature are high because of the high energy produced in the cylinder during the driving phase [102]. Figure 6.5(a) depicts in-cylinder pressure curves that are quite similar across all blends for the 8 MPa scenario; however, Figure 6.5(b) demonstrates a significant rise in in-cylinder pressure across all blends relative to pure methane at 15 MPa. M20H, M30H, and M50H blends based on methane all saw increases in peak in-cylinder pressure of 5.6%, 5.74%, and 7.5%, respectively. Since the laminar flame speed rises linearly with the amount of H_2 in the mixed fuel, adding H_2 to hydrocarbons can improve combustion, as indicated by Benbellil et al. [103]. The use of H_2 can boost the combustion rate, which was attributed by He et al. [90] to an increase in OH and H radicals. When using 15–35% and 35–60% hydrogen, NG, and diesel, respectively, compared to 50–50 diesel/natural gas, Luo et al. [53] found a similar trend of in-cylinder rise to reach 27%.

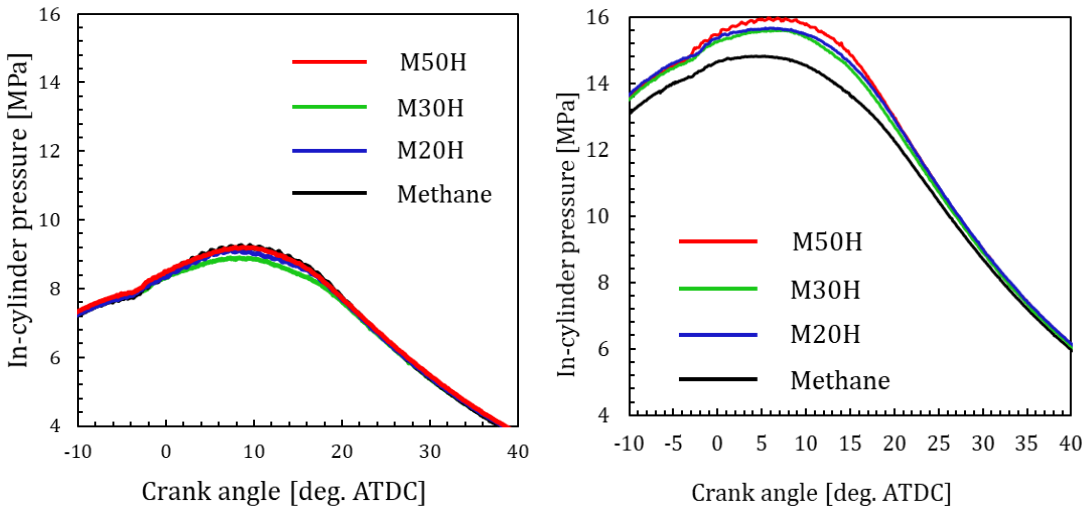

Figure 6.5 In-cylinder pressure versus crank angle for different hydrogen-methane blends at two compression pressures a) 8 MPa and b) 15 MPa.

Figure 6.6 shows the Heat Release Rates (HRR) for the methane- hydrogen mixtures versus the crank angle. A single-zone model [104] was utilized to calculate the heat release rate ($dQ/d\theta$) based on the measurements of the in-cylinder pressure. A cylinder's combustion process may be described by its rate of pressure increase [87]. Evaporation of the pilot gas oil (GO) during injection explains the subsequent decrease

in heat release rate along the negative axis. The gas jet ignites as the GO begins to self-ignite. Benbellil et al. [103] found two peaks with distinctive patterns of heat emission. The first one depicts diesel combustion, and the second one is an example of premixed gas combustion. When more than 60% hydrogen is applied, the second peak from the combustion of premixed gas might result in PREMIER combustion and even banging, as documented by Cheng et al. [51]. In this research, one peak in heat release occurred after the use of direct gas jet injection, and this was followed by controlled diffusion.

As can be seen in Figure 6.6(a), all of the blends showed the similar HHR peak value at 8 MPa in the premixed state. At 8 MPa, the kJ/^{o}CA values for methane, M20H, M30H, and M50H were 0.74, 0.51, 0.74, and 0.75. While the peak heat release in the premixed phase is almost 0.7 kJ/^{o}CA for methane at 15 MPa (Figure 6.6(b)), the hydrogen-methane blends produce 1.2 kJ/^{o}CA for M20H, 0.8 kJ/^{o}CA for M30H, and 1.1 kJ/^{o}CA for M50H. Hydrogen addition increases OH concentrations, which may be viewed as an expansion of the methane reaction zone [90]. The higher heat output of the premixed combustion stage in dual fuel mode compared to methane [90] can be explained by the enlargement of the methane consumption zone. The rapid flame speed of the hydrogen may also contribute to the heightening of the premixed peaks [99].

The amount of heat emitted for the hydrogen-methane mixtures is shown in Figure 6.6 as a function of the crank angle. At 25^{o}CA, all mixtures had nearly completed accumulating heat. However, the rates of accumulation are not the same. Thus, 10%, 50%, and 90% of the total heat released were classified as CA10, CA50, and CA90, respectively, to characterize the cumulative heat release variance. Combustion epochs (CA10, CA50, and CA90) for 8 and 15 MPa methane-hydrogen mixtures are depicted in Figure 6.7. In the instance of 15 MPa compression pressure, M30H has the lowest CA50 and CA90 by 8.1^{o}CA and 14.6^{o}CA, respectively. While this is going on, the CA50 and CA90 values for pure methane are respectively 10.7^{o}CA and 18.9^{o}CA. Comparatively, in the 8 MPa compression scenario, the CA50 and CA90 values for M30H are 8^{o}CA and 15^{o}CA, respectively, whereas they are 13^{o}CA and 19^{o}CA, respectively, for pure methane.

Combustion durations at 8 and 15 MPa compression pressure for various methane-hydrogen mixtures are shown in Figure 6.8. Total time per crank angle between 10% and 90% of total heat emission is considered the combustion duration [54]. At 8 MPa, the combustion time of M20H, M30H, and M50H is reduced by 4.9%, 10%, and 5.8%, respectively, when hydrogen is added to the methane. There was a 7.5% drop, 5.7%

decrease, and 11.5% decrease in combustion time for M20H, M30H, and M50H methane-hydrogen blends at 15 MPa. Combustion times were cut by 11.5% and 5.7%, respectively, using M50H at 8 MPa and 15 MPa compression pressures. Improved combustion and greater in-cylinder pressure and temperature account for the shorter combustion period at increased compression pressure [99]. However, the shorter time required for combustion when using a methane-hydrogen blend as opposed to pure methane can be attributed to the faster flame speed of the blends [51]. Those findings are consistent with the literature to date. The combustion time was reduced by 21.5% when hydrogen was added to diesel-TEGMME blends at a concentration of 35%, as reported by Kumar et al. [30]. Burning times are decreased when H_2 concentrations rise. Increasing the hydrogen content to 60%, as stated by Cheng et al. . [51], shortens the combustion time by 30-50%.

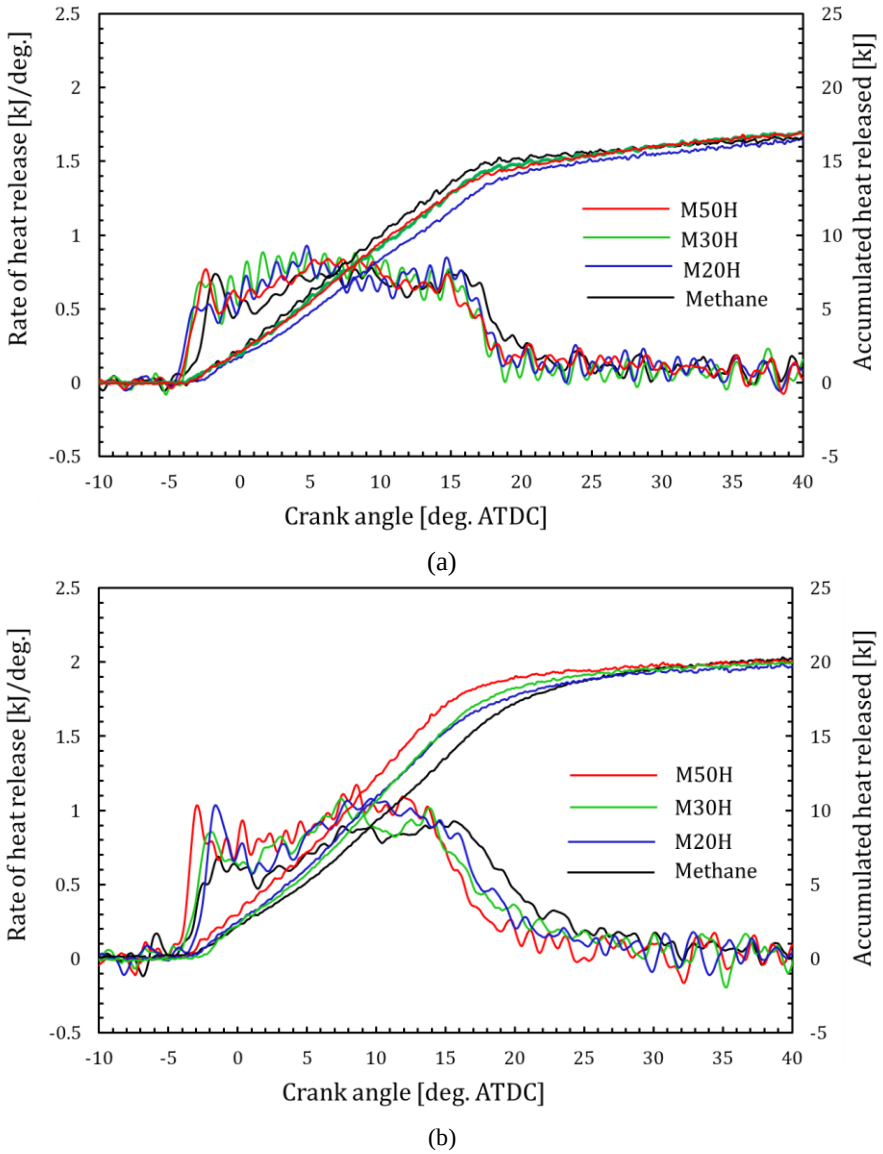

Figure 6.6 Heat release rate and accumulated heat released for methane and hydrogen mixture fuels versus crank angle under two injection cases a) 8 MPa and b) 15 MPa.

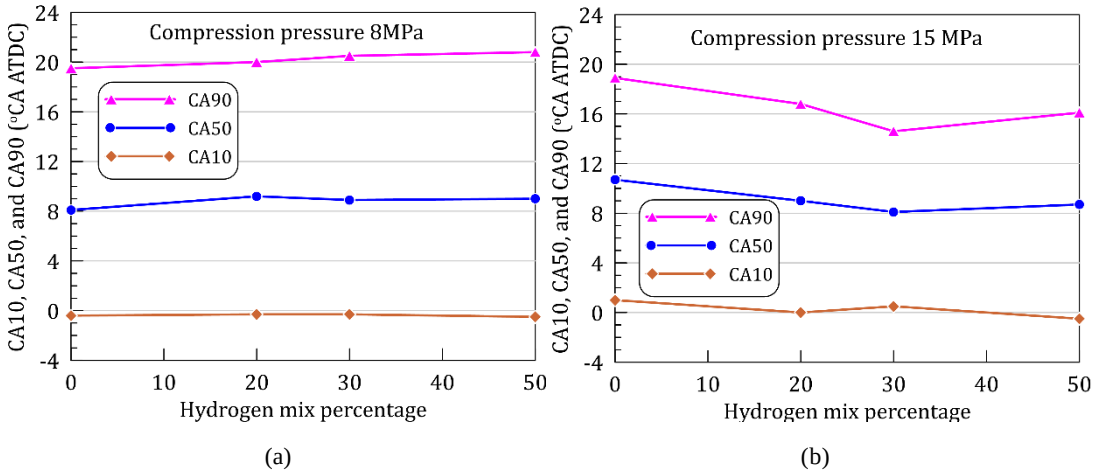

Figure 6.7 Combustion phases CA10, CA50, and CA90 for methane-hydrogen blends under two injection cases a) 8 MPa and b) 15 MPa.

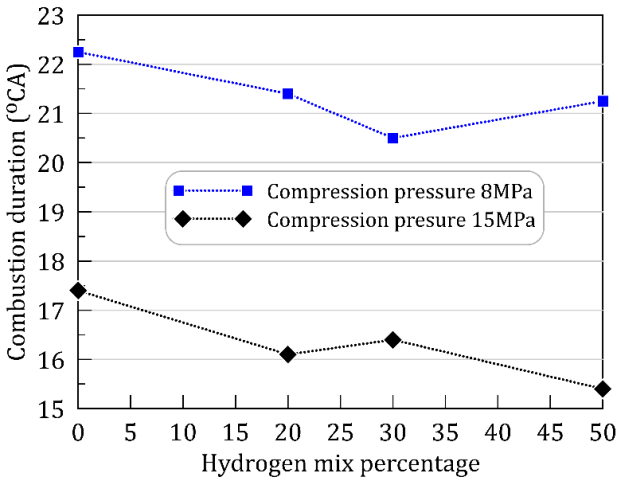

Figure 6.8 Combustion duration for methane-hydrogen blends under two different compression pressures

6.6.Emission characteristics

Different methane-gas blends have varying concentrations of CO, CO_2, NOx, and HC, which are discussed in this section. Exhaust gas emission concentrations for two different hydrogen-methane mixes and compression pressures are shown in Figure 6.9. Although NG has one of the lowest carbon concentrations among hydrocarbons, it has a lower tendency to CO_2 emissions than diesel fuel [105]. NG still emits CO_2, the main contributor to global warming, as a byproduct of combustion. In this work results, CO_2 concentration in the exhaust gases records a linear reduction with the methane substitution with hydrogen. This reduction is the direct benefit of using hydrogen to decrease the GHG impact of combusting methane. Hydrogen usage decreased CO_2 by 2 %, 3.5%, and 17.4% at 8 MPa and by 8.9%, 13.6%, and 23.7% at 15 MPa for M20H, M30H, and M50H,

respectively. Karimi et al. [106] reported the linear decrease in CO_2 emissions with increasing hydrogen percentage.

Natural gas (NG) has a low tendency to CO2 emissions than diesel fuel [105], while having one of the lowest carbon contents among hydrocarbons. When burned, NG still releases significant amounts of carbon dioxide, the principal greenhouse gas. According to the findings of this study, replacing methane with hydrogen leads to a linear decrease in the concentration of carbon dioxide in the exhaust gases. Hydrogen is used to mitigate the greenhouse gas emissions caused by the combustion of methane, and this is the direct advantage. Hydrogen usage decreased CO_2 by 2 %, 3.5%, and 17.4% at 8 MPa and by 8.9%, 13.6%, and 23.7% at 15 MPa for M20H, M30H, and M50H, respectively. Carbon dioxide emissions were shown to decrease linearly with increasing hydrogen content, as reported by Karimi et al. [106].

Carbon monoxide (CO) formation depends on both combustion temperature and the quantity of unburned gaseous fuel [103]. Because methane gas is so difficult to ignite, it contributes significantly to global warming [53]. Methane's limited flammability may help to explain why premixed combustion results in such significant quantities of CO emissions. When using methane as a premixed fuel, Benbellil et al. [103] found that absolute CO concentrations were 1000-1400 ppm (depending on the load), but they were only 50-100 ppm when using diesel. When 50% hydrogen was applied, these extremely high CO emission levels dropped by 55%. However, Ishibashi et al. [107] found that direct methane injection resulted in CO emissions as low as 8-10 ppm. In addition, between 60 and 240 ppm are produced with direct injection of NG, as described in the review work by Li et al. [108]. Figure 6.9 displays that almost the same CO emission was generated with the direct injection (diffusive combustion) of the methane-hydrogen mixes used in this research. In addition, the direct injection was the primary reason to improve methane combustion and reduce generated CO emissions, whereas the hydrogen impact had essentially little influence on either variable.

Hydrogen, on the other hand, can aid in the combustion of cylinder particulate matter, which could result in a more efficient engine cylinder [109]. Meanwhile, even with that improvement, it was still impossible to guarantee that the combustion would be completed. Consequently, HC emissions [110] consist of organic chemicals produced during combustion. The concentration of HC in the exhaust gases is shown in Figure 6.9 for various mixtures of methane gas utilized in the RCEM. The HC pattern is consistent

in both compression scenarios, but with a varied degree of tightening. At 8 MPa compression ratio, HC was reduced by 60% compared to methane, while at 15 MPa compression pressure, HC was reduced by 40% compared to pure methane. The rapid consumption of hydrogen causes its full combustion, which in turn reduces HC concentrations [109]. The increased combustibility of hydrogen gas also boosts the production of the essential radicals OH, O, and OH.

Concentrations of NOx emissions from the tested fuels are shown in the figure. The NOx emissions for M20H, M30H, and M50H all rose by 4.7%, 14.5%, and 48.6%, respectively, at 8 MPa compression pressure. At 15 MPa compression pressure, the NOx emissions for M20H were 16.3 percent higher than for M30H and 50 percent more than for M50H. When using up to three times as much hydrogen as diesel, the NOx emission was observed to be high by Liu et al. When the pilot spray ignites, a hotspot forms along the flame's leading edge due to the rapid elaboration of heat. The substantial rise in premixed combustion [53] is a result of the quicker burning of hydrogen-methane mixes. Enhanced premixed combustion results in high local temperatures and thus, NOx emissions. The increased combustion temperature accounted for the majority of the increase in NOx emissions that Benbellil et al. [103] found.

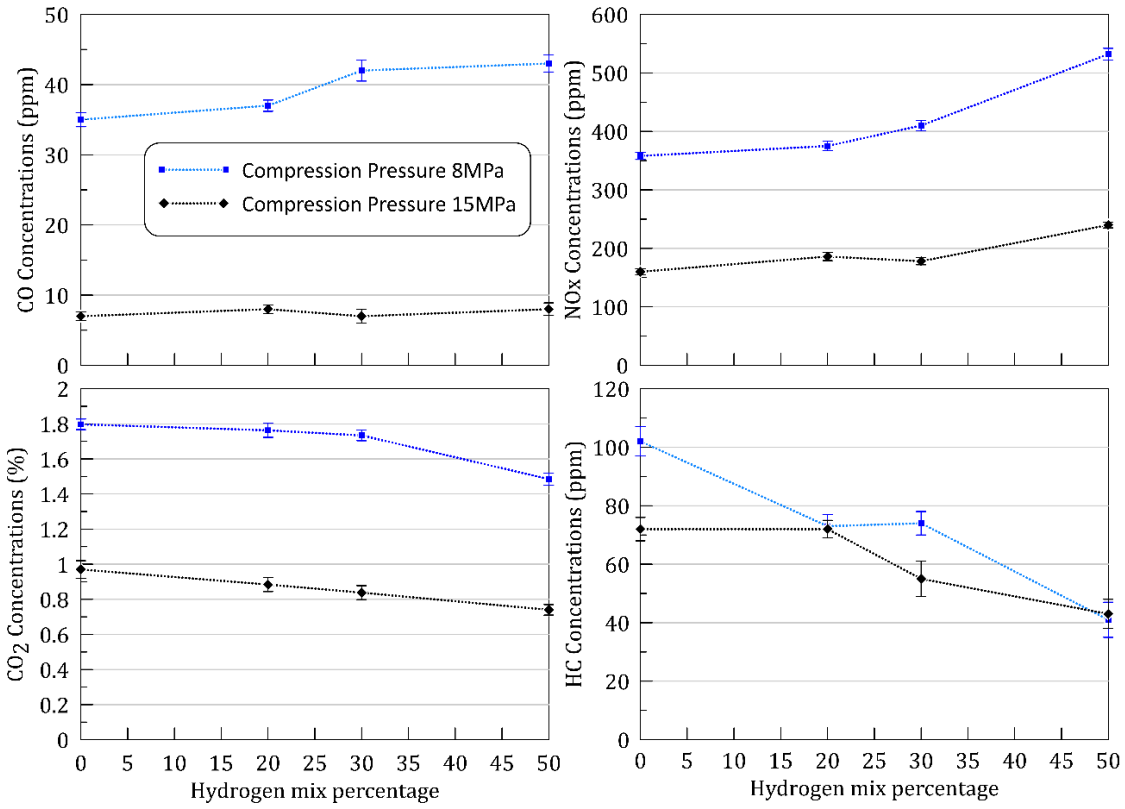

Figure 6.9 Emission characteristics (carbon dioxide, carbon monoxide, Hydrocarbons, and NOx) in the exhaust gases when fueling the engine with hydrogen-methane blends.

6.7.Indicated mean effective pressure

The Indicated Mean Effective Pressure (IMEP) could be estimated for all test fuels since the cumulative heat emitted was held constant throughout the investigation. The IMEP for various mixtures of methane and hydrogen at two different compression pressures is depicted in Figure 6.10. All mixtures of methane and hydrogen provide an IMEP that is greater than the methane baseline. The significance of the hydrogen substitution % is shown by the tendencies of the reported efficiency. High peak HRR and short combustion duration are characteristics of the cases with an extensive replacement percentage, i.e. 50%. Additionally, hydrogen replacement could have reduced heat loss via the walls [53]. The hydrogen-methane blends attained (0.19, 0.2, and 0.2) MPa for M20H, M30H, and M50H, respectively, at 8 MPa compression pressure, but the methane case barely hit 0.18 MPa. At 8 MPa compression pressure, the methane-hydrogen blends improved IMEP by (5.6), (11.1), and (11.1%) compared to methane, whereas at 15 MPa compression pressure, the respective percentages were (2.8), (5.6), and (11.1%), respectively. Those findings are consistent with previous research by Liu et al. [55].

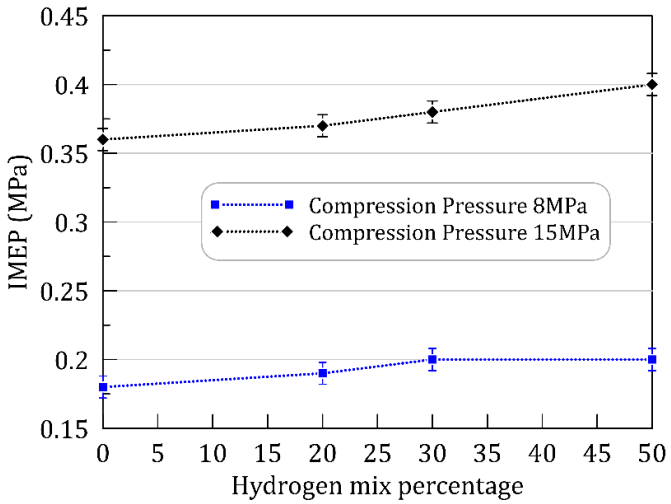

Figure 6.10 IMEP for different hydrogen-methane blends at two compression pressure cases 8 and 15 MPa.

Chapter 7

Conclusions & Recommendations

7.1. Conclusions

In this thesis, we investigated several approaches for enhancing the efficiency of marine diesel engines and decreasing the produced emissions. Both experimental and computational research were conducted to better understand the dynamics of diesel spray and methane jet behaviors under engine-like circumstances. Using these foundations as a jumping off point, we investigated three targeted strategies: the usage of combined exhaust gas recirculation (EGR) and water emulsion, the utilization of methane-inert gases, and the application of methane-hydrogen as a direct-injected fuel.

Our research provided significant understanding of the relationship between fuel injection characteristics and air entrainment. In particular, we found that active entrainment resulting from spray development and droplet dispersion was significantly larger than the passive entrainment of air generated by spray motion. Additionally, as injection pressure was elevated, a larger amount of air was entrained into the spray.

Nitrogen oxide (NOx) emissions were reduced by 94% thanks to the combination of water emulsion and EGR, and thermal efficiency was increased by 4%. The addition of water to the combustion process lowered NOx generation because the latent heat of evaporating water lowered the combustion temperature.

In addition, we investigated the feasibility of employing carbon dioxide-methane dilutions and methane-nitrogen mixes as substitute fuels. Methane-nitrogen combinations and carbon dioxide-methane dilutions both showed satisfactory result, lowering NOx emissions by 62% and 54%, respectively, compared to emissions from conventional gas oil fuel.

The results of using hydrogen and methane as a direct-injected fuel blend were also significant. Carbon dioxide (CO_2) and hydrocarbon emissions were cut by 23% and 60%, respectively, using this blending method, while in-cylinder pressure and indicated mean effective pressure were improved by 7.5% and 11%, respectively.

Our findings lead us to suggest a number of measures that might improve the efficiency of marine propulsion engines while cutting down on pollution. To increase the effectiveness of methane jets, we recommend diluting them with 17.5 % carbon dioxide gas. In addition, increasing in-cylinder pressure and overall engine performance can be achieved by using a methane-hydrogen blend consisting of 30% hydrogen and 70% methane.

7.2.Recommendations

This study recommends diluting the methane gas with 17.5% carbon dioxide gas to enhance the methane jet penetration. Also, utilizing a methane-hydrogen with 30% hydrogen and 70% methane to enhancement the in-cylinder pressure and. Blending methane with other gases could be applied in an engine constructed with high-pressured injection system, and the best representative of this engine is the dual-fuel engine model MAN B&W ME-GI and its upgraded version MAN B&W ME-GI Mk. 2.

7.3.Future work

- It is recommended that research be conducted into the possibility of combining methane with other fuels in order to increase its combustibility and decrease the wet-wall phenomena.
- NOx reduction technology such as EGR might be employed with a high percentage of hydrogen in order to reduce the increased levels of NOx emissions that are produced when hydrogen levels are high.

Bibliography

[1] Z. Shi, C. fon Lee, H. Wu, H. Li, Y. Wu, L. Zhang, Y. Bo, F. Liu, Effect of injection pressure on the impinging spray and ignition characteristics of the heavy-duty diesel engine under low-temperature conditions, Appl. Energy. 262 (2020) 114552. https://doi.org/10.1016/j.apenergy.2020.114552.

[2] L. De Simio, S. Iannaccone, Gaseous and particle emissions in low-temperature combustion diesel–HCNG dual-fuel operation with double pilot injection, Appl. Energy. 253 (2019) 113602. https://doi.org/10.1016/j.apenergy.2019.113602.

[3] M.C. Cameretti, R. De Robbio, E. Mancaruso, M. Palomba, CFD Study of Dual Fuel Combustion in a Research Diesel Engine Fueled by Hydrogen, Energies. 15 (2022). https://doi.org/10.3390/en15155521.

[4] P. Talebizadeh, M. Babaie, R. Brown, H. Rahimzadeh, Z. Ristovski, M. Arai, The role of non-thermal plasma technique in NOx treatment: A review, Renew. Sustain. Energy Rev. 40 (2014) 886–901. https://doi.org/10.1016/j.rser.2014.07.194.

[5] N. Førby, T.B. Thomsen, R.F. Cordtz, F. Bræstrup, J. Schramm, Ignition and combustion study of premixed ammonia using GDI pilot injection in CI engine, Fuel. 331 (2023) 125768. https://doi.org/10.1016/j.fuel.2022.125768.

[6] Y. Wang, X. Zhou, L. Liu, Theoretical investigation of the combustion performance of ammonia/hydrogen mixtures on a marine diesel engine, Int. J. Hydrogen Energy. 46 (2021) 14805–14812. https://doi.org/10.1016/J.IJHYDENE.2021.01.233.

[7] A.K. Hossain, P. Refahtalab, A. Omran, D.I. Smith, P.A. Davies, An experimental study on performance and emission characteristics of an IDI diesel engine operating with neat oil-diesel blend emulsion, Renew. Energy. 146 (2020) 1041–1050. https://doi.org/10.1016/j.renene.2019.06.162.

[8] M. Puškár, M. Kopas, D. Puškár, J. Lumnitzer, E. Faltinová, Method for reduction of the NOX emissions in marine auxiliary diesel engine using the fuel mixtures containing biodiesel using HCCI combustion, Mar. Pollut. Bull. 127 (2018) 752–760. https://doi.org/10.1016/j.marpolbul.2017.08.031.

[9] C.W. Mohd Noor, M.M. Noor, R. Mamat, Biodiesel as alternative fuel for marine diesel engine applications: A review, Renew. Sustain. Energy Rev. 94 (2018) 127–142. https://doi.org/10.1016/j.rser.2018.05.031.

[10] Emission Standards, d. Internal: IMO marine engine regulations, (n.d.). https://www.imo.org/en/OurWork/Environment/Pages/GHG-Emissions.aspx#:~:text=The Fourth IMO GHG Study,tonnes of CO2 in.

[11] A.A. Arpia, W.H. Chen, S.S. Lam, P. Rousset, M.D.G. de Luna, Sustainable biofuel and bioenergy production from biomass waste residues using microwave-assisted heating: A comprehensive review, Chem. Eng. J. 403 (2021) 126233. https://doi.org/10.1016/j.cej.2020.126233.

[12] J. Deng, X. Wang, Z. Wei, L. Wang, C. Wang, Z. Chen, A review of NOx and SOx emission reduction technologies for marine diesel engines and the potential evaluation of liquefied natural gas fuelled vessels, Sci. Total Environ. 766 (2021) 144319. https://doi.org/10.1016/j.scitotenv.2020.144319.

[13] H.J. Kim, S.H. Park, C.S. Lee, Impact of fuel spray angles and injection timing on the combustion and emission characteristics of a high-speed diesel engine, Energy.

107 (2016) 572–579. https://doi.org/10.1016/j.energy.2016.04.035.
[14] E. Jiaqiang, Z. Zhang, J. Chen, M.H. Pham, X. Zhao, Q. Peng, B. Zhang, Z. Yin, Performance and emission evaluation of a marine diesel engine fueled by water biodiesel-diesel emulsion blends with a fuel additive of a cerium oxide nanoparticle, Energy Convers. Manag. 169 (2018) 194–205. https://doi.org/10.1016/J.ENCONMAN.2018.05.073.
[15] W. Yoon, J.Y. Kim, D.H. Kim, K.D. Kim, Optimization of Fuel Injection Nozzles for Reduction of NOx Emissions in Medium-speed Marinethe Diesel Engines, Sixth Lnternational Symp. Diagnostics Model. Combust. Lnternal Combust. Engine. (2004) 81–86. https://doi.org/https://doi.org/10.1299/jmsesdm.2004.6.81.
[16] D. Hariharan, S. Rajan Krishnan, K. Kumar Srinivasan, A. Sohail, Multiple injection strategies for reducing HC and CO emissions in diesel-methane dual-fuel low temperature combustion, Fuel. 305 (2021) 121372. https://doi.org/10.1016/j.fuel.2021.121372.
[17] M.C. Cameretti, R. De Robbio, Raffaele Tuccillo, Performance Improvement and Emission Control of a Dual Fuel Operated Diesel Engine, in: 13th Int. Conf. Engines Veh., 2017: pp. 24–66. https://doi.org/10.4271/2017-24-0066.
[18] F. D'Aniello, I. Arsie, C. Pianese, F. Stola, Development of an integrated control strategy for engine and SCR system based on effective EGR rate, IFAC-PapersOnLine. 53 (2020) 14034–14039. https://doi.org/10.1016/j.ifacol.2020.12.925.
[19] T. Kuwahara, K. Yoshida, T. Kuroki, K. Hanamoto, K. Sato, M. Okubo, Pilot-scale aftertreatment using nonthermal plasma reduction of adsorbed NOx in marine diesel-engine exhaust gas, Plasma Chem. Plasma Process. 34 (2014) 65–81. https://doi.org/10.1007/s11090-013-9486-0.
[20] S. Yang, X. Pan, Z. Han, D. Zhao, B. Liu, D. Zheng, Z. Yan, Removal of NOx and SO2 from simulated ship emissions using wet scrubbing based on seawater electrolysis technology, Chem. Eng. J. 331 (2018) 8–15. https://doi.org/10.1016/j.cej.2017.08.083.
[21] J. Zhou, J. Ma, Z. Wang, Experimental study on removal performance of SO2 and NOx in marine exhaust gas using seawater/urea peroxide solution and analysis of ions concentration change, Fuel Process. Technol. 227 (2022) 107133. https://doi.org/10.1016/j.fuproc.2021.107133.
[22] P. Wang, X. Tang, L. Shi, X. Ni, Z. Hu, K. Deng, Experimental investigation of the influences of Miller cycle combined with EGR on performance, energy and exergy characteristics of a four-stroke marine regulated two-stage turbocharged diesel engine, Fuel. 300 (2021) 120940. https://doi.org/10.1016/J.FUEL.2021.120940.
[23] W. Zhang, T. Feng, Z. Li, Z. Chen, J. Zhao, EGR thermal and chemical effects on combustion and emission of diesel/natural gas dual-fuel engine, Fuel. 302 (2021) 121161. https://doi.org/10.1016/J.FUEL.2021.121161.
[24] P. Ni, X. Wang, H. Li, A review on regulations, current status, effects and reduction strategies of emissions for marine diesel engines, Fuel. 279 (2020) 118477. https://doi.org/10.1016/J.FUEL.2020.118477.
[25] X. Yuan, X. Ding, L. Leng, H. Li, J. Shao, Y. Qian, H. Huang, X. Chen, G. Zeng, Applications of bio-oil-based emulsions in a DI diesel engine: The effects of bio-oil compositions on engine performance and emissions, Energy. 154 (2018) 110–118. https://doi.org/10.1016/j.energy.2018.04.118.
[26] R.K. Gopidesi, S.R. Premkartikkumar, Evaluating the hythane/water diesel emulsion dual fuel diesel engine characteristics at various pilot diesel injection

timings, Mater. Today Proc. (2021). https://doi.org/10.1016/j.matpr.2021.07.127.
[27] M. Aghbashlo, M. Tabatabaei, E. Khalife, B. Najafi, Z. Khounani, A novel emulsion fuel containing aqueous nano cerium oxide additive in diesel – biodiesel blends to improve diesel engines performance and reduce exhaust emissions : Part II – Exergetic analysis, Fuel. 205 (2017) 262–271. https://doi.org/10.1016/j.fuel.2017.05.003.
[28] P. Murugesan, A.T. Hoang, E. Perumal Venkatesan, D. Santosh Kumar, D. Balasubramanian, A.T. Le, V.V. Pham, Role of hydrogen in improving performance and emission characteristics of homogeneous charge compression ignition engine fueled with graphite oxide nanoparticle-added microalgae biodiesel/diesel blends, Int. J. Hydrogen Energy. (2021). https://doi.org/10.1016/j.ijhydene.2021.08.107.
[29] N. Ganesan, T.H. Le, P. Ekambaram, D. Balasubramanian, V.V. Le, A.T. Hoang, Experimental assessment on performance and combustion behaviors of reactivity-controlled compression ignition engine operated by n-pentanol and cottonseed biodiesel, J. Clean. Prod. 330 (2022) 129781. https://doi.org/10.1016/j.jclepro.2021.129781.
[30] A. Kumar, C. Bhushan Kumar, D.B. Lata, Effect of addition of fuel additive in diesel with hydrogen on combustion duration, Mater. Today Proc. (2022). https://doi.org/10.1016/j.matpr.2022.08.305.
[31] N.K. Vinayagam, A.T. Hoang, J.M. Solomon, M. Subramaniam, D. Balasubramanian, A.I. EL-Seesy, X.P. Nguyen, Smart control strategy for effective hydrocarbon and carbon monoxide emission reduction on a conventional diesel engine using the pooled impact of pre-and post-combustion techniques, J. Clean. Prod. 306 (2021) 127310. https://doi.org/10.1016/j.jclepro.2021.127310.
[32] D. Imhof, D. Tsuru, H. Tajima, K. Takasaki, High-pressure natural gas injection (GI) marine engine research with a Rapid Compression Expansion Machine, in: CIMAC Congr. 2013, Shanghai, 2013: p. 11.
[33] S.K. Nayak, A.T. Hoang, S. Nižetić, X.P. Nguyen, T.H. Le, Effects of advanced injection timing and inducted gaseous fuel on performance, combustion and emission characteristics of a diesel engine operated in dual-fuel mode, Fuel. 310 (2022) 1–16. https://doi.org/10.1016/j.fuel.2021.122232.
[34] M. Taghi Zarrinkolah, V. Hosseini, Methane slip reduction of conventional dual-fuel natural gas diesel engine using direct fuel injection management and alternative combustion modes, Fuel. 331 (2023) 125775. https://doi.org/10.1016/j.fuel.2022.125775.
[35] F. Jaliliantabar, B. Ghobadian, A.P. Carlucci, G. Najafi, R. Mamat, A. Ficarella, L. Strafella, A. Santino, S. De Domenico, A comprehensive study on the effect of pilot injection, EGR rate, IMEP and biodiesel characteristics on a CRDI diesel engine, Energy. 194 (2020). https://doi.org/10.1016/j.energy.2019.116860.
[36] X. Sun, J. Ning, X. Liang, G. Jing, Y. Chen, G. Chen, Effect of direct water injection on combustion and emissions characteristics of marine diesel engines, Fuel. 309 (2022) 122213. https://doi.org/10.1016/j.fuel.2021.122213.
[37] E. Abdelhameed, H. Tashima, Experimental investigation on methane inert gas dilution effect on marine gas diesel engine performance and emissions, Energy Sources, Part A Recover. Util. Environ. Eff. 44 (2022) 3584–3596. https://doi.org/10.1080/15567036.2022.2067603.
[38] Z. Wang, F. Zhang, Y. Xia, D. Wang, Y. Xu, G. Du, Combustion phase of a diesel/natural gas dual fuel engine under various pilot diesel injection timings, Fuel. 289 (2021) 119869. https://doi.org/10.1016/j.fuel.2020.119869.

[39] S. Lion, I. Vlaskos, R. Taccani, A review of emissions reduction technologies for low and medium speed marine Diesel engines and their potential for waste heat recovery, Energy Convers. Manag. 207 (2020) 112553. https://doi.org/10.1016/j.enconman.2020.112553.
[40] B. Petroleum, G. Expo, Fuel flexability in power generation onboard offshore floating units, in: Rio Oil Gas Expo Conf., 2012: pp. 1–7.
[41] H. Yu, W. Wang, D. Sheng, H. Li, S. Duan, Performance of combustion process on marine low speed two-stroke dual fuel engine at different fuel conditions: Full diesel/diesel ignited natural gas, Fuel. 310 (2022) 122370. https://doi.org/10.1016/j.fuel.2021.122370.
[42] C. fon Lee, Y. Pang, H. Wu, K. Nithyanandan, F. Liu, An optical investigation of substitution rates on natural gas/diesel dual-fuel combustion in a diesel engine, Appl. Energy. 261 (2020) 114455. https://doi.org/10.1016/j.apenergy.2019.114455.
[43] P. Ni, X. Wang, H. Li, A review on regulations, current status, effects and reduction strategies of emissions for marine diesel engines, Fuel. 279 (2020). https://doi.org/10.1016/j.fuel.2020.118477.
[44] MAN Diesel, ME-GI Dual Fuel MAN B & W Engines, 2013.
[45] United States Environmental Protection Agency, (2022). https://www.epa.gov/ghgemissions/sources-greenhouse-gas-emissions.
[46] S. Tüchler, P. Dimitriou, On the capabilities and limitations of predictive, multi-zone combustion models for hydrogen-diesel dual fuel operation, Int. J. Hydrogen Energy. 44 (2019) 18517–18531. https://doi.org/10.1016/j.ijhydene.2019.05.172.
[47] S.S. Lee, C. Kim, S.S. Lee, S. Oh, J. Kim, J. Lee, Characteristics of non-methane hydrocarbons and methane emissions in exhaust gases under natural-gas/diesel dual-fuel combustion, Fuel. 290 (2021) 120009. https://doi.org/10.1016/j.fuel.2020.120009.
[48] T. AOYAGI, E. Abdelhameed, D. Tsuru, H. Tashima, Experimental and Numerical Considerations of Air Entrainment Process of Diesel Spray, Int. Conf. Liq. At. Spray Syst. 1 (2021). https://doi.org/10.2218/iclass.2021.6105.
[49] R. Wang, H. Chen, C. Guan, W. Gong, Z. Zhang, Research on the fault monitoring method of marine diesel engines based on the manifold learning and isolation forest, Appl. Ocean Res. 112 (2021) 102681. https://doi.org/10.1016/J.APOR.2021.102681.
[50] V. Dhyani, K.A. Subramanian, Control of backfire and NOx emission reduction in a hydrogen fueled multi-cylinder spark ignition engine using cooled EGR and water injection strategies, Int. J. Hydrogen Energy. 44 (2019) 6287–6298. https://doi.org/10.1016/j.ijhydene.2019.01.129.
[51] Q. Cheng, Z. Ahmad, O. Kaario, V. Vuorinen, M. Larmi, Experimental study on tri-fuel combustion using premixed methane-hydrogen mixtures ignited by a diesel pilot, Int. J. Hydrogen Energy. 46 (2021) 21182–21197. https://doi.org/10.1016/j.ijhydene.2021.03.215.
[52] C.B. Kumar, D.B. Lata, D. Mahto, Effect of addition of di-tert butyl peroxide (DTBP) on performance and exhaust emissions of dual fuel diesel engine with hydrogen as a secondary fuel, Int. J. Hydrogen Energy. 46 (2021) 9595–9612. https://doi.org/10.1016/j.ijhydene.2020.12.129.
[53] J. Luo, Z. Liu, J. Wang, H. Xu, Y. Tie, D. Yang, Z. Zhang, C. Zhang, H. Wang, Investigation of hydrogen addition on the combustion, performance, and emission characteristics of a heavy-duty engine fueled with diesel/natural gas, Energy. 260 (2022) 125082. https://doi.org/10.1016/j.energy.2022.125082.

[54] X. Liu, G. Seberry, S. Kook, Q.N. Chan, E.R. Hawkes, Direct injection of hydrogen main fuel and diesel pilot fuel in a retrofitted single-cylinder compression ignition engine, Int. J. Hydrogen Energy. (2022). https://doi.org/10.1016/j.ijhydene.2022.08.149.
[55] X. Liu, A. Srna, H.L. Yip, S. Kook, Q.N. Chan, E.R. Hawkes, Performance and emissions of hydrogen-diesel dual direct injection (H2DDI) in a single-cylinder compression-ignition engine, Int. J. Hydrogen Energy. 46 (2020) 1302–1314. https://doi.org/10.1016/j.ijhydene.2020.10.006.
[56] M.T. Mito, M.A. Teamah, W.M. El-Maghlany, A.I. Shehata, Utilizing the scavenge air cooling in improving the performance of marine diesel engine waste heat recovery systems, Energy. 142 (2018) 264–276. https://doi.org/10.1016/j.energy.2017.10.039.
[57] M. HUO, AIR/FUEL MIXING ENHANCEMENT AND EMISSION REDUCTION THROUGH INTAKE PORT DESIGN AND VARIOUS FUEL EMULSIONS FOR DIESEL COMBUSTION, 2014. https://repositories.lib.utexas.edu/handle/2152/39127%0Ahttps://cris.brighton.ac.uk/ws/portalfiles/portal/4755978/Julius+Ojebode%27s+Thesis.pdf%0Ausir.salford.ac.uk/29369/1/Angela_Darvill_thesis_esubmission.pdf%0Ahttps://dspace.lboro.ac.uk/dspace-jspui/ha.
[58] Z. Wang, S. Zhou, Y. Feng, Y. Zhu, EGR modeling and fuzzy evaluation of Low-Speed Two-Stroke marine diesel engines, Sci. Total Environ. 706 (2020) 135444. https://doi.org/10.1016/j.scitotenv.2019.135444.
[59] H. Xi, S. Zhou, Z. Zhang, A novel method for the synchronous absorption of SO2 and NO from marine diesel engines, Fuel Process. Technol. 210 (2020) 106560. https://doi.org/10.1016/J.FUPROC.2020.106560.
[60] X. Liu, H. Wang, Z. Zheng, M. Yao, Numerical investigation on the combustion and emission characteristics of a heavy-duty natural gas-diesel dual-fuel engine, Fuel. 300 (2021) 120998. https://doi.org/10.1016/J.FUEL.2021.120998.
[61] J. Wang, X. Duan, W. Wang, J. Guan, Y. Li, J. Liu, Effects of the continuous variable valve lift system and Miller cycle strategy on the performance behavior of the lean-burn natural gas spark ignition engine, Fuel. 297 (2021) 120762. https://doi.org/10.1016/j.fuel.2021.120762.
[62] J. Wang, X. Duan, Y. Liu, W. Wang, J. Liu, M.C. Lai, Y. Li, G. Guo, Numerical investigation of water injection quantity and water injection timing on the thermodynamics, combustion and emissions in a hydrogen enriched lean-burn natural gas SI engine, Int. J. Hydrogen Energy. 45 (2020) 17935–17952. https://doi.org/10.1016/j.ijhydene.2020.04.146.
[63] X. Duan, Y. Liu, J. Liu, M.C. Lai, M. Jansons, G. Guo, S. Zhang, Q. Tang, Experimental and numerical investigation of the effects of low-pressure, high-pressure and internal EGR configurations on the performance, combustion and emission characteristics in a hydrogen-enriched heavy-duty lean-burn natural gas SI engine, Energy Convers. Manag. 195 (2019) 1319–1333. https://doi.org/10.1016/j.enconman.2019.05.059.
[64] W. Zhang, C. Song, G. Lv, F. Bi, Y. Qiao, L. Wang, X. Zhang, Properties and oxidation of in-cylinder soot associated with exhaust gas recirculation (EGR) in diesel engines, Proc. Combust. Inst. 38 (2021) 1319–1326. https://doi.org/10.1016/j.proci.2020.06.065.
[65] M.S. Gad, Z. He, A.S. El-Shafay, A.I. El-Seesy, Combustion characteristics of a diesel engine running with Mandarin essential oil -diesel mixtures and propanol additive under different exhaust gas recirculation: Experimental investigation and

numerical simulation, Case Stud. Therm. Eng. 26 (2021). https://doi.org/10.1016/j.csite.2021.101100.
[66] M. Mukhtar, F.Y. Hagos, A.R.A. Aziz, A.A. Abdulah, Z.A.A. Karim, Combustion characteristics of tri-fuel (diesel-ethanol-biodiesel) emulsion fuels in CI engine with micro-explosion phenomenon attributes, Fuel. 312 (2022) 122933. https://doi.org/10.1016/j.fuel.2021.122933.
[67] J. Park, J. Oh, Study on the characteristics of performance, combustion, and emissions for a diesel water emulsion fuel on a combustion visualization engine and a commercial diesel engine, Fuel. 311 (2022) 122520. https://doi.org/10.1016/j.fuel.2021.122520.
[68] M. Abdollahi, B. Ghobadian, G. Najafi, S.S. Hoseini, M. Mofijur, M. Mazlan, Impact of water – biodiesel – diesel nano-emulsion fuel on performance parameters and diesel engine emission, Fuel. 280 (2020). https://doi.org/10.1016/j.fuel.2020.118576.
[69] Y. Wakuri, M. Fujii, T. Amitani, R. Tsuneya, Studies on the penetration of fuel spray in a diesel engine, Bull JSME. 3 (1960) 123–30.
[70] H. Hiroyasu, M. Arai, Structures of fuel sprays in diesel engines, SAE Tech. Pap. (1990) 900475.
[71] J. Xia, Z. Huang, L. Zhang, Q. Zhang, L. Zheng, R. Liu, D. Ju, X. Lu, Experimental comparisons on injection and atomization characteristics of diesel and its six-component surrogate under different critical conditions of marine engine, Energy Convers. Manag. 205 (2020) 112397. https://doi.org/10.1016/j.enconman.2019.112397.
[72] K. Kannaiyan, R. Sadr, The effects of alumina nanoparticles as fuel additives on the spray characteristics of gas-to-liquid jet fuels, Exp. Therm. Fluid Sci. 87 (2017) 93–103. https://doi.org/10.1016/j.expthermflusci.2017.04.027.
[73] Y. Yu, W. Lin, L. Li, Z. Zhang, Effects of hydrogen addition on the combustion characteristics of diesel fuel jets under ultra-high injection pressures, Int. J. Hydrogen Energy. 45 (2020) 10592–10601. https://doi.org/10.1016/j.ijhydene.2019.08.242.
[74] M.N.A. Mukhtar, F.Y. Hagos, M.M. Noor, R. Mamat, A.A. Abdullah, A.R. Abd Aziz, Tri-fuel emulsion with secondary atomization attributes for greener diesel engine – A critical review, Renew. Sustain. Energy Rev. 111 (2019) 490–506. https://doi.org/10.1016/j.rser.2019.05.035.
[75] M. Choi, K. Mohiuddin, N. Kim, S. Park, Investigation of the effects of EGR rate, injection strategy and nozzle specification on engine performances and emissions of a single cylinder heavy duty diesel engine using the two color method, Appl. Therm. Eng. 193 (2021) 117036. https://doi.org/10.1016/j.applthermaleng.2021.117036.
[76] J. Jeon, S. Park, Effect of injection pressure on soot formation/oxidation characteristics using a two-color photometric method in a compression-ignition engine fueled with biodiesel blend (B20), Appl. Therm. Eng. 131 (2018) 284–294. https://doi.org/10.1016/j.applthermaleng.2017.12.005.
[77] A. Kakoee, A. Gharehghani, Comparative study of hydrogen addition effects on the natural-gas/diesel and natural-gas/dimethyl-ether reactivity controlled compression ignition mode of operation, Energy Convers. Manag. 196 (2019) 92–104. https://doi.org/10.1016/j.enconman.2019.05.113.
[78] Y. Lu, J. Pan, B. Fan, P. Otchere, W. Chen, B. Cheng, Research on the application of aviation kerosene in a direct injection rotary engine-Part 1: Fundamental spray characteristics and optimized injection strategies, Energy Convers. Manag. 195

(2019) 519–532. https://doi.org/10.1016/j.enconman.2019.05.042.
[79] A. Matsumoto, D. Tsuru, H. Tashima, Reduction of NOx Emission from Diesel Engines by Exhaust Gas Recirculation and Fuel-Water Emulsification, kyushu University, 2013.
[80] R.A. Glassman, I., & Yetter, Diffusion Flames., 2008. https://doi.org/10.1016/B978-0-12-088573-2.00006-3.
[81] X. Li, X. Zhen, Y. Wang, D. Liu, Z. Tian, The knock study of high compression ratio SI engine fueled with methanol in combination with different EGR rates, Fuel. 257 (2019) 116098. https://doi.org/10.1016/j.fuel.2019.116098.
[82] S. Verma, L.M. Das, S.C. Kaushik, S.S. Bhatti, The effects of compression ratio and EGR on the performance and emission characteristics of diesel-biogas dual fuel engine, Appl. Therm. Eng. 150 (2019) 1090–1103. https://doi.org/10.1016/j.applthermaleng.2019.01.080.
[83] J. Zhao, R. Fu, S. Wang, H. Xu, Z. Yuan, Fuel economy improvement of a turbocharged gasoline SI engine through combining cooled EGR and high compression ratio, Energy. 239 (2022) 122353. https://doi.org/10.1016/j.energy.2021.122353.
[84] M. Pan, W. Qian, Z. Zheng, R. Huang, X. Zhou, H. Huang, M. Li, The potential of dimethyl carbonate (DMC) as an alternative fuel for compression ignition engines with different EGR rates, Fuel. 257 (2019) 115920. https://doi.org/10.1016/j.fuel.2019.115920.
[85] Z. Ahmad, O. Kaario, S. Karimkashi, C. Qiang, V. Vuorinen, M. Larmi, Effects of ethane addition on diesel-methane dual-fuel combustion in a heavy-duty engine, Fuel. 289 (2021) 119834. https://doi.org/10.1016/j.fuel.2020.119834.
[86] M. Mikulski, S. Wierzbicki, Numerical investigation of the impact of gas composition on the combustion process in a dual-fuel compression-ignition engine, J. Nat. Gas Sci. Eng. 31 (2016) 525–537. https://doi.org/10.1016/j.jngse.2016.03.074.
[87] A. Jamrozik, K. Grab-Rogaliński, W. Tutak, Hydrogen effects on combustion stability, performance and emission of diesel engine, Int. J. Hydrogen Energy. 45 (2020) 19936–19947. https://doi.org/10.1016/j.ijhydene.2020.05.049.
[88] A. Yousefi, H. Guo, S. Dev, B. Liko, S. Lafrance, Effect of pre-main-post diesel injection strategy on greenhouse gas and nitrogen oxide emissions of natural gas/diesel dual-fuel engine at high load conditions, Fuel. 302 (2021) 121110. https://doi.org/10.1016/J.FUEL.2021.121110.
[89] J. Stewart, A. Clarke, R. Chen, An experimental study of the dual-fuel performance of a small compression ignition diesel engine operating with three gaseous fuels, Proc. Inst. Mech. Eng. Part D J. Automob. Eng. 221 (2007) 943–956. https://doi.org/10.1243/09544070JAUTO458.
[90] Y. He, M. Liang, C. Liu, S. Liao, R. Yang, L. Qin, X. Jian, Y. Shao, Kinetic incentive of hydrogen addition on nonpremixed laminar methane/air flames, Int. J. Hydrogen Energy. (2021) 1–11. https://doi.org/10.1016/j.ijhydene.2021.01.230.
[91] A.H. Kakaee, A. Paykani, M. Ghajar, The influence of fuel composition on the combustion and emission characteristics of natural gas fueled engines, Renew. Sustain. Energy Rev. 38 (2014) 64–78. https://doi.org/10.1016/j.rser.2014.05.080.
[92] M.R.A. Mansor, M.M. Abbood, T.I. Mohamad, The influence of varying hydrogen-methane-diesel mixture ratio on the combustion characteristics and emissions of a direct injection diesel engine, Fuel. 190 (2017) 281–291. https://doi.org/10.1016/j.fuel.2016.11.010.
[93] E.J.C. Cavalcanti, Energy, exergy and exergoenvironmental analyses on gas-diesel

fuel marine engine used for trigeneration system, Appl. Therm. Eng. 184 (2021) 116211. https://doi.org/10.1016/J.APPLTHERMALENG.2020.116211.
[94] X. Wang, B. gang Sun, Q. he Luo, L. zhi Bao, J. ye Su, J. Liu, X. chao Li, Visualization research on hydrogen jet characteristics of an outward-opening injector for direct injection hydrogen engines, Fuel. 280 (2020) 118710. https://doi.org/10.1016/j.fuel.2020.118710.
[95] W.Y. Sakellarakis V, Vera-Tudela W, Doll U, Ebi D, Boulouchos K. The effect of high-pressure injection variations on the mixing state of underexpanded methane jets, Int. J. Engine Res. 22 (2020). https://doi.org/https://doi.org/10.1177/1468087420960895.
[96] E. Abdelhameed, T. Aoyagi, H. Tashima, D. Tsuru, PIV measurements of entrainment process of directly injected media in internal combustion engines, 14th Int. Symp. Part. Image Velocim. 1 (2021) 1–10. https://doi.org/10.18409/ispiv.v1i1.184.
[97] M. Yeganeh, Q. Cheng, A. Dharamsi, S. Karimkashi, J. Kuusela-Opas, O. Kaario, M. Larmi, Visualization and comparison of methane and hydrogen jet dynamics using schlieren imaging, Fuel. 331 (2023) 125762. https://doi.org/10.1016/j.fuel.2022.125762.
[98] and J.D.M. Petrucci, Ralph H., F. Geoffrey Herring, General chemistry: principles and modern applications, Pearson Prentice Hal, 2010.
[99] P. Rosha, S. Kumar, P. Senthil Kumar, C.N. Kowthaman, S. Kumar Mohapatra, A. Dhir, Impact of compression ratio on combustion behavior of hydrogen enriched biogas-diesel operated CI engine, Fuel. 310 (2022) 122321. https://doi.org/10.1016/j.fuel.2021.122321.
[100] J. Larfeldt, Technology options and plant design issues for fuel-flexible gas turbines., in: Fuel Flex. Energy Gener., 2016: pp. 271–291. https://doi.org/10.1016/B978-1-78242-378-2.00010-9.
[101] J. Cheng, B. Zhang, T. Dai, H. Liu, Effects of jet/flame interaction on deflagration-to-detonation transition by non-reactive gas jet in a methane-oxygen mixture, Aerosp. Sci. Technol. 126 (2022) 107581. https://doi.org/10.1016/j.ast.2022.107581.
[102] M.E.M. Soudagar, M.A. Mujtaba, M.R. Safaei, A. Afzal, D.R. V, W. Ahmed, N.R. Banapurmath, N. Hossain, S. Bashir, I.A. Badruddin, M. Goodarzi, K. Shahapurkar, S.N. Taqui, Effect of Sr@ZnO nanoparticles and Ricinus communis biodiesel-diesel fuel blends on modified CRDI diesel engine characteristics, Energy. 215 (2021) 119094. https://doi.org/10.1016/j.energy.2020.119094.
[103] M.A. Benbellil, M.S. Lounici, K. Loubar, M. Tazerout, Investigation of natural gas enrichment with high hydrogen participation in dual fuel diesel engine, Energy. 243 (2022) 122746. https://doi.org/10.1016/j.energy.2021.122746.
[104] J.B. Heywood, Internal Combustion Engine Fundamentals. N. York: McGraw-Hill, 1988.
[105] J. Deng, X. Wang, Z. Wei, L. Wang, C. Wang, Z. Chen, A review of NOx and SOx emission reduction technologies for marine diesel engines and the potential evaluation of liquefied natural gas fuelled vessels, Sci. Total Environ. 766 (2021) 144319. https://doi.org/10.1016/J.SCITOTENV.2020.144319.
[106] M. Karimi, X. Wang, J. Hamilton, M. Negnevitsky, Numerical investigation on hydrogen-diesel dual-fuel engine improvements by oxygen enrichment, Int. J. Hydrogen Energy. 47 (2022) 25418–25432. https://doi.org/10.1016/j.ijhydene.2022.05.271.
[107] R. Ishibashi, D. Tsuru, An optical investigation of combustion process of a direct

high-pressure injection of natural gas, J. Mar. Sci. Technol. 22 (2017) 447–458. https://doi.org/10.1007/s00773-016-0422-x.
[108] M. Li, H. Wu, T. Zhang, B. Shen, Q. Zhang, Z. Li, A comprehensive review of pilot ignited high pressure direct injection natural gas engines: Factors affecting combustion, emissions and performance, Renew. Sustain. Energy Rev. 119 (2020) 109653. https://doi.org/10.1016/j.rser.2019.109653.
[109] P. Raju, S.K. Masimalai, N. Ganesan, S. V. Karthic, Engine's behavior on hydrogen addition of waste cooking oil fueled light duty diesel engine - A dual fuel approach, Energy. 194 (2020) 116844. https://doi.org/10.1016/j.energy.2019.116844.
[110] R. Sathiyamoorthi, G. Sankaranarayanan, S.B. Adhith kumaar, T. Chiranjeevi, D. Dilip Kumar, Experimental investigation on performance, combustion and emission characteristics of a single cylinder diesel engine fuelled by biodiesel derived from Cymbopogon Martinii, Renew. Energy. 132 (2019) 394–415. https://doi.org/10.1016/j.renene.2018.08.001.